NORTHWESTERN UNIVERSITY

Thermal Transport Near The Normal-Metal/Superconductor Interface In Mesoscopic Devices

A DISSERTATION

SUBMITTED TO THE GRADUATE SCHOOL
IN PARTIAL FULFILLMENT OF THE REQUIREMENTS

for the degree

DOCTOR OF PHILOSOPHY

Field of Physics and Astronomy

By

Zhigang Jiang

EVANSTON, ILLINOIS

June 2005

ABSTRACT

Thermal Transport Near The Normal-Metal/Superconductor Interface In Mesoscopic Devices

Zhigang Jiang

Thermal transport properties, *i.e.*, thermal conductance and thermopower, have been studied experimentally in mesoscopic proximity-coupled normal-metal devices. These devices essentially consist of a normal metal in proximity to a superconductor, with dimensions comparable to the characteristic lengths related to the physics of interest. These samples were patterned by multi-layer electron-beam lithography, and measured at low temperatures using an Oxford Kelvinox 300 dilution refrigerator and a Janis ^{3}He refrigerator.

It is well-known that, in the elastic-scattering dominated regime, the ratio of the thermal to the electric conductance of a normal metal is proportional to the temperature, the so-called Wiedemann-Franz law. However, it has been found in our experiments that the thermal conductance of the proximity-coupled normal metal is strongly suppressed at low temperatures, deviating from its normal state value (the value predicted by Wiedemann-Franz law). In another words, the Wiedemann-Franz law breaks down in the proximity regime. In contrast to the strong suppression in

the thermal conductance, the magnitude of the thermopower of such devices is much larger than an equivalent normal-metal system. Both the thermal conductance and the thermopower oscillate as a function of magnetic flux with a fundamental period corresponding to one flux quantum $\Phi_0 = h/2e$. While the thermal conductance shows oscillations symmetric with the magnetic field, the symmetry of the thermopower oscillations can be either symmetric or anti-symmetric.

In addition to the experimental studies, numerical simulations have been performed on the sample geometries using the quasiclassical theory of superconductivity. Qualitative agreement with the experimental results is obtained.

Beside thermal transport near the normal-metal/superconductor interface, spin transport through a ferromagnet/superconductor interface also has been studied. The differential resistance of the interfaces shows asymmetric structure as a function of the voltage bias across it, which can be understood as a consequence of spin-polarized electron transport from the ferromagnet to the superconductor. Close to the interface, the superconducting proximity effect in the ferromagnet and the charge-imbalance effect in the superconductor have been investigated as well.

Acknowledgements

It is my honor to acknowledge the assistance and encouragement of many people.

First and foremost, I would like to thank my adviser, Prof. Venkat Chandrasekhar, for patiently teaching me from lithography, low temperature measurements to numerical simulations. His exceptional skills and deep physical insights have enhanced my understanding of physics. Although he failed to convert me from a tea lover to a coffee drinker in six years, he indeed leads me to the way of experimentalist.

I also want to thank my ten-years friend and colleague, Zhengfan Zhang, for sharing all invaluable experience. He is the one who can help me transfer liquid helium at 2:00 AM, and then give me a ride home at 3:00 AM.

I am greatly indebted to the former postdoctor, Dr. Dmitriy Dikin, for my early research work. He has gladly provided me with his knowledge of experimental physics.

Paul Cadden-Zimansky, graduate student in the lab. He always asks good questions and pushes me to learn more.

Prof. James Sauls, for opening the door of Green's function technique. I would like to appreciate the discussions on my thermal conductance measurements with him and his group members, Erhai Zhao and Dr. Tomas Löfwander. Particularly, Erhai Zhao, my theoretical consultant and good friend.

Prof. John Ketterson, for useful and enjoyable discussions on my experimental results, and also for sharing many equipments.

Dr. Sukkoo Jung and Hochul Lim, for invaluable information on lithography.

Prof. Jonghwa Eom, the former student. I enjoy our collaboration in the summer of 2002 and all interesting discussions.

Thank other group members: Dr. José Aumentado, Dr. Sergey Rozhok, Dr. Dmitry Ruzmetov and Dr. Yongho Seo.

Thank Prof. Guillaume Gervais to introduce me to the world of two-dimensional electron gas and fractional quantum hall effect.

I should not forget to thank Prof. Vitali Metlushko and Prof. Victor Moshchalkov for the collaboration in studying the pinning effect in superconducting films.

Finally, I would like to thank my parents for their unceasing support and cheerfulness.

Contents

List of Tables

List of Figures

CHAPTER 1

Introduction

1.1. Thermal transport in normal-metal/superconductor heterostructures

In the past two decades, the electrical characteristics of mesoscopic normal-metal/superconductor (NS) heterostructures have been studied extensively (see for example: [**1, 2**]). In a proximity-coupled normal metal, two effects, namely the superconducting proximity effect and the quantum interference effect, have attracted much interest [**3, 4, 5, 6, 7**]. The superconducting proximity effect reflects the modification of the interactions between electrons inside the normal metal due to the proximity of the superconductor [**8, 9**]. Generally speaking, there are two mechanisms in this regime: (1) the superconductor introduces pair correlations into the normal-metal electrons, which reduce the resistance of the normal metal at a temperature below the transition temperature T_c of the superconductor; (2) at very low temperatures, the reduction of the density of states (DOS) of electrons in the normal metal increases the resistance and results in the so-called re-entrant behavior. The quantum interference effect, on the other hand, describes the phase coherence nature of electrons in such devices, and stems from the process of Andreev reflection [**10**]: at temperatures well below the gap of the superconductor, $k_B T << \Delta$, an electron in the normal metal cannot be transmitted through the NS interface, but is reflected as a coherent hole with the simultaneous generation of a Cooper pair in the superconductor.

In spite of the abundance of interesting physics discovered in the electrical transport measurements, the investigation of the thermal properties of such devices is still in its infancy, especially experimental studies. This fact is due to technical and physical reasons. Technically speaking, thermal transport measurements are one order of magnitude more difficult than electrical transport measurements. For instance, to know the temperature distribution in mesoscopic samples, submicron or even nanometer scale thermometers are required to measure the local electron temperature. In contrast to the technical difficulties, which may be overcome by improving fabrication techniques and developing new measurement methods, the physical reasons are more fundamental, because the main argument here is that whether or not one can calculate thermal characteristic parameters based on the electrical transport measurements. In another words, is it necessary to do thermal transport measurements? The typical example is that the thermal conductance can be calculated by Wiedemann-Franz law [**11**], knowing the conductance and the temperature of the sample. We will show in this thesis that, in a proximity-coupled normal metal, the Wiedemann-Franz law breaks down. The thermopower may also oscillate with a different symmetry as a function of magnetic field compared with the conductance oscillations. Hence, it is necessary to employ thermal transport measurements, which may bring additional information about the interactions between electrons in the proximity-coupled normal metal and probably show new physics.

The main goal of this thesis is to study the superconducting proximity effect and the quantum interference effect in the thermal properties (the thermal conductance and the thermopower) of proximity-coupled normal-metal devices. In fact, the device studied is the so-called Andreev interferometer, which is a hybrid loop with one normal-metal arm and one superconducting arm.

1.1.1. Thermal conductance of Andreev interferometers

Thermal conductance is defined by the ratio of the thermal current through the sample to the temperature differential across the sample under the condition that there is no electrical current flowing in the sample [**12**]. It is analogous to the electric conductance, with thermal energy being carried rather than electric charge. Many normal metals, such as Cu, Ag and Au, are good thermal conductors. However, for a pure superconductor, the thermal conductance is suppressed dramatically at a temperature well below T_c, which makes a superconductor a very poor thermal conductor at low temperatures. The question investigated in this thesis is: what is the situation for a normal metal coupled to a superconductor?

Historically, thermal conductance of an Andreev interferometer was first measured by Dikin *et al.* in our group [**13**]. A clear suppression in the thermal conductance at a temperature below T_c was observed. However, as pointed out by us in Ref. [**13**] and a later theoretical study by Bezuglyi *et al.* [**14**], the sample measured there was actually not in the true proximity regime, the reduced thermal conductance may have been due to the well-known suppression of thermal conductance in a conventional superconductor, rather than a proximity effect phenomenon.

In this thesis, the thermal conductance of Andreev interferometers has been measured quantitatively in the true proximity regime at different temperatures and in different magnetic fields, with many technical improvements compared with the previous measurement. Furthermore, as we will show, for the first time, thermal conductance oscillations (as a function of magnetic field) have been observed [**15**]. The period of the oscillations corresponds to one flux quantum $\Phi_0 = h/2e$ through the loop of Andreev interferometer.

In addition, the thermal conductance of Andreev interferometers has also been investigated theoretically and numerically [**16**] by using the quasiclassical theory of superconductivity. In contrast to Bezuglyi's work, our simulations particularly focus on the proximity regime and predict the thermal conductance of the two types of Andreev interferometers relevant to the experiments. The numerical results are qualitatively in agreement with our experimental data.

1.1.2. Thermopower of Andreev interferometers

Thermopower is defined as the ratio of the induced thermal voltage differential across the sample to the applied temperature differential, also under the condition that there is no electrical current flowing in the sample [**12**]. In the framework of Fermi liquid theory, the thermopower stems from breaking of electron-hole symmetry, and arises from the second term in the Sommerfeld expansion of the Fermi distribution function. For a typical metal, it is usually very small.

Historically, the thermopower of Andreev interferometers was measured first by Eom *et al.* [**17**], a former student in our group. It was found that the thermopower oscillates as a function of magnetic field with a period of $\Phi_0 = h/2e$. The oscillations can be either symmetric or anti-symmetric with respect to the magnetic field, depending on the geometry of the sample. Moreover, the temperature dependence of the magnitude of the oscillations is non-monotonic. As the temperature drops down from T_c, it first increases and then decreases after reaching a maximum at some intermediate temperature. Phase coherent thermopower oscillations were confirmed later by Dikin *et al.* [**13, 18**] from our group and Parsons *et al.* [**19**] from Petrashov's group.

Spurred by the above experiments, thermopower of Andreev interferometers has attracted much interest from theorists [**20, 21, 22**]. Unfortunately, these theoretical models cannot explain all the experimental data. Six years after phase coherent thermopower oscillations were first reported, the exact reason for the symmetry of the oscillations still remains as a puzzle. However, there is a common theme in these theoretical works, which is that the supercurrent plays an important role in the thermoelectrical transport.

In this thesis, the symmetry of the thermopower oscillations has been further investigated on a device where we have control of the magnitude and direction of the supercurrent. The preliminary results indeed show that, depending on the direction of the supercurrent, the oscillations can be either symmetric or anti-symmetric in the same device [**23**].

1.2. Spin transport in ferromagnet/superconductor heterostructures

There has been continuing interest in the past few years in mesoscopic ferromagnet/superconductor (FS) heterostructures, due to the rich physics involved and its potential applications in industry. However, compared with NS systems, this field is much less mature and many topics remain unexplored. In this thesis, two topics have been examined: (1) differential resistance of mesoscopic FS junctions and (2) superconducting proximity effect in ferromagnets.

Extending the pioneering work of Tedrow and Meservey [**24**], point-contact FS spectroscopy has been studied recently by several groups [**25, 26**]. It has been found that the spin-polarization P in the ferromagnet can be determined by measuring the differential resistance of the FS junction as a function of the voltage bias across it [**27, 28, 29, 30, 31**] and fitting the results to the spin-polarized version of the Blonder, Tinkham, Klapwijk (BTK) theory [**32**]. In Chapter 5, we will present our measurements of differential resistance of mesoscopic FS junctions. We find that the differential resistance is asymmetric even at zero external field. The dips in the differential resistance split at higher magnetic field. This splitting can be understood as arising from a combination of the spin-polarized tunneling through the FS interface and the splitting of the quasi-particle density of states due to the magnetic field [**33**].

There has also been much debate about the length scale in which superconducting proximity effect can be observed in a ferromagnet. In the conventional picture, this length scale should be quite short, because the presence of the large exchange field in ferromagnets would destroy the pair correlations induced by the proximity of the superconductor [**34**]. However, long-range proximity effects in a ferromagnetic have been reported in a number of recent publications [**35, 36, 37, 38, 39, 40**]. Additionally, recent theoretical work also shows that a long-range proximity effect may arise from the triplet component of the superconducting correlations, which are predicted to extend into a ferromagnet to a much longer distance [**41, 42**]. In this thesis, we will report our own measurements of the proximity effect in Ni/Al devices with high transparent interfaces. We found that the total resistance change in the ferromagnet is about 0.07 % of its normal state resistance, much less than 12 % measured by Giroud *et al.* [**40**].

1.3. Overview of this thesis

This thesis is comprised of two parts. Part one is the major part, which describes the thermal transport properties of proximity-coupled normal-metal devices. It includes Chapter 2-4: Chapter 2, a brief introduction of the quasiclassical theory of superconductivity, followed by detailed numerical calculations of the thermal conductance of Andreev interferometers. Chapter 3, technical details of the sample fabrication process and low temperature measurements on mesoscopic devices. Chapter 4, experimental data on the thermal conductance and thermopower measurements, and the comparisons with the results of numerical simulations. Part two (Chapter 5) investigates a separate topic, spin transport through ferromagnet/superconductor interface devices. It is a self-contained chapter, which includes theory overview and experimental results. At the end, this thesis is concluded in Chapter 6 with a summary on both the thermal transport and the spin transport measurements, as well a discussion about the possible directions for the future work.

CHAPTER 2

Theory: Quasiclassical theory of superconductivity

Although a variety of theories have been developed to describe the NS systems, the quassiclassical theory of superconductivity has proved to be a powerful tool to understand both the equilibrium and non-equilibrium properties of such systems. It has essentially become the common language in recent publications related to the thermal properties of NS devices [**14, 21, 22, 43**]. In this chapter, we will first present a detailed derivation of the Usadel equation and the related kinetic equations in the language of the quasiclassical Green's function and the Keldysh technique. Then, we will solve them numerically to calculate the thermal conductance of Andreev interferometers with the geometries relevant to the sample geometries measured in experiments. Several approximations have been made in this chapter to simplify the problem, based on the fact that we are only interested in the transport properties of quasi-one-dimensional diffusive systems. More details and general discussions can be found in Ref. [**44, 45, 46, 47, 48**].

2.1. Usadel equation

2.1.1. Quasiclassical Green's function

The starting point of this chapter is the time-ordered Green's function, which can be expressed, in Nambu space (the particle and hole space), as the following

$$\hat{G}(\boldsymbol{r}_1, \boldsymbol{r}_2; t_1, t_2) = -i \left\langle \mathrm{T}\hat{\Psi}(\boldsymbol{r}_1, t_1)\hat{\Psi}^{\dagger}(\boldsymbol{r}_2, t_2)\right\rangle . \tag{2.1}$$

Using the center-of-mass coordinates in space and time and taking the Fourier transformation, we obtain

$$\hat{G}(\boldsymbol{r}_1, \boldsymbol{r}_2; t_1, t_2) \Rightarrow \hat{G}(\boldsymbol{R}, \boldsymbol{r}; T, t) \Rightarrow \hat{G}(\boldsymbol{R}, \boldsymbol{p}; T, E), \tag{2.2}$$

where $\boldsymbol{R} = (\boldsymbol{r}_1 + \boldsymbol{r}_2)/2$, $\boldsymbol{r} = \boldsymbol{r}_1 - \boldsymbol{r}_2$, $T = (t_1 + t_2)/2$, and $t = t_1 - t_2$.

The time-ordered Green's function oscillates as a function of $r = |\boldsymbol{r}_1 - \boldsymbol{r}_2|$ on a scale of the Fermi wavelength λ_F, which is typically several angstroms, much smaller than the characteristic length scale of the physics of interest. Hence, it is a proper approximation to integrate out the dependence on r, in order to reduce the number of variables. This is the so-called quasiclassical approximation. In addition, the electrons involved in the transport are primarily on the Fermi surface. Therefore, we can rewrite the above Green's function as $\hat{G}(\boldsymbol{R}, \xi, \hat{\boldsymbol{v}}_F; T, E)$, where ξ and $\hat{\boldsymbol{v}}_F$ are related to the magnitude of the momentum and the direction of velocity at the Fermi surface respectively. The quasiclassical Green's function is then defined as

$$\hat{g}(\boldsymbol{R}, \hat{\boldsymbol{v}}_F; T, E) \equiv \frac{i}{\pi} \int d\xi \; \hat{G}(\boldsymbol{R}, \xi, \hat{\boldsymbol{v}}_F; T, E). \tag{2.3}$$

In our mesoscopic devices, the typical sample dimensions are shorter than the inelastic impurity-scattering length of electrons. So, we can neglect the inelastic scattering, and only consider the elastic scattering. In the Born approximation, the self-energy of the elastic impurity-scattering reads

$$\hat{\Sigma}(\boldsymbol{R}, \hat{\boldsymbol{p}}, T, E)_{imp} = n_{imp} \left\langle \int \frac{d^3p'}{(2\pi)^3} \left|v(\hat{\boldsymbol{p}} \cdot \hat{\boldsymbol{p}}')\right|^2 \hat{G}(\boldsymbol{R}, \boldsymbol{p}'; T, E) \right\rangle_{\boldsymbol{p}_F}, \tag{2.4}$$

where n_{imp} is the impurity concentration and $\langle \ldots \rangle_{\boldsymbol{p}_F}$ denotes the averaging over the Fermi surface. Since $\left| v(\hat{\boldsymbol{p}} \cdot \hat{\boldsymbol{p}}') \right|^2$ normally varies slowly as a function of the magnitude of the momentum $p' = |\boldsymbol{p}'|$ near the Fermi surface, one can introduce an elastic scattering time τ,

$$\tau^{-1} = 2\pi n_{imp} N_0 \int d\Omega_{\boldsymbol{p}'} \left| v(\hat{\boldsymbol{p}} \cdot \hat{\boldsymbol{p}}') \right|^2 , \tag{2.5}$$

where $N_0 = mk_F/2\pi^2$ is the DOS per spin and on the Fermi surface $p = p' = k_F$. Consequently,

$$\hat{\Sigma}(\boldsymbol{R}, \hat{\boldsymbol{p}}, T, E)_{imp} = \frac{1}{2\pi\tau} \left\langle \int d\xi \; \hat{G}(\boldsymbol{R}, \boldsymbol{p}'; T, E) \right\rangle_{\boldsymbol{p}_F} , \tag{2.6}$$

where we use the substitution

$$\int \frac{d^3 p'}{(2\pi)^3} \longmapsto N_0 \int d\xi \int d\Omega_{\boldsymbol{p}'} . \tag{2.7}$$

Note that $\xi = p'^2/2m - \mu$, where m is the effective mass and μ is the chemical potential.

In the rest of this chapter, because we are not going to solve time-dependent problems, we will drop the time variable T for simplicity.

2.1.2. Eilenberger equation

The equation of motion for the quasiclassical Green's function is the so-called Eilenberger equation,

$$\left[\hat{g}_0^{-1} - \hat{\sigma}, \hat{g} \right] = 0, \tag{2.8}$$

where $\hat{\sigma}$ is the self-energy. In general, $\hat{g}_0$ can be written as

$$\hat{g}_0^{-1} = E\hat{\tau}_3 + i\boldsymbol{v}_F \hat{\partial}_R - e\phi + \mu, \tag{2.9}$$

where $\hat{\tau}_3$ is the third Pauli spin matrix[1] and $\hat{\partial}_R = \nabla_R - ie\boldsymbol{A}(\boldsymbol{R})$ is the gauge-invariant spatial derivative. The last two terms on the right side of Eqn. (2.9), *i.e.*, the electric potential and the chemical potential, commute with $\hat{g}$, so we can simply drop them after we insert Eqn. (2.9) into Eqn. (2.8). In addition, the self-energy term $\hat{\sigma}$ in Eqn. (2.8) consists of two contributions. One is the electron-phonon scattering self-energy (pair potential), $-\hat{\Delta}$, which is responsible for superconductivity. Another one is the elastic impurity-scattering self-energy $\hat{\Sigma}_{imp}$. Hence, we can rewrite the Eilenberger equation as the following

$$-\left[\boldsymbol{v}_F\hat{\partial}, \hat{g}\right] = \left[-iE\hat{\tau}_3 - i\hat{\Delta} + \frac{1}{2\tau}\left\langle\hat{g}\right\rangle_{\boldsymbol{v}_F}, \hat{g}\right], \tag{2.10}$$

where $\hat{\Delta}$ is given by

$$\hat{\Delta} = \begin{pmatrix} 0 & \Delta \\ -\Delta^* & 0 \end{pmatrix}. \tag{2.11}$$

It also should be noted that the quasiclassical Green's function are normalized, *i.e.*, $\hat{g}\hat{g} = \hat{1}$. If we define the matrix elements of $\hat{g}$ as

$$\hat{g} = \begin{pmatrix} g & f \\ f\dagger & -g \end{pmatrix}, \tag{2.12}$$

then we obtain $g^2 + ff\dagger = 1$.

2.1.3. Keldysh technique

The Keldysh Green's function technique is a very useful technique to study both the equilibrium and non-equilibrium phenomena. In this method, a Green's function is

[1]In this thesis, $\hat{\tau}_i$ $(i = 0 \dots 3)$ represents the ith Pauli spin matrix.

normally written in a matrix form,

$$\check{G} = \begin{pmatrix} \hat{G}^R & \hat{G}^K \\ 0 & \hat{G}^A \end{pmatrix}, \tag{2.13}$$

where $\hat{G}^R$, $\hat{G}^A$ and $\hat{G}^K$ are retarded, advanced and Keldysh Green's functions respectively. The diagonal terms, the retarded and advanced Green's functions, represent the spectral, *i.e.*, equilibrium properties of the system; while the off-diagonal term, the Keldysh Green's function, is related to the non-equilibrium distribution function.

The purpose of developing these Green's functions is to calculate physical quantities and understand the physics behind them. The so-called Kadanoff functions have been introduced to do so [**49**],

$$\hat{G}^{>}(1,2) = i\left\langle \Psi\dagger(2)\Psi(1)\right\rangle, \; \hat{G}^{<}(1,2) = -i\left\langle \Psi(1)\Psi\dagger(2)\right\rangle. \tag{2.14}$$

In the Keldysh space, the retarded, advanced and Keldysh Green's functions can be expressed as linear combinations of the Kadanoff functions,

$$\begin{aligned} \hat{G}^R(1,2) &= \theta(t1-t2)\left[\hat{G}^{<}(1,2) - \hat{G}^{>}(1,2)\right], \\ \hat{G}^A(1,2) &= -\theta(t2-t1)\left[\hat{G}^{<}(1,2) - \hat{G}^{>}(1,2)\right], \\ \hat{G}^K(1,2) &= \hat{G}^{<}(1,2) + \hat{G}^{>}(1,2). \end{aligned} \tag{2.15}$$

Since the physical quantities can be written in terms of $\hat{G}^{>}$ and $\hat{G}^{<}$, it is trivial to transfer them to $\hat{G}^R$, $\hat{G}^A$ and $\hat{G}^K$.

Within the quasiclassical approximation, again we use $\check{g}$ (or $\hat{g}$) instead of $\check{G}$ (or $\hat{G}$), based on the transmission of Eqn. (2.3). $\check{g}$ satisfies the Eilenberger equation

(2.8) and the normalization condition $\check{g}\check{g} = \check{1}$. Hence, the expectation values of the physical quantities can be expressed by the matrix components of $\check{g}$: $\hat{g}^R$, $\hat{g}^A$ and $\hat{g}^K$. For example, the local DOS of electrons, the electrical current, the thermal current, and the superconducting gap are [**46, 47, 48**]

$$N(\boldsymbol{R}, E) = N_0 \Re \left[\int d\Omega_{\boldsymbol{p}} \hat{g}^R(\boldsymbol{R}, \hat{\boldsymbol{v}}_F, E) \right], \tag{2.16a}$$

$$\boldsymbol{j}(\boldsymbol{R}) = -\frac{eN_0}{4} \int dE \int d\Omega_{\boldsymbol{p}} \mathrm{Tr} \left[\boldsymbol{v}_F \hat{\tau}_3 \hat{g}^K(\boldsymbol{R}, \hat{\boldsymbol{v}}_F, E) \right], \tag{2.16b}$$

$$\boldsymbol{j}^T(\boldsymbol{R}) = -\frac{N_0}{4} \int dE \int d\Omega_{\boldsymbol{p}} \; E \mathrm{Tr} \left[\boldsymbol{v}_F \hat{g}^K(\boldsymbol{R}, \hat{\boldsymbol{v}}_F, E) \right], \tag{2.16c}$$

$$\Delta(\boldsymbol{R}) = N_0 \frac{\lambda}{4} \int dE \int d\Omega_p \hat{g}^K(\boldsymbol{R}, \hat{\boldsymbol{v}}_F, E)_{12}. \tag{2.16d}$$

2.1.4. Dirty limit

In metallic mesoscopic samples, the concentration of impurities is normally very high, so that the mean free path of electrons l_e is much shorter than the sample dimensions. In another words, the electron motion is diffusive, *i.e.*, the electrons feel strong elastic impurity scattering during the transport. This is the so-called *dirty limit*. In this limit, the Green's functions are nearly isotropic, therefore we can expand them in spherical harmonics

$$\check{g}(\boldsymbol{R}, \hat{\boldsymbol{v}}_F, E) = \check{g}_s(\boldsymbol{R}, E) + \hat{\boldsymbol{v}}_F \check{g}_p(\boldsymbol{R}, E) + (\textit{higher order terms}), \tag{2.17}$$

where $\check{g}_s(\boldsymbol{R}, E)$ is the isotropic term (s-wave expansion) obtained from the angular average of the quasiclassical Green's function, and $\hat{\boldsymbol{v}}_F \check{g}_p$ is the first order expansion (p-wave expansion). As a consequence of dirty limit, $\hat{\boldsymbol{v}}_F \check{g}_p << \check{g}_s$ and all the higher order terms in the expansion are negligible.

Following the same procedure, one can expand the self-energy as

$$\check{\sigma} = \check{\sigma}_s + \check{\sigma}'_s + \hat{\boldsymbol{v}}_F \check{\sigma}_p. \tag{2.18}$$

The first two terms are s-wave expansion terms

$$\begin{aligned} \check{\sigma}_s &\cong -\frac{i}{2\tau}\check{g}_s, \\ \check{\sigma}'_s &= -\check{\Delta}, \end{aligned} \tag{2.19}$$

where $\cong$ means we only consider the contribution from the zero order expansion, and

$$\check{\Delta} = \begin{pmatrix} \hat{\Delta} & 0 \\ 0 & \hat{\Delta} \end{pmatrix}. \tag{2.20}$$

The p-wave term is [2]

$$\begin{aligned} \hat{\boldsymbol{v}}_F \check{\sigma}_p &\cong -i\pi n_{imp} N_0 \left(\int d\Omega_{\boldsymbol{p}'} \left| v(\hat{\boldsymbol{p}} \cdot \hat{\boldsymbol{p}}') \right|^2 \hat{\boldsymbol{p}}' \right) \check{g}_p, \\ \check{\sigma}_p &\cong -\frac{i}{2}(\frac{1}{\tau} - \frac{1}{\tau_{tr}})\check{g}_p, \end{aligned} \tag{2.21}$$

where τ_{tr} is called transport time and defined by

$$\tau_{tr}^{-1} = 2\pi n_{imp} N_0 \int d\Omega_{\boldsymbol{p}'} \left| v(\hat{\boldsymbol{p}} \cdot \hat{\boldsymbol{p}}') \right|^2 (1 - \hat{\boldsymbol{p}} \cdot \hat{\boldsymbol{p}}'). \tag{2.22}$$

Furthermore, $\check{g}_0^{-1}$ can also be expressed as follows

$$\begin{aligned} \check{g}_0^{-1} &= \check{g}_{0,s}^{-1} + \hat{\boldsymbol{v}}_F \check{g}_{0,p}^{-1} \\ &= E\check{\tau}_3 + \hat{\boldsymbol{v}}_F \cdot (iv_F \hat{\partial}), \end{aligned} \tag{2.23}$$

[2]At the Fermi surface, $\hat{\boldsymbol{v}}_F$ and $\hat{\boldsymbol{p}}$ are identical. They denote the direction of velocity or momentum.

where

$$\check{\tau}_3 = \begin{pmatrix} \hat{\tau}_3 & 0 \\ 0 & \hat{\tau}_3 \end{pmatrix}. \tag{2.24}$$

It should be pointed out that the Keldysh technique is not restricted to the dirty limit. It is a very general method, which can be applied in the ballistic regime as well without many modifications. In addition, for the diffusive regime, one can also include the inelastic scattering and the spin of electrons into the above discussions.

2.1.5. Usadel equation and parameterization

Using the s-wave and p-wave expansions derived in the above section, the Eilenberger equation (2.8) reduces to its dirty limit version, the Usadel equation. As we will see later, after parameterization, the Usadel equation further reduces to a relatively simple form. Although this equation has analytical solutions in some simple problems, it needs to be solved numerically in most cases.

Inserting Eqn. (2.17), (2.18) and (2.23) into the Eilenberger equation (2.8) and separating the even terms and the odd terms with respect to $\hat{\boldsymbol{v}}_F$, one obtains

Even terms:

$$\left[E\check{\tau}_3 + \check{\Delta},\ \check{g}_s\right] + i\frac{v_F}{3}\left[\hat{\partial},\ \check{g}_p\right] = 0; \tag{2.25}$$

odd terms:

$$\left[iv_F\hat{\partial} - \frac{i}{2\tau_{tr}}\check{g}_p,\ \check{g}_s\right] + \left[E\check{\tau}_3 + \check{\Delta},\ \check{g}_p\right] = 0, \tag{2.26}$$

where the last term can be neglected, because in the dirty limit, $1/\tau_{tr} >> \Delta, E$.

In addition, we can use the normalization condition $\check{g}\check{g} = \check{1}$, *i.e.*,

$$\check{g}_s\check{g}_s = \check{1},\ \{\check{g}_s,\ \check{g}_p\} = 0, \tag{2.27}$$

to further simplify the above Eqn. (2.25) and (2.26). Insert Eqn. (2.27) into Eqn. (2.26), one gets

$$\check{g}_p = -\tau_{tr} v_F \check{g}_s \left[\hat{\partial},\ \check{g}_s\right]. \tag{2.28}$$

Finally, inserting Eqn. (2.28) into Eqn. (2.25), we obtain the Usadel equation

$$\left[E\check{\tau}_3 + \check{\Delta},\ \check{g}_s\right] - iD\hat{\partial}(\check{g}_s\hat{\partial}\check{g}_s) = 0, \tag{2.29}$$

where $D = v_F^2 \tau_{tr}/3$ is the electric diffusion coefficient.

Next, introduce a way to parameterize the retarded quasiclassical Green's function which makes use of all available symmetries,

$$\begin{aligned}\hat{g}_s^R &= i\mathrm{sinh}\theta\mathrm{sin}\phi(\hat{\tau}_1) + i\mathrm{sinh}\theta\mathrm{cos}\phi(\hat{\tau}_2) + \mathrm{cosh}\theta(\hat{\tau}_3) \\ &= \begin{pmatrix} \mathrm{cosh}\theta & \mathrm{sinh}\theta e^{i\phi} \\ -\mathrm{sinh}\theta e^{-i\phi} & -\mathrm{cosh}\theta \end{pmatrix},\end{aligned} \tag{2.30}$$

where θ and ϕ are both complex variables and ϕ is related to the phase of the superconducting order parameter. Since $\hat{g}_s^A = -\hat{\tau}_3(\hat{g}_s^R)^\dagger\hat{\tau}_3$, it reads

$$\hat{g}_s^A = \begin{pmatrix} -\mathrm{cosh}\theta^* & -\mathrm{sinh}\theta^* e^{i\phi^*} \\ \mathrm{sinh}\theta^* e^{-i\phi^*} & \mathrm{cosh}\theta^* \end{pmatrix}. \tag{2.31}$$

Then, one can get

$$\hat{\partial}(\hat{g}_s^R\hat{\partial}\hat{g}_s^R) = \begin{pmatrix} X_{11} & X_{12} \\ X_{21} & X_{22} \end{pmatrix}, \tag{2.32}$$

where

$$
\begin{aligned}
X_{11} &= i\text{sinh}(2\theta)\partial\theta\partial\phi + i\text{sinh}^2\theta(\partial^2\phi) \\
X_{12} &= \left[\partial^2\theta + 2i\text{cosh}^2\theta\partial\theta\partial\phi + \frac{i}{2}\text{sinh}(2\theta)(\partial^2\phi) - \frac{1}{2}\text{sinh}(2\theta)(\partial\phi)^2\right] e^{i\phi} \\
X_{21} &= X_{12}(\phi \Rightarrow -\phi) \\
X_{22} &= -X_{11}.
\end{aligned}
\tag{2.33}
$$

Inserting the above equations into the matrix equation (2.29) and only considering the first diagonal equation, one can obtain the parameterized Usadel equation immediately. Since we are primarily interest in the proximity-coupled normal-metal systems, we will set the superconducting gap in the normal metal to zero $\Delta = 0$ in the following derivation. A general formula will be shown at the end of this section.

After all the efforts above, the Usadel equation Eqn. (2.29) turns into

$$
iD \begin{pmatrix} X_{11} & X_{12} \\ X_{21} & X_{22} \end{pmatrix} = 2E \begin{pmatrix} 0 & \text{sinh}\theta e^{i\phi} \\ \text{sinh}\theta e^{-i\phi} & 0 \end{pmatrix}. \tag{2.34}
$$

For a one-dimensional sample, the above matrix equation can be expressed by two equivalent equations,

$$
\partial_x(\text{sinh}^2\theta\partial_x\phi) = 0, \tag{2.35a}
$$

$$
D\partial_x^2\theta + 2iE\text{sinh}\theta - \frac{D}{2}\text{sinh}(2\theta)(\partial_x\phi)^2 = 0, \tag{2.35b}
$$

where the first equation is related to the continuity equation of the spectral current $\partial_x j_\epsilon = 0$, since by the definition the energy-dependent spectral current is $j_\epsilon \equiv$

$\sinh^2\theta\partial_x\phi$. Notice that the above equations can be easily modified to three-dimensional systems.

In a more general problem, the Usadel equation reads

$$D\partial_x(\sinh^2\theta\partial_x\phi) - 2i\Im(\Delta)\sinh\theta = 0, \tag{2.36a}$$

$$D\partial_x^2\theta + 2iE\sinh\theta - \frac{D}{2}\sinh(2\theta)(\partial_x\phi)^2 - 2i\Re(\Delta)\cosh\theta = 0. \tag{2.36b}$$

It needs to be pointed out that, if the gap Δ has an imaginary component, according to Eqn. (2.36a), the spectral current j_ϵ would not be conserved any more. Then, a conversion between the supercurrent and the quasiparticle current would expect to be seen. As we will see later, this conversion provides the zero order contribution to the thermal voltage of Andreev interferometers [**22**].

2.1.6. Kinetic equations and parameterization

Although the Usadel equation has offered us spectral information of the system, which potentially can tell us the DOS of electrons, we need more information (especially the distribution function) to complete our understanding of the system and calculate the physical quantities of interest. The distribution function can be obtained from the so-called kinetic equations. In contrast to the Usadel equation, the kinetic equations are related to the Keldysh Green's function $\hat{g}^K$, hence the off-diagonal term in Eqn. (2.29).

The normalization condition $\check{g}\check{g} = \check{1}$ suggests the Keldysh Green's function satisfies the following condition:

$$\hat{g}^K = \hat{g}^R\hat{h} - \hat{h}\hat{g}^A, \tag{2.37}$$

where $\hat{h}$ is called distribution matrix. The kinetic equation of motion for $\hat{h}$ can be derived from the off-diagonal term of Eqn. (2.29) as

$$\partial\left[\partial\hat{h} + \hat{g}^R(\partial\hat{g}^R)\hat{h} - \hat{h}\hat{g}^A(\partial\hat{g}^A) - \hat{g}^R(\partial\hat{h})\hat{g}^A\right] = 0. \tag{2.38}$$

Again, we set $\Delta = 0$ in normal metal.

Furthermore, based on the symmetry requirement, we can choose $\hat{h}$ to be diagonal [**50, 51**]

$$\hat{h} = h_L\hat{\tau}_0 + h_T\hat{\tau}_3, \tag{2.39}$$

where $h_{L(T)}$ is the longitudinal (transverse) component of the distribution function. Consequently, we can rewrite the kinetic equation as

$$\begin{aligned}&\partial\left[(\hat{g}^R\partial\hat{g}^R - \hat{g}^A\partial\hat{g}^A)h_L + (1-\hat{g}^R\hat{g}^A)\partial h_L\right]\hat{\tau}_0\\ &+\partial\left[(\hat{g}^R\partial\hat{g}^R - \hat{\tau}_3\hat{g}^A\partial\hat{g}^A\hat{\tau}_3)h_T + (1-\hat{g}^R\hat{\tau}_3\hat{g}^A\hat{\tau}_3)\partial h_T\right]\hat{\tau}_3 = 0.\end{aligned} \tag{2.40}$$

Now, do the following actions onto the above equation:

(1) $\mathrm{Tr}\left[(\text{left side})\cdot\hat{\tau}_3\right]$:

$$\begin{aligned}&\partial\left\{\mathrm{Tr}\left[(\hat{g}^R\partial\hat{g}^R - \hat{g}^A\partial\hat{g}^A)\hat{\tau}_3\right]h_L - \mathrm{Tr}\left[\hat{g}^R\hat{g}^A\hat{\tau}_3\right]\partial h_L\right\}\\ &+\partial\left\{\mathrm{Tr}\left[1-\hat{g}^R\hat{\tau}_3\hat{g}^A\hat{\tau}_3\right]\partial h_T\right\} = 0,\end{aligned} \tag{2.41}$$

where

$$\begin{aligned}\mathrm{Tr}\left[\hat{g}^{R(A)}\partial\hat{g}^{R(A)}\right] &= \frac{1}{2}\mathrm{Tr}\left[\hat{g}^{R(A)}\partial\hat{g}^{R(A)}\right] + \frac{1}{2}\mathrm{Tr}\left[\partial\hat{g}^{R(A)}\cdot\hat{g}^{R(A)}\right]\\ &= \frac{1}{4}\mathrm{Tr}\left[\partial(\hat{g}^{R(A)})^2\right] = 0.\end{aligned} \tag{2.42}$$

(2) $\mathrm{Tr}\left[(\text{left side})\cdot\hat{\tau}_0\right]$:

$$\partial\left\{\mathrm{Tr}\left[(1-\hat{g}^R\hat{g}^A)\right]\partial h_L - \mathrm{Tr}\left[\hat{g}^R\hat{\tau}_3\hat{g}^A\right]\partial h_T\right\}$$
$$+\partial\left\{\mathrm{Tr}\left[(\hat{g}^R\partial\hat{g}^R-\hat{g}^A\partial\hat{g}^A)\hat{\tau}_3\right]h_T\right\}=0. \tag{2.43}$$

Then, after define the following notations,

$$Q=\frac{1}{4}\mathrm{Tr}\left[(\hat{g}^R\partial\hat{g}^R-\hat{g}^A\partial\hat{g}^A)\hat{\tau}_3\right], \tag{2.44}$$
$$M_{ij}=\frac{1}{4}\mathrm{Tr}\left[\delta_{ij}-\hat{g}^R\hat{\tau}_i\hat{g}^A\hat{\tau}_j\right], \tag{2.45}$$

Eqn. (2.41) and (2.43) turn to a beautiful format

$$\partial\left\{Q\cdot h_L+M_{03}\cdot\partial h_L+M_{33}\cdot\partial h_T\right\}=0, \tag{2.46a}$$

$$\partial\left\{Q\cdot h_T+M_{30}\cdot\partial h_T+M_{00}\cdot\partial h_L\right\}=0. \tag{2.46b}$$

We will see later that these two equations are actually the continuity equations for the electrical current and thermal current, which represent the conservation of particle number and energy respectively.

In addition, the second terms in Eqn. (2.46) describe the contributions from broken particle-hole symmetry. In much of the literature, this contribution is dropped out while calculating the electrical properties by assuming equal number of electrons and holes in the studied systems. However, if we consider the thermal properties of those systems, such as the thermopower, it has been shown recently that these two terms give rise to a detectable contribution [**22**]. Furthermore, the first and third terms in Eqn. (2.46) represent the contributions due to the occupation of current-carrying states and ordinary diffusion, which are related to the supercurrent and normal current respectively. In terms of θ and ϕ, Q has a clear physical meaning,

$$Q = \frac{1}{2}\left[i\sinh^2\theta\partial\phi - i\sinh^2\theta^*\partial\phi^*\right] = -\Im\left[\sinh^2\theta\partial\phi\right], \tag{2.47}$$

i.e., $Q = -\Im\left[j_\epsilon\right]$, related to the imaginary part of the spectral supercurrent. According to the Usadel equation (2.35a), $\partial Q = 0$ in normal metals. In addition to Eqn. (2.47), we can also express M_{ij} in terms of θ and ϕ

$$M_{00} = \frac{1}{2}\left[1 + \cosh\theta\cosh\theta^* - \sinh\theta\sinh\theta^*\cosh(2\Im(\phi))\right], \tag{2.48a}$$

$$M_{33} = \frac{1}{2}\left[1 + \cosh\theta\cosh\theta^* + \sinh\theta\sinh\theta^*\cosh(2\Im(\phi))\right], \tag{2.48b}$$

$$M_{03} = \frac{1}{2}\sinh\theta\sinh\theta^*\sinh(2\Im(\phi))), \tag{2.48c}$$

$$M_{30} = -\frac{1}{2}\sinh\theta\sinh\theta^*\sinh(2\Im(\phi)). \tag{2.48d}$$

If we consider the superconducting gap Δ while deriving the Eqn. (2.46), we can rewrite the above kinetic equations into a more general form

$$\partial\left\{Qh_L + M_{03}\partial h_L + M_{33}\partial h_T\right\} = \frac{i}{4D}\left[h_L\mathrm{Tr}\left\{\tau^3[\hat{g}_s^R - \hat{g}_s^A, \hat{\Delta}]\right\} - 2h_T\mathrm{Tr}\left\{\hat{\Delta}(\hat{g}_s^R + \hat{g}_s^A)\right\}\right], \tag{2.49a}$$

$$\partial\left\{Qh_T + M_{30}\partial h_T + M_{00}\partial h_L\right\} = 0. \tag{2.49b}$$

Note that the kinetic equations, Eqn. (2.46) or (2.49), can be easily parameterized by using Eqn. (2.30) and (2.31). We will come back to it later while solving specific problems in the second half of this chapter.

2.1.7. Boundary conditions

2.1.7.1. Boundary conditions for the Usadel equation

The sample of interest in our experiments (for example: a one-dimensional normal-metal wire) is normally connected to a metal pad of large area that acts as a reservoir to cool down electrons. In the following simulations, we will use *ideal* reservoir boundary conditions, in which we assume the electrons in the reservoirs are in an equilibrium state and have a well-defined uniform temperature T and electric potential V. In terms of θ and ϕ, the *ideal* reservoir boundary conditions can be expressed as

$$\hat{g}^R = \frac{1}{[(E+i\delta)^2 - \Delta^2]^{1/2}} \begin{pmatrix} E & \Delta e^{i\phi} \\ -\Delta e^{-i\phi} & -E \end{pmatrix}, \tag{2.50}$$

where E is the quasiparticle energy and δ is an infinitesimally positive number, called the pair breaking term. In some papers, $\delta \to 0_+$, and the above boundary conditions of θ reduce to a simple form

$$\cosh\theta = \frac{E}{\sqrt{E^2 - \Delta^2}}, \tag{2.51}$$

i.e.,

$$\theta = \begin{cases} -\frac{\pi}{2}i + \frac{1}{2}\ln\frac{\Delta+E}{\Delta-E} & \text{if } E < \Delta \\ \frac{1}{2}\ln\frac{E+\Delta}{E-\Delta} & \text{if } E > \Delta \end{cases}. \tag{2.52}$$

In a normal reservoir, $\Delta = 0$, so that $\hat{g}^R = \hat{\tau}_3$, $\theta = 0$.

The value of ϕ in a superconducting reservoir is the macroscopic phase of the superconductor. In a normal reservoir, however, it does not have a physical meaning. It obeys $\partial\phi = 0$ to ensure that supercurrent does not exist in such reservoirs.

In reality, the interface between a normal-metal wire and a superconducting reservoir cannot be perfect. The effect of the barrier resistance of NS interface was first studied by Zaitsev [**52**], then simplified by Kupriyanov and Lukichev [**53**] for the diffusive case in the limit of low transparency. The boundary conditions of Kupriyanov and Lukichev read

$$v_{F1} D_1 \hat{g}_{s1}(\partial_x \hat{g}_{s1}) = v_{F2} D_2 \hat{g}_{s2}(\partial_x \hat{g}_{s2}), \tag{2.53a}$$

$$\hat{g}_{s1}\partial_x \hat{g}_{s1} = \frac{1}{2r}[\hat{g}_{s1}, \hat{g}_{s2}], \tag{2.53b}$$

where ∂_x denotes the direction from 1 to 2, and $r = R_b/R_N$ is the ratio of the barrier resistance R_b to the normal-metal wire resistance per unit length R_N, which is inversely proportional to the transmission of the interface.

A further study of the boundary conditions of Kupriyanov and Lukichev shows that Eqn. (2.53a) is essentially the continuity equation of Green's function across the interface, while Eqn. (2.53b) is the one related to the barrier resistance. In terms of θ and ϕ, Eqn. (2.53) can be expressed as

$$r \sinh\theta_1(\partial_x \phi_1) = \sinh\theta_2 \sin(\phi_2 - \phi_1), \tag{2.54a}$$

$$r\left[\partial_x \theta_1 + i \sinh\theta_1 \cosh\theta_1(\partial_x\phi_1)\right] = \cosh\theta_1 \sinh\theta_2 e^{i(\phi_2-\phi_1)} - \sinh\theta_1 \cosh\theta_2. \tag{2.54b}$$

In the limit of a perfect interface, *i.e.*, $r = 0$, the above equations reduce to the continuity equations for θ and ϕ: $\theta_1 = \theta_2$ and $\phi_1 = \phi_2$. In the absence of a supercurrent, *i.e.*, $\partial_x \phi_{1(2)} = 0$, one can also get a relatively simple boundary condition: $r(\partial_x\theta_1) = \sinh(\theta_2 - \theta_1)$ and $\phi_1 = \phi_2$.

2.1.7.2. Boundary conditions for kinetic equations

In ideal reservoirs, no matter whether one has a normal reservoir or a superconducting reservoir, the boundary conditions for the distribution functions h_L and h_T are (at specific temperature T and voltage V)

$$h_{L(T)} = \frac{1}{2}\left[\tanh\frac{E+eV}{2T} \pm \tanh\frac{E-eV}{2T}\right]. \tag{2.55}$$

Note that, in case of $V = 0$, $h_L = \tanh\frac{E}{2T}$ and $h_T = 0$. Moreover, $h_L = \tanh\frac{E}{2T} = 1-2f_0$, where $f_0 = 1/(e^{E/T}+1)$ is the usual equilibrium Fermi distribution function. In another words, h_L and h_T are directly related to the Fermi distribution function, but in a different representation.

2.1.8. Physical quantities

In the dirty limit approximation, applying the parameterizaion (Eqn. (2.30) and (2.31)) to the equations of physical quantities (Eqn. (2.16)), one can be rewritten Eqn. (2.16) as the following

(1) DOS of electrons:

$$N(E) = N_0 \cosh\left(\Re(\theta)\right)\cos\left(\Im(\theta)\right). \tag{2.56}$$

(2) electrical current:

$$\begin{aligned} j &= \frac{eN_0D}{4}\int_{-\infty}^{\infty} dE\ \mathrm{Tr}\left[\hat{\tau}_3(\hat{g}^R\partial\hat{g}^K + \hat{g}^K\partial\hat{g}^A)\right] \\ &= eN_0D\int_{-\infty}^{\infty} dE\ (Q\cdot h_L + M_{03}\cdot\partial h_L + M_{33}\cdot\partial h_T) \\ &= j_s + j_t + j_n, \end{aligned} \tag{2.57}$$

where $j_n = eN_0D\int_{-\infty}^{\infty} dE\ (M_{33}\cdot\partial h_T)$ corresponds to the normal current, $j_s = eN_0D\int_{-\infty}^{\infty} dE\ (Q\cdot h_L)$ the supercurrent, and $j_t = eN_0D\int_{-\infty}^{\infty} dE\ (M_{03}\cdot\partial h_L)$ is the current related to broken particle-hole symmetry.

(3) thermal current:

$$\begin{aligned} j^T &= N_0D\int_{-\infty}^{\infty} dE\ E(Q\cdot h_T + M_{30}\cdot\partial h_T + M_{00}\cdot\partial h_L) \\ &= j_s^T + j_t^T + j_n^T. \end{aligned} \tag{2.58}$$

(4) superconducting gap:

$$\begin{aligned} \Delta &= N_0\frac{\lambda}{4}\int dE\ [\hat{g}_s^R\hat{h} - \hat{h}\hat{g}_s^A]_{12}, \\ &= N_0\frac{\lambda}{4}\int dE\ \left[h_L(\text{sinh}\theta e^{i\phi} + \text{sinh}\theta^* e^{i\phi^*}) - h_T(\text{sinh}\theta e^{i\phi} - \text{sinh}\theta^* e^{i\phi^*})\right]. \end{aligned} \tag{2.59}$$

This equation is usually used for the self-consistent calculation of the superconducting gap. In an ideal superconducting reservoir with $V = 0$ and $\phi = 0$, the above equation can be simplified to

$$\Delta = N_0\lambda\int_0^{\infty} dE\ \tanh(E/2k_BT)\Re\left(\frac{\Delta}{\sqrt{E^2-\Delta^2}}\right). \tag{2.60}$$

2.2. Applications of quasiclassical theory to proximity-coupled systems

The quasiclassical theory of superconductivity has been used to improve our understanding of the transport properties of the proximity-coupled normal-metal systems in many publications. For example: [**54, 55, 56, 57, 58, 59**]. In the following part of this chapter, we are going to apply it to calculate the thermal conductance of such systems. Before we show the simulation details, let me first introduce the general routine we used to solve this type of problems.

2.2.1. Routine for numerical simulations

In general, in order to calculate the electrical and thermal properties of mesoscopic devices, one needs to solve the Usadel equation and the kinetic equations numerically. The routine is the following:

(1) Guess an appropriate initial distribution of the superconducting gap in the sample.

(2) Solve the Usadel equation (2.35) numerically for θ and ϕ with proper boundary conditions.

(3) Use the values of θ and ϕ from the previous step to calculate Q and M_{ij}, and then solve the kinetic equations (2.46) for h_L and h_T with proper boundary conditions.

(4) Calculate the superconducting gap by using Eqn. (2.59) and compare it with the assumption used in step (1). If a self-consistent calculation is required, use the new calculated gap and go to step (2). Repeat step (2)-(4) until the calculated gap converges.

(5) Calculate the physical quantities of interest.

2.2.2. Proximity-coupled normal-metal wire

Consider a proximity-coupled normal-metal wire of length L with one end ($x = 0$) connected to a normal reservoir and another end ($x = L$) to a superconducting reservoir, as shown in Fig. 2.1. We set the normal reservoir at a higher temperature

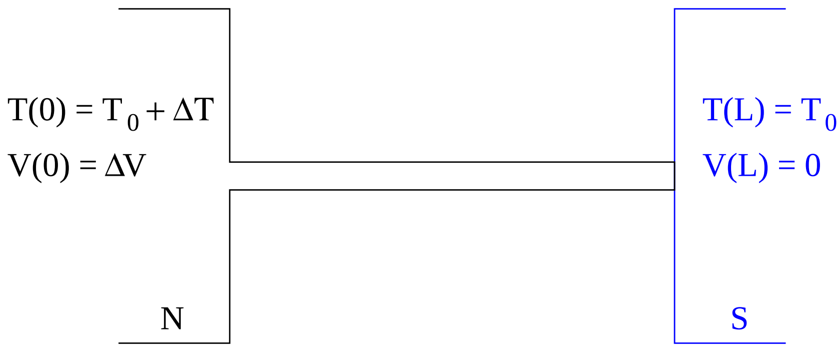

Figure 2.1. Schematic of a proximity-coupled normal-metal wire with one end ($x = 0$) connected to a normal reservoir and another end ($x = L$) to a superconducting reservoir.

$T(0) = T_0 + \Delta T$ and voltage $V(0) = \Delta V$, while the superconducting reservoir is at a lower temperature $T(L) = T_0$ and voltage $V(L) = 0$.

This sample configuration is relatively simple. There is no supercurrent flowing in the normal-metal wire, so $\partial\phi = 0$. In addition, we can set $\phi = 0$ in the superconducting reservoir, which results in $\phi(x) = 0$ for $x \in [0, L]$. Solving the Usadel equation (2.35) for θ and ϕ and inserting the results into Eqn. (2.56), one can obtain the DOS of quasiparticles along the wire. Figure 2.2 shows the normalized DOS, $N(x, E)/N_0$, as a function of position and particle energy along the wire. It needs to be pointed out that: (1) At $x = 0$, $N(0, E)/N_0 = 1$, as one expected for a normal reservoir. (2) At $x = L$, due to the presence of the superconducting gap, the DOS shows a divergence at the gap energy, and reduces to zero when $E \to 0$. However, unlike a bulk superconductor, the DOS is not strictly equal to zero for $E < \Delta$, but shows a finite value. This reduction of DOS is also called a "pseudogap", as analogous to the *real* superconducting gap Δ. (3) When $x \in (0, L)$, both the pseudogap and the divergence at the gap energy are reduced as one moves away from the superconducting reservoir.

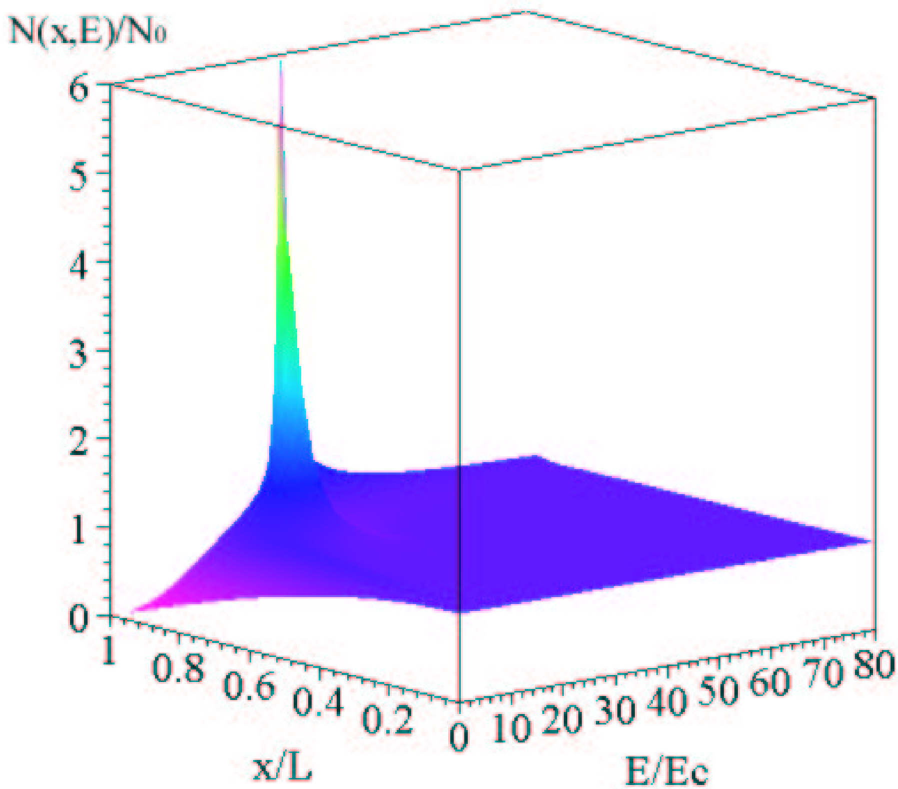

Figure 2.2. Normalized DOS, $N(x, E)/N_0$, in a proximity-coupled normal-metal wire as a function of position x and particle energy E. x is normalized to L, the length of the wire, while energy E is normalized to $E_c = D/L^2$, the so-called correlation energy or Thouless energy. We use our experimental value: $\Delta = 30.3E_c$ in this simulation.

In addition, the above position dependence of DOS has been observed in experiments [**60**].

The kinetic equations for this sample configuration can be solved analytically because of the fact that $Q = 0$, $M_{03} = 0$ and $M_{30} = 0$ simplifies the problem. In specific, the kinetic equations (2.46) can be simplified to

$$\begin{aligned} M_{33} \cdot \partial h_T &= I(E) = \text{constant}, \\ M_{00} \cdot \partial h_L &= I^T(E) = \text{constant}. \end{aligned} \tag{2.61}$$

One can do the integration over x and rewrite the above equations as

$$\begin{aligned} I(E) &= D_3 \left[h_T(L) - h_T(0) \right], \\ I^T(E) &= D_0 \left[h_L(L) - h_L(0) \right], \end{aligned} \tag{2.62}$$

where

$$\begin{aligned} D_0^{-1} &\equiv \int_0^L \frac{dx}{M_{00}} = \int_0^L \frac{dx}{\cos^2(\Im(\theta))}, \\ D_3^{-1} &\equiv \int_0^L \frac{dx}{M_{33}} = \int_0^L \frac{dx}{\cosh^2(\Re(\theta))}. \end{aligned} \tag{2.63}$$

The boundary conditions, Eqn. (2.55), read

$$\begin{aligned} h_L(0) &= \frac{1}{2} \left[\tanh \frac{E + e\Delta V}{2(T_0 + \Delta T)} + \tanh \frac{E - e\Delta V}{2(T_0 + \Delta T)} \right], \\ h_L(L) &= \tanh \frac{E}{2T_0}, \\ h_T(0) &= \frac{1}{2} \left[\tanh \frac{E + e\Delta V}{2(T_0 + \Delta T)} - \tanh \frac{E - e\Delta V}{2(T_0 + \Delta T)} \right], \\ h_T(L) &= 0. \end{aligned} \tag{2.64}$$

For a small voltage differential ΔV and temperature differential ΔT across the normal-metal wire, in the linear response regime, the right hand side of Eqn. (2.64) can be expanded into Taylor's series. Therefore, Eqn. (2.62) can be expressed in terms of ΔV and ΔT as

$$\begin{aligned} I(E) &= \frac{eD_3}{2T_0 \cosh^2 \frac{E}{2T_0}} \Delta V, \\ I^T(E) &= -\frac{ED_0}{2T_0^2 \cosh^2 \frac{E}{2T_0}} \Delta T. \end{aligned} \tag{2.65}$$

In conventional Boltzmann transport theory, the electrical current and the thermal current can be formulated in a linearized form [**12**],

$$\begin{aligned} I &= G\Delta V + \eta(-\Delta T), \\ I^T &= \zeta \Delta V + \kappa(-\Delta T), \end{aligned} \tag{2.66}$$

where G is the electric conductance, which is defined as $G \equiv I/\Delta V$ under the condition that $\Delta T = 0$. The thermal conductance is then defined by $G^T \equiv -I^T/\Delta T = \kappa - \zeta\eta/G$ under the condition that the total current through the sample vanishes $I = 0$. Since the second term in G^T is usually very small for a typical metal, $G^T \approx \kappa$.

Combining the above two sets of equations, one can get the electric conductance G and the thermal conductance G^T immediately,

$$\begin{aligned} G &= \frac{e^2 N_0 D}{2T_0} \int dE \frac{D_3}{\cosh^2 \frac{E}{2T_0}}, \\ G^T \approx \kappa &= \frac{N_0 D}{2T_0^2} \int dE \frac{E^2 D_0}{\cosh^2 \frac{E}{2T_0}}. \end{aligned} \tag{2.67}$$

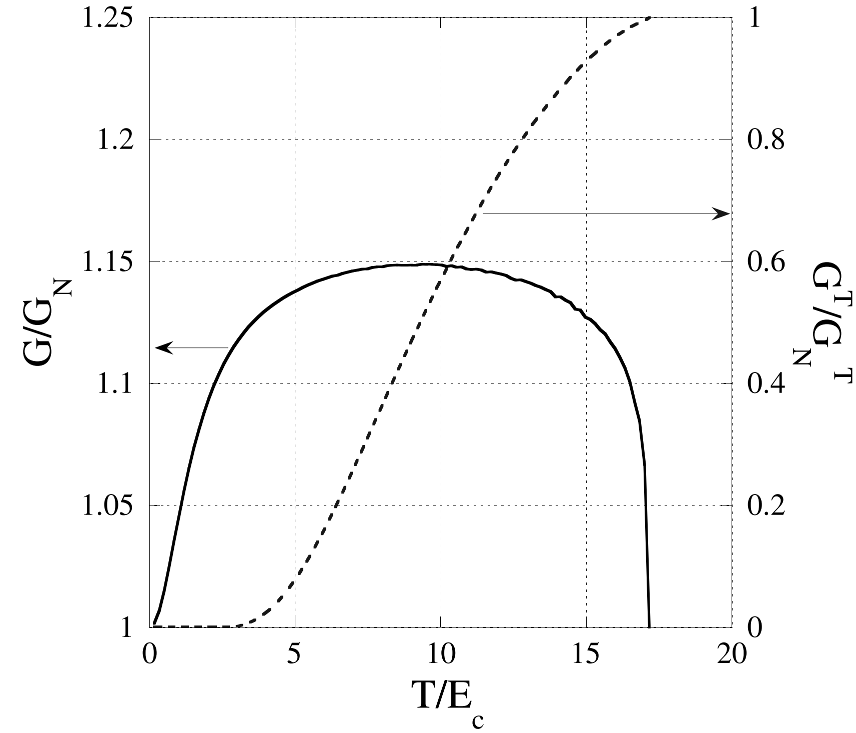

Figure 2.3. Normalized electric conductance (solid line) and thermal conductance (dashed line) of the proximity-coupled normal-metal wire as a function of temperature. Again, we use our experimental value: $\Delta = 30.3E_c$, *i.e.*, $T_c = 17.2E_c$.

Figure 2.3 shows the normalized electric conductance G/G_N (solid line) and thermal conductance G^T/G_N^T (dashed line) of the proximity-coupled normal-metal wire as a function of temperature, where G_N and G_N^T are the normal state electric and thermal conductance respectively. In Fig. 2.3, G/G_N shows non-monotonic temperature dependence at $T < T_c$: as the temperature drops down below T_c, G/G_N first increases and then decreases, approaching its normal state value $G/G_N = 1$ as $T \to 0$. G/G_N reaches its maximum at a temperature of $T \approx 9Ec/k_B$[3]. This is the

[3]In general, one would expect the maximum in G/G_N to be around $T \approx 5Ec/k_B$ [**48**]. However, since we have taken into account of the temperature dependence of the superconducting gap in our calculations, the maximum in conductance occurs at a higher temperature, $\approx 9Ec/k_B$.

well-known proximity effect and reentrance behavior, which has been studied both experimentally [**61, 62, 63**] and theoretically [**56, 57, 58, 64, 65**]. This non-monotonic temperature dependence is a result of the competition between two effects. One is the penetration of superconducting correlations from the superconducting reservoir into the normal-metal wire, which increases the value of G; another effect is the reduction of the DOS of quasiparticles (pseudogap) at very low temperatures, which reduces the value of G. The reduction in G^T/G_N^T, however, is monotonic as a function of temperature. It stems only from the reduction of the DOS of quasiparticles, since the induced superconducting correlations in the normal-metal wire would not carry any thermal current. Hence, the Wiedemann-Franz law [**11**] breaks down in such system. Moreover, as noted by Andreev [**10**], for a NS interface, G^T/G_N^T vanishes at a temperature well below T_c.

If we replace the superconducting reservoir in Fig. 2.1 with another normal reservoir, the entire device becomes a normal-metal system. Consequently, the solutions of the Usadel equation (2.35) change to the simplest form: $\theta(x) = 0$ and $\phi(x) = 0$ for $x \in [0, L]$. Consequently, $D_0 = 1$ and $D_3 = 1$, and Eqn. (2.67) reduces to

$$\begin{aligned} G &= 2e^2 N_0 D = \text{constant}, \\ G^T &= \frac{2\pi^2 N_0 DT}{3} = \pounds_0 G T, \end{aligned} \tag{2.68}$$

where $\pounds_0 = \pi^2/3e^2$ is the Lorenz number. This is exactly the Wiedemann-Franz law, but re-discovered in the language of the quasiclassical theory of superconductivity.

2.2.3. Thermal conductance of Andreev interferometers

In this section, we calculate the thermal conductance G^T of diffusive Andreev interferometers with two different geometries relevant to our experiments. The calculation shows that the presence of the superconductor suppresses G^T. However, unlike the proximity-coupled normal-metal wire discussed in the previous section, G^T/G^T_N does not vanish at a temperature well below T_c, but saturates at a finite value that depends on the barrier resistance r of the NS interfaces and their distance from the path of the temperature gradient. It also has been shown that the reduction of G^T results from the suppression of the DOS in the proximity-coupled normal metal along the path of the temperature gradient. In addition, we find that G^T/G^T_N is non-linear, varying with the thermal current I^T approximately as $\sqrt{I^T}$ for intermediate values of I^T. Finally, G^T oscillates periodically as a function of the applied magnetic flux, with a fundamental period of one flux quantum $\Phi_0 = h/2e$. As with the electric conductance, the thermal conductance oscillations are symmetric with respect to the applied magnetic flux.

Figure 2.4 illustrates the two types of Andreev interferometers calculated in this section. Following the terminology used in Ref. [**17**], we call them: (a) the "house" geometry and (b) the "parallelogram" geometry. Our intent here is to determine the effect of sample geometry and finite NS interface resistance on G^T.

The thermal conductance of such Andreev interferometers can only be calculated numerically. Again, we are going to follow the simulation routine introduced previously and start with the assumption that there is no superconducting gap in the proximity-coupled normal metal, $\Delta = 0$. Therefore, the Usadel equation can be written in the form of Eqn. (2.35). However, to close the set of equations, we must

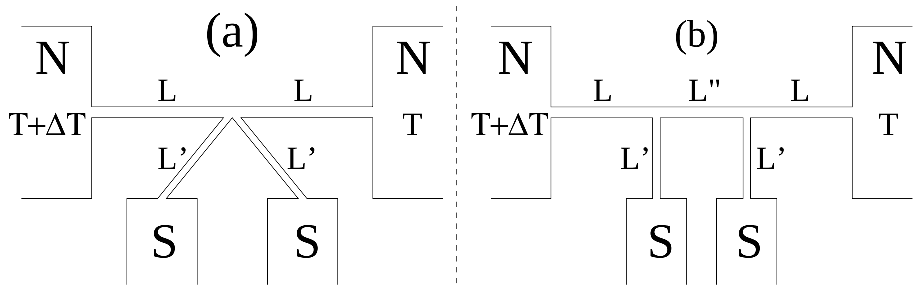

Figure 2.4. Schematic of Andreev interferometers with two different geometries: (a) “house” and (b) “parallelogram”.

specify the boundary conditions for θ and ϕ at the NS interfaces and at the nodes where multiple one-dimensional normal-metal segments meet. At the NS interfaces, in the limit of low transparency, the boundary conditions can be expressed as Eqn. (2.54). In case of perfect interfaces, $r = 0$, these boundary conditions reduce to the continuity equations of the θ function and the phase ϕ across the interface, *i.e.*, θ and ϕ obey the reservoir boundary conditions Eqn. (2.50). In addition, the major contribution to the phase ϕ is from the applied magnetic flux. Since the critical current in the superconducting loop is much larger than that in the proximity-coupled normal metal, we could assume that all the phase drop occurs across the normal-metal wires between two NS interfaces. In the following simulation, we will apply the phase change $\Delta\phi$ symmetrically between the two NS interfaces. For example, for an applied flux of $\Phi_0/2$ (*i.e.*, $\Delta\phi = \pi$) through the area of the Andreev interferometer loop, we set the phases ϕ at the two NS interfaces to be $-\pi/2$ and $\pi/2$ respectively. For a normal reservoir, the absolute value of ϕ is meaningless, but the gradient $\partial_x\phi$ must be 0 to assure no supercurrent in it. For a node, assuming one-dimensional wires of equal cross-section, the boundary conditions reduce to the condition that the parameter θ

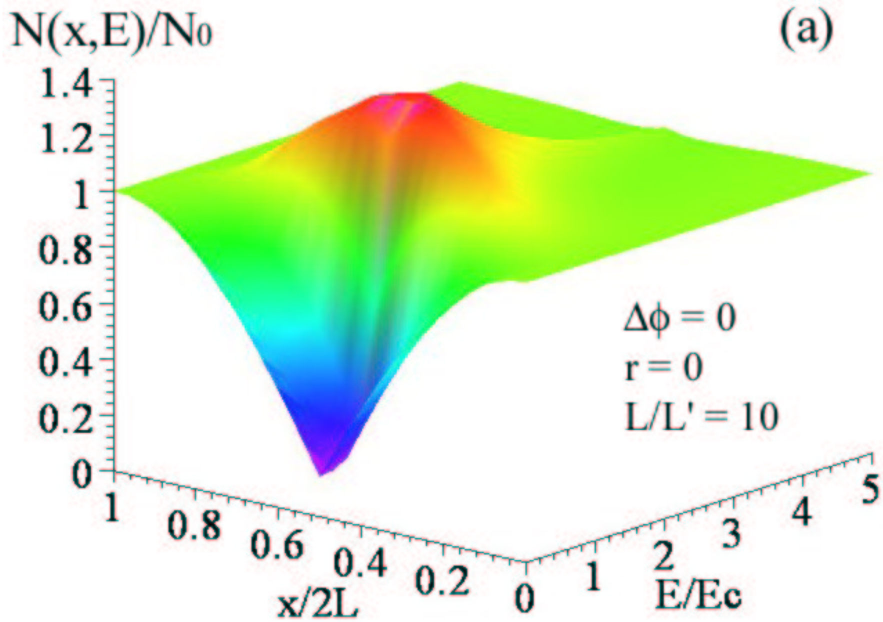

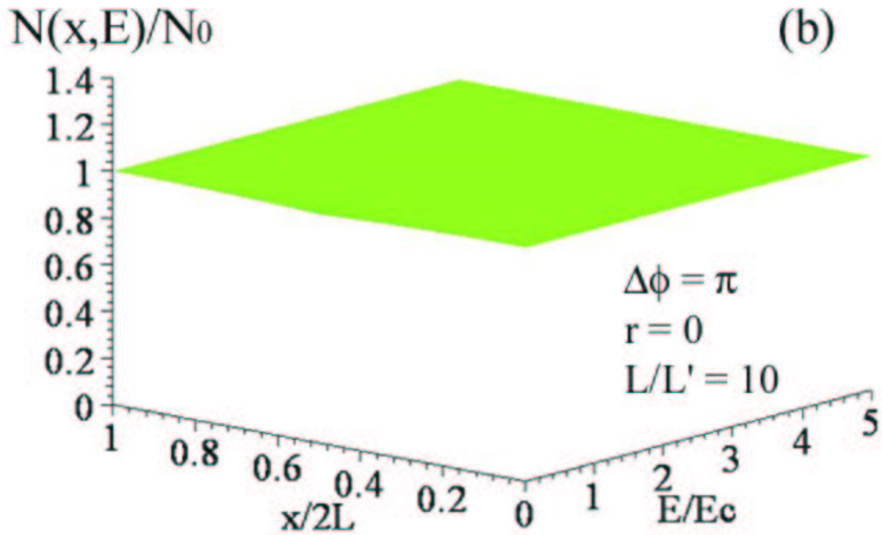

Figure 2.5. Normalized DOS $N(x, E)/N_0$ for the "house" interferometer along the path of the temperature gradient for $r = 0$ and $L/L' = 10$. (a) $\Delta\phi = 0$; (b) $\Delta\phi = \pi$.

and ϕ must be continuous at the node, and $\sum \partial_x \theta = 0$, $\sum \partial_x \phi = 0$, where the sum is over all wires emanating from the node.

After all the efforts above, we should be able to solve the Usadel equation (2.35) and calculate the DOS of quasiparticles in these devices. Figure 2.5(a) illustrates the normalized DOS, $N(x, E)/N_0 = \cosh(\Re(\theta)) \cos(\Im(\theta))$, for the "house" interferometer along the path of the temperature gradient from $x = 0$ to $x = 2L$, for $\Delta\phi = 0$, $r = 0$ and $L/L' = 10$. It shows that the maximum suppression is reached at the node ($x = L$). However, unlike a conventional superconductor [**66**], $N(x, E)/N_0$ does not vanish at $E < \Delta$, which is consistent with Fig. 2.7(a) and (b) that G^T/G^T_N is suppressed, but remains finite as $T \to 0$. For the "parallelogram" interferometer, as shown in Fig. 2.6(a), an even larger suppression has been observed in $N(x, E)/N_0$ due to the presence of the middle segment. Note that the DOS can be tuned by the applied magnetic flux Φ for both geometries. While $\Delta\phi = \pi$ (shown in Fig. 2.5(b) and Fig. 2.6(b)), the suppression in $N(x, E)/N_0$ of the "house" interferometer has been removed completely and it is strongly reduced for the "parallelogram" interferometer as well.

The next step is to calculate Q and M_{ij} by using the values of θ and ϕ obtained from the solutions of the above Usadel equation. We then solve the kinetic equations (2.46) for the non-equilibrium distribution functions, h_L and h_T[4]. Finally, we calculate the electric and thermal conductance of Andreev interferometers.

In general, to determine the thermal current through an Andreev interferometer, one must consider the supercurrent flowing between the two NS interfaces in the presence of a magnetic field, although the terms involving the supercurrent make the

[4]In the normal and superconducting reservoirs, the boundary conditions of h_L and h_T are expressed by Eqn. (2.55).

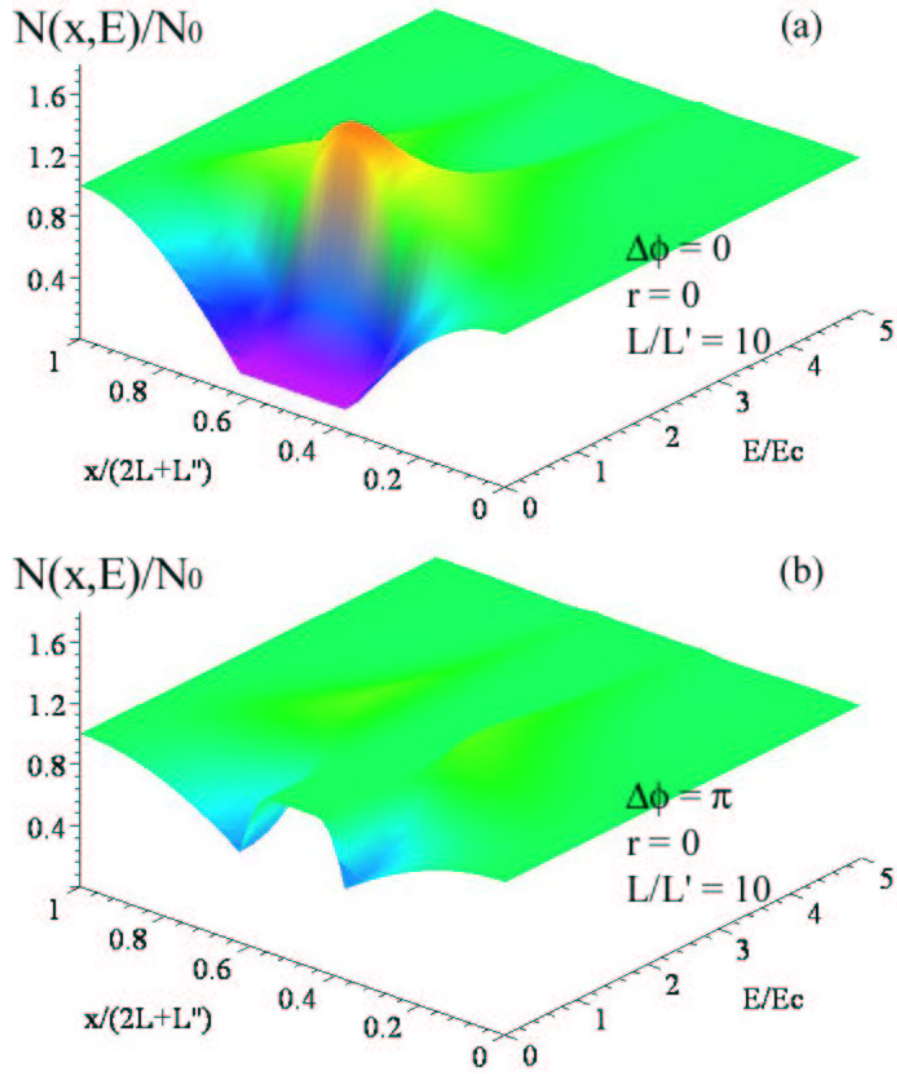

Figure 2.6. Normalized DOS $N(x, E)/N_0$ for the "parallelogram" interferometer along the path of the temperature gradient for $r = 0$, $L/L' = 10$ and $L''/L = 0.66$. (a) $\Delta\phi = 0$; (b) $\Delta\phi = \pi$.

kinetic equations much more difficult to solve. However, for the geometries shown in Fig. 2.4, some simplifications can be made. For the "house" geometry, as shown in Fig. 2.4(a), a temperature differential ΔT has been established across the two normal reservoirs, *i.e.*, the right normal reservoir is at a temperature of T and the left reservoir is at a temperature of $T+\Delta T$. Since there is no supercurrent flowing in the segments connected to the two normal reservoirs, the phase ϕ in these segments is a constant, $\partial_x \phi = 0$. Furthermore, applying the boundary conditions for the phase ϕ as discussed above, we get $\phi = 0$ at the central node by symmetry. It should be pointed out that $\phi = 0$ at the central node is also confirmed by the results of numerical solutions after we solve the Usadel equation. Hence, we can take $\phi = 0$ in the segments connected to the two normal reservoirs and calculate Q and M_{ij} accordingly, which turn out to be $Q = 0$ and $M_{03} = M_{30} = 0$. Following the derivation performed in the previous section for the proximity-coupled normal-metal wire, one can write down the thermal conductance of the "house" Andreev interferometer as

$$G^T = \frac{N_0 D}{2T^2} \int dE \frac{E^2}{\cosh^2(E/2T)} \left[\int_0^{2L} \frac{1}{M_{00}} dx \right]^{-1}. \tag{2.69}$$

Figure 2.7(a) shows the normalized thermal conductance G^T/G^T_N of the "house" interferometer as a function of the normalized temperature T/T_c, for a sample with perfectly transparent NS interfaces ($r = 0$). The length L of one normal-metal segment attached to a normal reservoir defines the correlation energy $E_c = \hbar D/L^2$ (see Fig. 2.4). As in the previous section, we choose $\Delta = 30.3E_c$, *i.e.*, $T_c = 17.2E_c$, related closely to the values in our experiments. The different curves in Fig. 2.7(a) correspond to different lengths L' of the normal-metal segments from the central node to the superconducting reservoirs. Notice that G^T differs appreciably from its normal

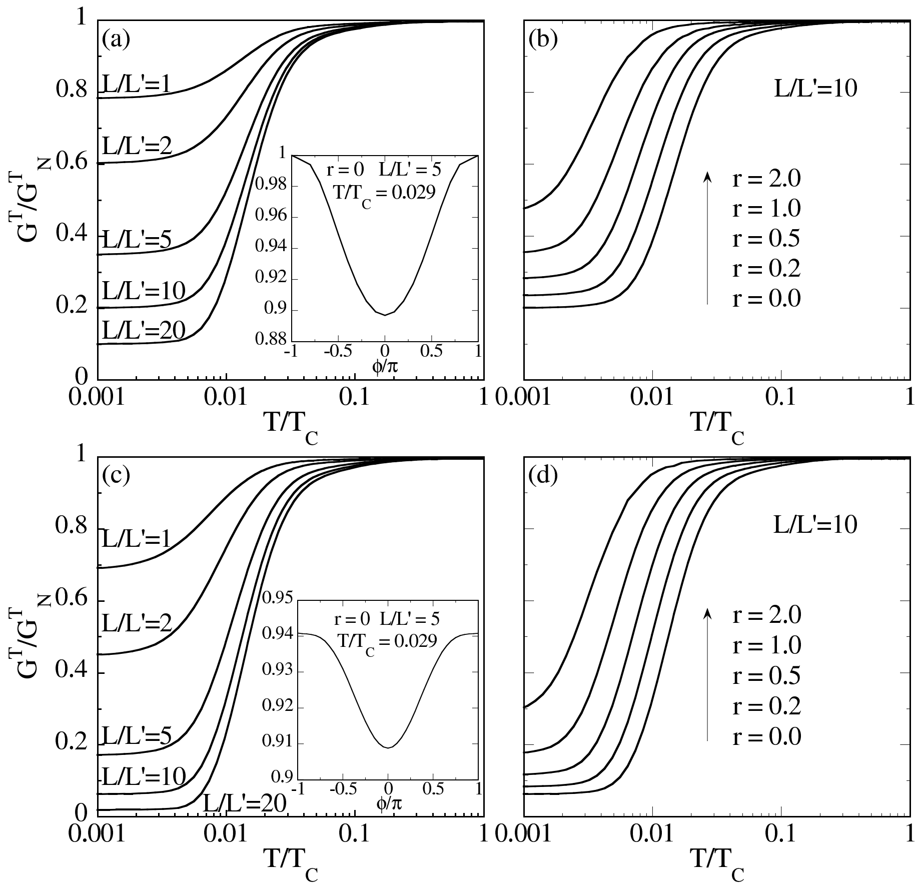

Figure 2.7. Normalized thermal conductance G^T/G_N^T of the "house" interferometer ((a) and (b)) and the "parallelogram" interferometer ((c) and (d)) as a function of the normalized temperature T/T_c. (a) and (c): for different L/L'; (b) and (d): for different r. The insets in (a) and (c) show the oscillations of G_T/G_N^T as a function of the phase ϕ.

state value G_N^T only at temperatures below E_c/k_B, and G^T/G_N^T saturates as $T \to 0$. The overall decrease in G^T/G_N^T depends on L'. As expected, the smaller L', the larger proximity effect and the larger decrease in G^T/G_N^T.

The normalized thermal conductance G^T/G_N^T of the "house" interferometer decreases monotonically as one decreases the temperature below T_c. This decrease is directly associated with the suppression of the DOS along the path of the temperature gradient. On the other hand, the electric conductance G of such devices behaves non-monotonically as a function of the temperature, showing the well-known reentrance effect. Hence, as indicated in both Fig. 2.5 and 2.7, the Wiedemann-Franz law is violated for such devices.

Any parameter that affects $N(x, E)$ will modify G^T. As shown in Fig. 2.7(a), the distance L' from the superconducting reservoir to the central node is one of such parameters. A second parameter is the NS interface resistance r. A larger value of r, *i.e.*, a lower transparency of the interface, would reduce the proximity effect in the normal metal, leading to a smaller suppression in G^T. This picture is supported by Fig. 2.7(b), where G^T/G_N^T as a function of T/T_c for $L/L' = 10$ has been plotted for a number of different values of r. The greatest suppression in G^T appears when $r = 0$. Since both L' and r affect G^T, understanding the dependence of G^T on L' and r is crucial for a quantitative analysis of the experimental results. Moreover, the simulations suggest that, in order to observe the largest suppression in G^T, it is important to improve the alignment ability (to reduce L') and the interface transparency during the sample fabrication process.

The third parameter that affects $N(x, E)$ is the applied magnetic flux. Figure 2.5(a) shows the normalized DOS, $N(x, E)/N_0$, for zero phase difference ($\Delta\phi = 0$)

between the two superconducting reservoirs; Fig. 2.5(b) shows $N(x,E)/N_0$ for $\Delta\phi = \pi$, corresponding to half flux quantum $\Phi_0/2$ through the interferometer loop. For $\Delta\phi = \pi$, $N(x,E)/N_0$ is essentially constant between the two normal reservoirs at a value corresponding to the normal state DOS, $N(x,E)/N_0 = 1$. Consequently, G^T regains its normal state value G_N^T at $\Delta\phi = \pi$, so that G^T shows full scale oscillations as a function of magnetic flux. This can be seen in the inset of Fig. 2.7(a), which shows G^T as a function of ϕ for $r = 0$ and $L/L' = 5$ at a temperature of $T/T_c = 0.029$. The observation of full-scale oscillations is directly related to the symmetry of the "house" interferometer. Further simulations show that if the distance from the central node to one of the superconducting reservoir was not exactly same as the corresponding length in the other side one, or the two NS interfaces had different barrier resistances, there would still be a suppression of DOS at the central node even for $\Delta\phi = \pi$. Hence, we would not be able to obtain full scale oscillations.

We now turn to discuss the results of the "parallelogram" interferometer. Basically, as shown in Fig. 2.7, the major results of the "parallelogram" interferometer are similar to the "house" configuration. Therefore, in the following discussion, we will mostly focus on the differences between them. For a "parallelogram" interferometer (shown in Fig. 2.4(b)), in addition to the two normal-metal segments of length L connected to the normal reservoirs, we also have a normal-metal segment of length L'' in the path of the temperature gradient. In the later calculations, we will use a typical experimental value of $L''/L = 0.66$, and keep all other parameters same as those used for the "house" interferometer. Since this additional segment lies between the two superconducting reservoirs, when magnetic flux is applied to such a system, a supercurrent would flow in this segment. Therefore, the first two terms in Eqn. (2.58) cannot be ignored any more as with the "house" configuration, and the kinetic equations would have a relatively complex form. However, since V in the superconducting reservoirs is set to zero, $h_T = 0$ at the superconducting reservoirs, so that the terms involving h_T are small, and can be ignored. It is important to point out that this assumption is very reasonable, because it is actually supported by detailed numerical simulations [**22**], where the solutions of the kinetic equations with and without this assumption are quite close. Consequently, we can continue to use Eqn. (2.69) to calculate G^T, except that the integral of $1/M_{00}$ is over the three normal-metal segments along which the thermal current flows.

G^T/G^T_N *vs.* T/T_c for the "parallelogram" interferometer has been shown in Fig. 2.7(c) and (d) for different values of L/L' and r. Compared with the "house" interferometer, a deeper suppression of G^T has been observed, which is associated with the broad suppression of DOS in the middle segment of the "parallelogram" interferometer (as shown in Fig. 2.6). Moreover, we also find that, as in the "house" interferometer, G^T of the "parallelogram" interferometer oscillates periodically as a function of the applied magnetic flux. As shown in the inset of Fig. 2.7(c)), the oscillations are symmetric with respect to the phase ϕ. However, unlike the "house" interferometer, G^T never reaches its normal state value G^T_N even at $\Delta\phi = \pi$, because, as shown in Fig. 2.6(b), there would always be a finite suppression in DOS around the two nodes of the "parallelogram" interferometer.

We should also note that the above simulations are in the linear response regime, because we have taken the linear response limit of Eqn. (2.62) to calculate G^T. However, in our experiments on the thermal conductance of Andreev interferometers, we find that G^T is actually a strongly non-linear function of the thermal current I^T

through the sample [**13, 15**]. In order to investigate this non-linear dependence of G^T on I^T, we numerically calculate the right side of Eqn. (2.62) for specific values of ΔT across the interferometer. In this calculation, G^T is still defined by the ratio $I^T/\Delta T$, but it is no longer given by the linear response result of Eqn. (2.69). As shown in Fig. 2.8, the calculated G^T is non-linear as a function of I^T for both the "house" and the "parallelogram" interferometers, since if G^T were linear for small I^T, we would expect a curve which had zero slope at $I^T = 0$, which is clearly not seen in the figure. In addition, at intermediate values of the thermal current, G^T varies as $\sqrt{I^T}$, shown by the dashed lines in the figure. Based on Fig. 2.8, we can estimate that the deviations from the $\sqrt{I^T}$ behavior are seen at $I^T < 4.3 \times 10^{-2}\ G_N^T E_c$ and the linear response regime is approached for values of I^T less than $4.3 \times 10^{-4}\ G_N^T E_c$. A similar dependence of G^T is also observed in the experiments, and we will discuss it further in Chapter 4.

Before we close the discussion of the thermal conductance of Andreev interferometers, we should not forget to mention the work by Bezuglyi and Vinokur (BV) [**14**], in which they calculated the thermal conductance G^T of a NSN sandwich-like structure and the thermal conductance oscillations in a "house"-like Andreev interferometer. The schematic of the studied systems has been shown in Fig. 2.9, adapted from Ref. [**14**]. But before we move onto the main results of BV's work, we would like to clarify that the devices BV studied are significantly different from ours. In BV's model, there always is a superconductor in the path of the thermal current. External parameters, which can modify the magnitude of the superconducting gap, will potentially affect G^T. In another words, the calculated G^T in BV's work is completely dominated by the superconducting portion of the device along the thermal

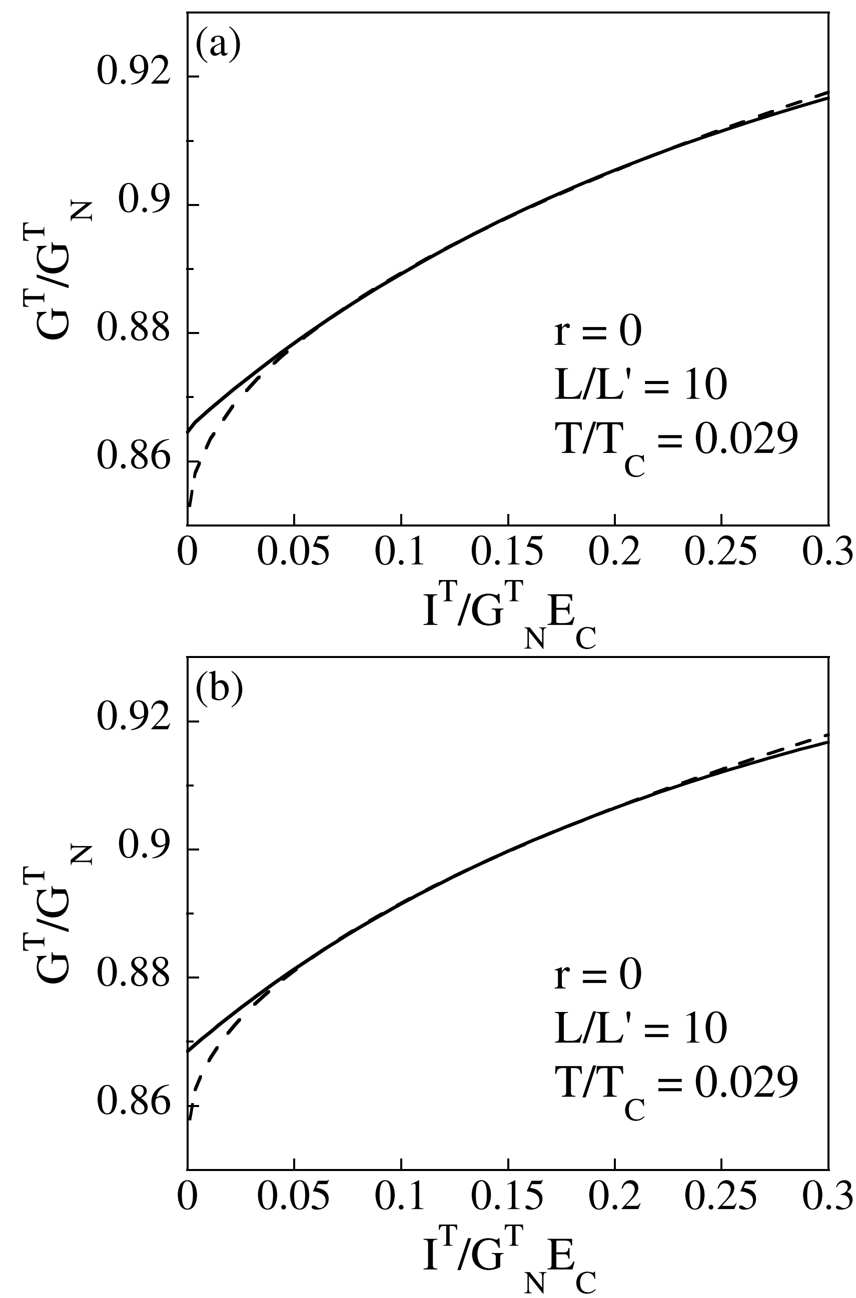

Figure 2.8. Solid lines represent the strongly non-linear G^T as a function of the thermal current I^T for both (a) the "house" and (b) the "parallelogram" interferometers. Dashed lines illustrate the $\sqrt{I^T}$ dependence of G^T at intermediate values of I^T.

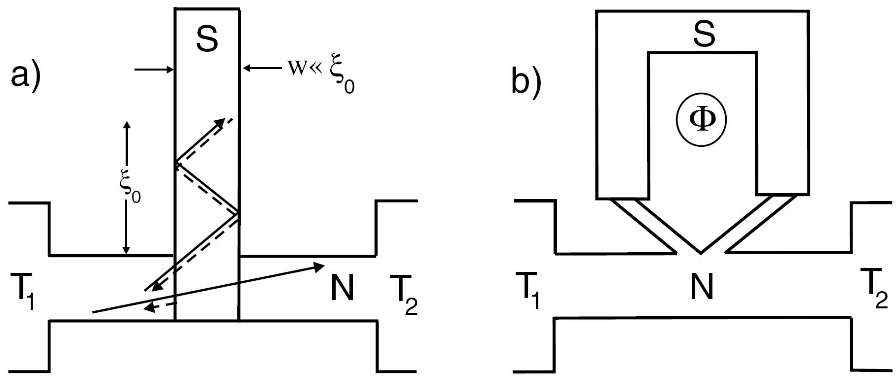

Figure 2.9. Schematic of the devices discussed by Bezuglyi and Vinokur. (a) A normal diffusive wire coupled with a superconducting wire in the limit of $w \ll \xi_0$, *i.e.*, the width of the superconducting wire is much less than the coherence length of the superconductor; (b) A "house" interferometer in the short SNS junction limit, *i.e.*, the length of the normal-metal wires between the two NS interfaces is much less than the coherence length. (Adapted from Ref. [**14**])

path. In contrast, in our devices as shown in Fig. 2.4, the two superconducting reservoirs are away from the path of the thermal current. The superconductivity effect can only penetrate into the normal-metal wires, but not open a real gap to intercept the thermal current. Hence, we calculate G^T in the true proximity regime.

The first geometry BV studied is a NSN sandwich-like structure. As shown in Fig. 2.9(a), it is essentially two diffusive normal wires coupled with a superconducting wire over a region much smaller than the coherence length of the superconductor[5], $w \ll \xi_0$. The thermal conductance G^T of this geometry is analyzed as a function of a parameter r that measures the relative amplitude of the proximity effect. Since the narrow superconducting wire is sandwiched between the two normal-metal wires along which the thermal current flows, G^T rapidly decreases with temperature due to the reduced thermal conductance of the superconductor. In contrast to our calculation,

[5]In our devices, $\xi_0 \approx 100$ nm for Al, and w is typically 50-100 nm. w is comparable to ξ_0.

their analysis shows that for a strong proximity effect (in the limit of $r \gg 1$), the thermal conductance approaches its normal state conductance. For $r \ll 1$, where the spectrum in the superconductor is not affected, there is a strong suppression of the thermal conductance. This is the so-called inverse proximity effect: as the coupling to the normal metal becomes stronger, the thermal conductance of the superconducting part increases. At very low temperatures, the Usadel equation has analytic solutions, the normalized thermal conductance obeys a powerlaw-like temperature dependence $G^T/G^T_N \propto T^4$.

In terms of the magnetic field dependence of the thermal conductance, BV calculate it for a "house" type Andreev interferometer, but in the short SNS junction limit, *i.e.*, the length of the normal-metal wires between the two superconducting reservoirs is much less than the coherence length. Moreover, they assume that the normal state conductance of the superconducting loop to be much larger than the conductance of the normal-metal wires, so that the presence of the normal-metal wires would not change the quasiparticle spectrum significantly in the junction. In this limit, one can apply a phase dependent superconducting gap $E_g(\phi) = \Delta|\cos(\phi/2)|$ at the central node where all normal-metal segments meet, so that their model of a NSN sandwich-like device can again be applied, but now with a phase dependent gap in the superconductor. At $\phi = 0$, a full superconducting gap opens up and intercepts the heat flow; at $\phi = \pi$, $\Delta = 0$ and $G^T \rightarrow G^T_N$. Consequently, one sees a 100% modulation of the thermal conductance on varying the phase. However, in our simulation, where we do not make those simplifying assumptions, the phase modulates the thermal conductance by about 10%, which is more in line with the experimental observations. In addition, from an experimental point of view, we note that some of the simplifying assumptions in BV's calculations make quantitative comparison the experiments difficult.

2.2.4. Symmetry of thermopower oscillations in Andreev interferometers

As a temperature differential ΔT is established across a metallic sample and no electrical current is allowed to flow through it, an induced electrostatic potential differential ΔV will be set up across the sample. The thermopower S is defined as the ratio of the induced voltage differential to the applied temperature differential $S \equiv \Delta V/\Delta T$. For canonical metals, the thermopower is related to the energy-dependent conductivity $\sigma(\epsilon)$ by Mott's relation [**12**]

$$S = -\frac{\pi^2}{3}\frac{k_B^2 T}{e}\frac{\sigma'(\epsilon_F)}{\sigma(\epsilon_F)}, \tag{2.70}$$

where $\sigma(\epsilon_F)$ the dc conductivity evaluated at the Fermi energy ϵ_F and $\sigma'(\epsilon_F) = \frac{\partial}{\partial\epsilon}\sigma(\epsilon)|_{\epsilon=\epsilon_F}$. In the framework of Fermi liquid theory, the thermopower stems from breaking of electron-hole symmetry, and arises from the second term in the Sommerfeld expansion of the Fermi distribution function [**12**]. For a typical metal (such as pure gold), this term is governed by a pre-factor k_BT/ϵ_F and is usually very small (less than 1 μV/K at low temperatures).

Equation (2.70) indicates that a large thermopower might be expected in systems where the conductivity depends on the energy ϵ of the quasiparticles near ϵ_F. Superconductor is one of such systems and has been studied extensively since 1970s [**67, 68, 69, 70, 71, 72**]. Following Eqn. (2.66), $S = \eta/G$ under the condition that $I = 0$. The thermoelectric coefficient η_S of the superconductor was first calculated by Gal'perin *et al.* using a quasiclassical Boltzmann equation method [**69**], in which

$$\eta_S = \eta_N G(\Delta/k_B T), \tag{2.71}$$

where η_S (η_N) is the thermoelectric coefficient in the superconducting (normal) state and the function $G(x)$ is given by

$$G(x) = \frac{6}{\pi^2} \int_x^\infty \frac{y^2 dy}{\cosh^2(y/2)}. \tag{2.72}$$

In the high temperature limit ($k_B T \gg \Delta$), $G(x) \to 1$ and $\eta_S \to \eta_N$. At low temperatures ($k_B T \ll \Delta$), η_S decreases exponentially with decreasing the temperature. In a bulk superconductor, however, because $\Delta V = 0$ in a steady state, one cannot directly measure the thermoelectric voltage induced by the applied temperature gradient. On the other hand, one also cannot directly detect the total thermal current in the system, since the resulting thermal current of the quasiparticles is canceled by a counterflowing supercurrent. Hence, to obtain the thermoelectric coefficient η_S, one needs to separate the normal and superconducting components of the current. The thermoelectric response of the superconductor was first measured by Clarke and Freake by detecting the thermally induced supercurrent in a point-contact Josephson junction system with an applied temperature gradient [**67**]. More related experiments in SNS junctions were performed later by Kartsovnik *et al.* [**71**] and Ryazanov *et al.* [**72**].

The focus of the above early work was on the thermoelectric response of superconductors, rather than on proximity-coupled normal metals. Mott's relation (2.70) is predicted to no longer be valid in the proximity regime [**73, 74, 20**]. In Ref. [**73**], Claughton and Lambert (CL) numerically calculated the thermopower of specific NS device geometries by solving the Bogoluibov-de Gennes equations. Their simulations were performed in the clean limit and showing that the amplitude of the thermopower of a normal metal wire in proximity to a superconductor is of the order of

$$S \sim 0.01 N_{ch} \frac{\pi^2}{e} \frac{k_B^2 T}{E_F}, \tag{2.73}$$

where N_{ch} is the number of channels in the wire. Inserting the typical values for our devices, we estimate the amplitude of the thermopower as ~ 1 μV/K at a temperature of 0.5 K. In addition, CL's calculation also shows that, for an Andreev interferometer, the thermopower oscillates as a function of the phase difference $\Delta\phi$ between the two NS interfaces. Although both the electric conductance and the thermal conductance of an Andreev interferometer are always symmetric with respect to $\Delta\phi$, the symmetry of the thermopower depends on the topology of the sample. For samples with an axis of mirror symmetry with respect to the two NS interfaces, the thermopower is expected to be symmetric as a function of $\Delta\phi$. In a sample with no particular geometrical symmetry, the thermopower also has no unique symmetry with respect to $\Delta\phi$.

The thermopower of Andreev interferometers with different geometries has been measured recently[6] [**17, 18, 19**]. In these experiments, which include some of our own, the measured thermopower was found indeed much larger than the values estimated from Mott's relation. In addition, the thermopower oscillations have also been observed as a function of magnetic flux with a period corresponding to one flux

[6]Note that all these experiments are performed in diffusive metal systems in the dirty limit.

quantum $\Phi_0 = h/2e$, which again demonstrates the phase coherent nature of electrons in such devices.

Our group has been investigating the symmetry of the phase-coherent thermopower oscillations in Andreev interferometers for more than six years. We find that the symmetry of the oscillations can be either symmetric or anti-symmetric, depending on the geometry of the sample. For Andreev interferometers similar to the "parallelogram" configuration, we always observe anti-symmetric oscillations; while for the "house" type interferometers, we find that the thermopower oscillations are symmetric.

This symmetry issue is attracting interest from theorists. In the early work of Seviour *et al.* and Kogan *et al.*, they suggest that the thermopower of NS structures may arise from the branch imbalance under non-equilibrium conditions in the presence of a superconductor [**20, 21**], where the branch imbalance implies the difference between the electron-like and hole-like branches of the excitation spectrum. It also has been shown that the imbalance is a periodic function of the phase, resulting in a phase-coherent thermopower oscillations. In this picture, the supercurrent in the superconductor may not be equal to the supercurrent in the proximity-coupled normal-metal wires (the wires between the two superconducting reservoirs) in the presence of a magnetic field. This difference leads to conversion of the supercurrent to quasiparticle current. The quasiparticle current can carry a thermal current and results in the appearance of an electric potential V_{imb} in the loop of the Andreev interferometer. However, as we mentioned before, a superconductor is a poor thermal conductor at low temperatures. Thermal current is not allowed to circulate in the loop of the Andreev interferometer, which is mostly fabricated from superconductor.

Consequently, the thermal current would leak out from the nodes to the normal reservoirs and generate a finite thermal voltage V_{th} across the two normal reservoirs. It is obvious that V_{th} in the "parallelogram" interferometer is anti-symmetric with respect to the applied magnetic field, because the supercurrent is anti-symmetric in the middle segment of such devices. As for the "house" geometry, the thermal current can only flow out from the central node (point connection) of the interferometer. Hence, one would naturally expect a symmetric oscillation in V_{th}.

Extending our thermal conductance calculations above, we can also investigate the symmetry of thermopower oscillations qualitatively. From Eqn. (2.57), we know that the symmetry of the phase dependent thermopower oscillations is determined by the integrand, $(Q \cdot h_L + M_{03} \cdot \partial h_L + M_{33} \cdot \partial h_T)$, where the longitudinal (transverse) distribution functions, $h_L(h_T)$, are functions of ΔV and ΔT across the sample. Expansion of ∂h_T in the third term in the integrand gives a term that depends only on ΔV, but not on ΔT. Therefore, this term has no contribution to the off-diagonal or thermoelectric term, which relates the electrical current j through the sample to the temperature differential ΔT across the sample. This is in agreement with the well-known fact that the derivation of the quasiclassical approximation assumes particle-hole symmetry, and hence throws out from the beginning the usual small thermoelectric effects found in a typical metal. However, there are more terms in the integrand of Eqn. (2.57). The first two terms actually do have a component proportional to ΔT, and generate the thermoelectric effect. As shown in Eqn. (2.47) and (2.48), M_{33} is symmetric with respect to the applied magnetic flux, while Q and M_{03} are anti-symmetric. Although Q and M_{03} are usually small, in some cases such as in the well-known charge imbalance regime of superconductor, pronounced thermoelectric effects have been observed [**75, 76, 77**].

Recently, Virtanen and Heikkilä (VH) also examined the thermopower of Andreev interferometers by solving the Usadel equation (2.35) and the kinetic equations (2.46) numerically [**22**]. Their simulation indeed shows that the terms involving Q and M_{03} lead to a dominant thermoelectric contribution which is anti-symmetric as a function of the phase ϕ. According to VH, the contribution from Q is the zero order contribution, which is much larger than the one from M_{03} (first order contribution), indicating that the origin of the symmetry of the thermopower oscillations is more related to the supercurrent in the devices. In order to illustrate VH's results, let us consider the "parallelogram" interferometer. A typical Andreev interferometer is designed so that the Josephson coupling between the two NS interfaces of the interferometer is strong at low temperatures. Therefore, if one applies a magnetic field on such devices, a diamagnetic supercurrent will be generated and circulate in the interferometer loop. This supercurrent is anti-symmetric in the applied magnetic flux. Furthermore, if one also considers the applied temperature differential across the sample, one would expect a corresponding temperature gradient between the two NS interfaces. As we known, the supercurrent is very sensitive to the temperature. Hence, the supercurrent coming out of one NS junction will not be the same as the current going in to the second junction. In order to conserve the total current, the excess supercurrent must convert into quasiparticle current and go to the normal-metal side arms. Since the thermopower is measured under the condition that there is no electrical current through the sample, a thermoelectric voltage V_{th} must develop to cancel the contribution due to the excess current. V_{th} will be anti-symmetric with respect to the applied magnetic flux, as the supercurrent is anti-symmetric. The amplitude of V_{th} is directly related to the resistance of the side arms; the larger the resistance, the larger the thermal voltage generated and hence the larger the thermopower.

VH's analysis has successfully explained the anti-symmetric behavior of the thermopower oscillations of the "parallelogram" interferometer. But, unfortunately, it cannot explain the symmetric thermopower oscillations observed in the "house" configuration, because their interpretation requires the two NS interfaces to be at two different temperatures, which is not true for the "house" interferometer. For the "house" configuration, since the superconductors act as thermal insulating boundaries at low temperatures, there is no thermal current along the normal-metal arms between two NS interfaces. Therefore, one would expect that both NS interfaces should be at the same temperature. On the other hand, for a symmetric "house" interferometer as shown in Fig. 2.4(b), $Q = 0$ and $M_{03} = 0$, so that $V_{th} = 0$ in the normal-metal wires along the path of the thermal current. Indeed, VH explicitly state in their papers that their model cannot explain the symmetric thermopower oscillations observed in the experiments. However, VH also realize that the "house" interferometers measured in the experiments are actually not symmetric, where one of the side arms is much longer than another. Therefore, VH explain the symmetric thermopower oscillations in the "house" interferometer as a geometry effect.

In summary, we should emphasize that all the above theoretical studies suggest that the conversion from the supercurrent to quasiparticle current is the key to understanding the origin of the symmetry of thermopower oscillations.

CHAPTER 3

Experimental techniques

In the following chapter, we will first briefly describe the nanolithography techniques used in the sample fabrication process during this thesis work, ranging from substrate cleaning, photolithography, electron-beam (e-beam) lithography, etching and metalization to liftoff. Since many common techniques have been discussed in the thesis work of former graduate students of our group [**78, 79, 80**], we will mostly focus on the new techniques developed in the last few years. In addition, we will also describe the measurement techniques related to the experiments, including cryogenics, electronics and low noise measurements.

3.1. Sample fabrication

3.1.1. Wafer preparation

The typical wafer used in our devices is a one-side polished Si wafer[1] (0.02 inch thick) with a 30 nm oxidized layer covered on the surface. With a voltage differential less than 1 V, a 30 nm Si_2O_3 layer is thick enough to prevent leakage current from the metallic film sitting on the surface to the Si substrate, but does not result in significant charging effects in a scanning electron microscope (SEM).

The wafer needs to be prepared carefully, because there may be some chemical contaminants even on the surface of a new chip. In addition, the wafer is normally

[1]From Polishing Corporation of America.

cut by a diamond scriber into small pieces; many scraps may reside on the surface after cutting. The cleaning procedure is as follows.

(1) Soak the wafer in acetone using ultrasonic cleaning for about 3 minutes. The ultrasonic bath usually works very well to remove the scraps from the chip and the acetone can remove the grease or organic contaminants.

(2) Soak the wafer in isopropanol with ultrasonic cleaning for another 3 minutes.

(3) Rinse the wafer in 18 MΩ distilled (DI) water for 1 minute to take off the inorganic residues, such as salt.

(4) Rinse the wafer in isopropanol again for 1 minute to dissolve the water.

(5) Blow the wafer dry with pure N_2 gas immediately after taking the wafer out from the last rinse of isopropanol.

If the wafer is clean, when it is blown dry, the isopropanol should come off in a clean and uniform film on the wafer. If there is any dirt on the wafer, the film will *get stuck* on the dirt spots. If this occurs, the above cleaning procedure should be repeated until a clean surface is obtained. Furthermore, it needs to be pointed out that, except for the last drying step, one should not let any part of the wafer get dry, or else any residues in the solvent will dry on the wafer and will be difficult to remove later.

However, sometimes, the above procedure is still not enough, especially for old wafers which have been used for lithography before, because the residue of PMMA[2] and MMA/MAA[3] can stick to the surface of the wafer tightly. In this case, O_2 plasma etching (about 3 minutes) is required.

[2]950K molecular weight polymethylmethacrylate dissolved in anisole (4% by weight). From MicroChem Corp..

[3]Methylmethacrylate-co-methacrylic acid. From MicroChem Corp..

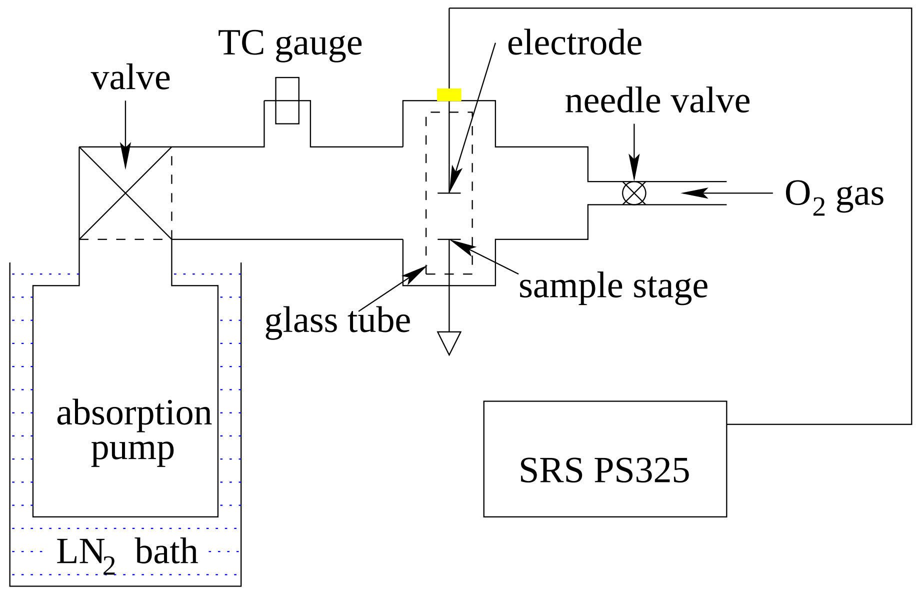

Figure 3.1. Schematic of the homemade dc plasma etcher for O_2 plasma etching.

The etcher used for such general cleaning is a homemade dc plasma etcher (see Fig. 3.1) built by a previous graduate student, José Aumentado. During the etching, the sample sits on a grounded stage and faces the counter-electrode which is about 3/4 inch away. Both the sample stage and the electrode are made of stainless steel. A clean glass tube is used to isolate the electrode and the sample stage from other parts of the etcher so that a relatively uniform plasma is generated on the top of the sample surface. After loading the sample into the etcher, the chamber is first pumped down by using a sorption pump (cooled down by liquid nitrogen) to base pressure, which is about 10 mTorr as read by a TC gauge. Pure O_2 gas is then introduced into the chamber and the flow is adjusted by the needle valve to keep the chamber pressure around 100 mTorr, while pumping with the sorption pump. In the next step, a -700 V dc voltage is applied by a SRS PS325 high voltage power supply[4] on the counter-electrode. Normally, by the time the power supply is turned on, a light-green

[4]From Stanford Research Systems.

O_2 plasma is generated. The plasma current is maintained at about 1.2 mA (as read by the power supply) by adjusting the O_2 flow using the needle valve. We use the etching time as the only tunable factor during the etching and keep the chamber pressure, dc voltage and plasma current constant. Under the above conditions, the etching rate as determined from atomic force microscope[5] (AFM) measurements is 1.5 nm per second.

Another candidate for O_2 plasma etching is the homemade reactive ion etching (RIE) system built by Zhengfan Zhang, which is powered by a PE-1000 ac plasma power source[6] at about 400 V. As with the dc plasma etcher, we normally keep the flow rate of the O_2 gas at about 100 mTorr and control the etching depth by tuning the etching time. Since this system is much more powerful than the dc etcher, it is not suggested to use it to remove a very thin layer of PMMA, but it is still good for general cleaning purposes like cleaning a wafer prior to sample fabrication. The typical time for general cleaning is 1 min. Details about this system will be described in the thesis of Zhengfan Zhang [**81**].

Note that both these two etchers are suitable for both dc and ac O_2 plasma etching with the appropriate power supply. We subjectively devote the first to quantitative dc plasma etching and the second to ac plasma etching at higher power. In addition, both these two etchers are also suitable for Ar^+ plasma etching. Ar^+ plasma etching is a different process compared with the O_2 plasma etching. It is a mechanical process, which can be used to peel off a thin layer of metal to remove its oxidized surface. The O_2 plasma etching, on the other hand, is a chemical process, which can be used to clean the substrate by removing the organic components like

[5]From Thermomicroscopes.
[6]From Plasma-Therm, Inc..

PMMA residue. However, during the Ar^+ plasma etching, charges may accumulate on the substrate and potentially can blow out the structures already patterned on it. In our experience, to avoid this problem, the substrate should be mounted on the counter-electrode with a good electrical contact with it (we normally use silver paint). A detailed description about Ar^+ plasma etching in an *in situ* etcher will be introduced later.

3.1.2. Photolithography

The typical size of a mesoscopic device fabricated in our laboratory is about 60 μm $\times$ 60 μm. However, in order to make transport measurements, we need to make electrical contacts to it. Hence, large area metal pads are necessary in order to connect the device to room temperature electronics. Although e-beam lithography is suitable for patterning such large area patterns, it is time consuming to make many of them. Therefore, photolithography is preferable.

Three different ways have been used in the past few years in our group to pattern the large area contact pads. Initially, we used the ultraviolet (UV) light generated by a Quintel Q-2001 CT mask aligner[7] in Prof. Ketterson's group to expose the substrate. The step by step procedure for this method has been described by José Aumentado in his thesis work [**80**]. The disadvantage of this method is that only a single layer of photoresist is used, so that one is not be able to make an undercut profile. Therefore, after deposition and liftfoff, one may have ragged edges on the metal pattern, which potentially can cause connection problems to subsequent fabrication layers. Because of the above reason, we then switched to bilayer photoresist

[7]From Quintel Corp..

and deep-UV exposure using a Quintel Q-4000 mask aligner in the Materials Research Center clean room. This method used to work very well. However, more recently, for reasons that are not entirely clear, we started to get inconsistent results. Hence we developed a new method that only requires a simple halogen lamp instead of a massive mask aligner to make the large area contact pads. The advantage of this method is that, with a relatively simple setup, one can get a well developed undercut ($\sim 0.5 - 1$ μm) after exposure, eliminating the connection problems. In this thesis, we are going to focus on this method. The fabrication details are listed below, and also demonstrated in Fig. 3.2.

(1) First layer. Spincoat[8] the polished surface of the substrate with LOR-7B[9] at a speed of 4000 RPM for 30 seconds. Bake the substrate in an oven at 170 ℃ for 45 minutes.

(2) Second layer. Spincoat the substrate with a layer of Shipley 1813 photoresist[10] at a speed of 3000 RPM for 40 seconds. Bake the substrate at 110 ℃ for 30 minutes.

(3) Exposure. The schematics of the setup for the exposure process are illustrated in Fig. 3.3, where we have a halogen lamp on the top and a home-made mask aligner[11] underneath. The technique used here is the so-called contact mask technique, hence it is crucial to ensure a tight contact between the substrate and the photomask during the exposure. A gap between the mask and the wafer would cause undesired patterns and failure to obtain an

[8]Spinner was purchased from Headway Research, Inc..
[9]From MicroChem Corp..
[10]From MicroChem Corp..
[11]This conformal mask aligner was machined in the University Machine Shop.

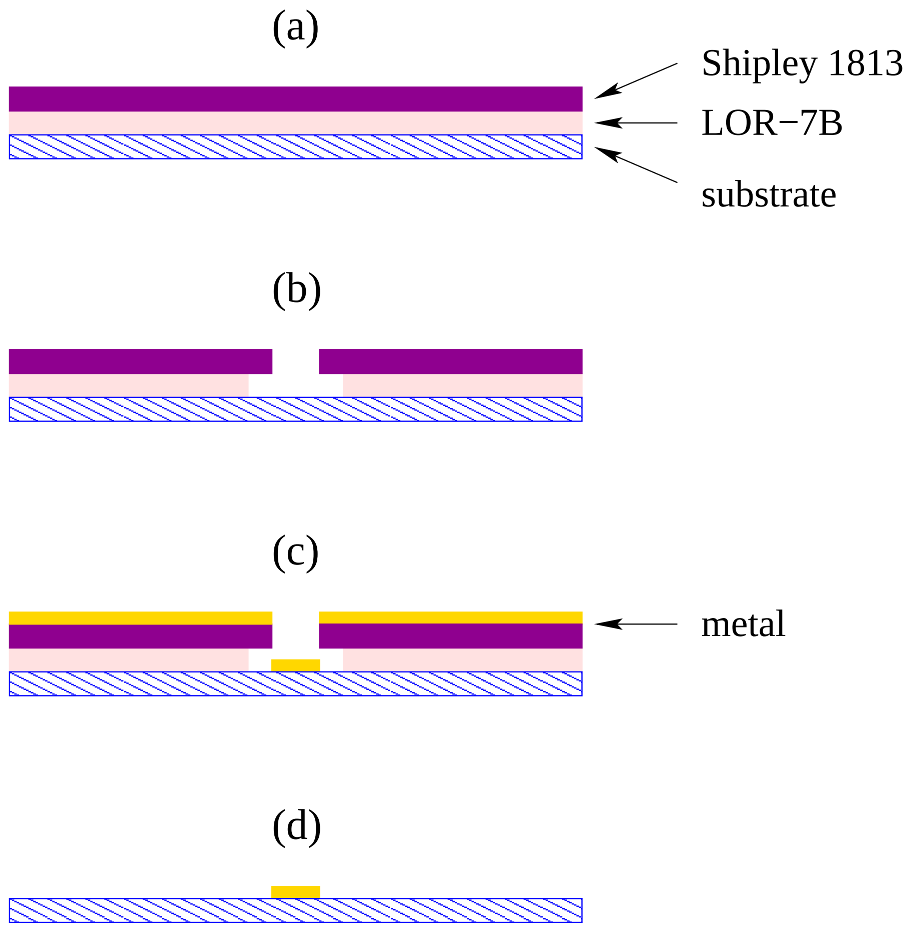

Figure 3.2. Schematics for photolithography: (a) Spincoat the substrate with LOR-7B (bottom layer) and Shipley 1813 photoresist (top layer). (b) Expose and develop. (c) Metalization. (d) Liftoff.

undercut due to the optical diffraction effect. The detailed operation procedure is as follows: (i) Unscrew the metal cover of the mask aligner, remove the thin Mylar sheet and place it face up to prevent contamination. (ii) Blow the photomask and the substrate with N_2 gas to ensure clean surfaces. Then load in the photomask with copper side facing up on a square polyethylene spacer and place the substrate face down on the photomask. Align the substrate properly by eye with Q-tips and place the Mylar sheet and the metal cover back. (iii) Turn on the vacuum. The purpose of the vacuum is to use the Mylar sheet to press the substrate on to the photomask, in order to get a tight contact between them, particularly ensuring no air bubbles in between. (iv) Flip the mask aligner over and align with the halogen lamp. Expose the substrate under the halogen lamp for 7 minutes. The light of the halogen lamp essentially goes through a glass window at the bottom of the aligner and the patterns on the photomask to the substrate, and breaks down the long polymers in the photoresist into shorter ones, so that the developer can remove them in the next step.

(4) Development. Develop the Shipley 1813 photoresist layer with the corresponding developer MF-319[12] for 60 seconds by using a constant jet of developer from a wash bottle. Rinse the substrate with DI water and blow it dry with N_2 gas. Develop the LOR-7B layer with SAL-101[13] for 2 minutes. Again, rinse with DI water and dry with N_2 gas. After development, a clear undercut profile can be seen in the LOR-7B layer under the optical microscope.

[12]From MicroChem Corp..
[13]From MicroChem Corp..

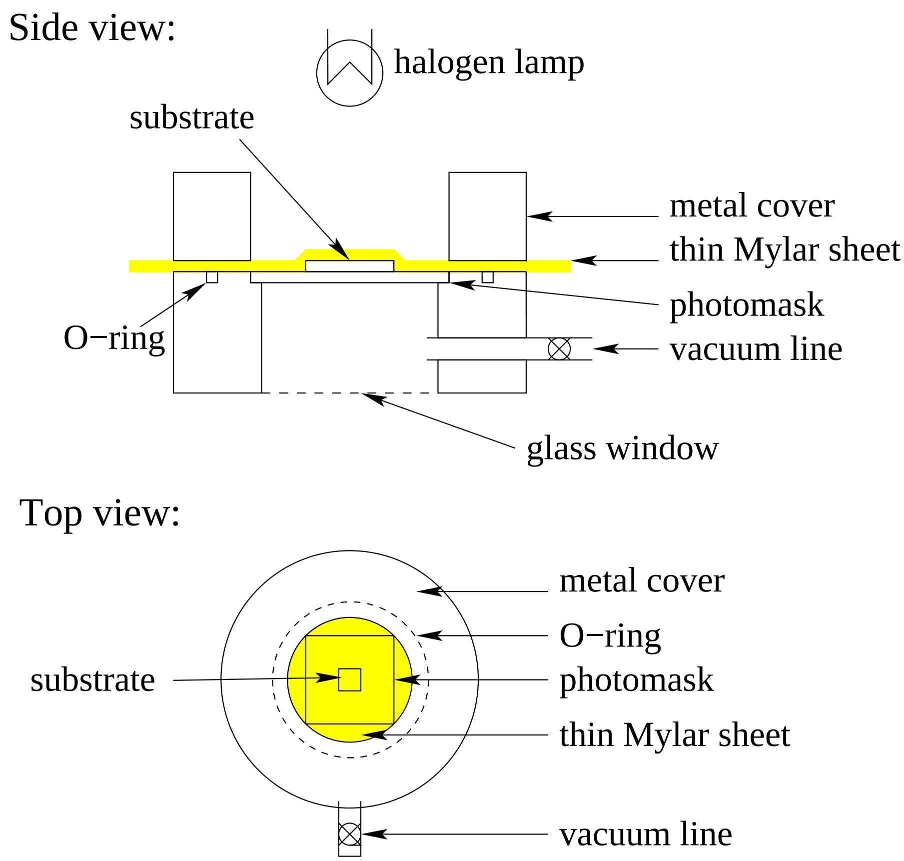

Figure 3.3. Schematics of the setup for the photo exposure process, where we have a halogen lamp on the top and a homemade mask aligner underneath. When we expose, we need to flip over the mask aligner in order to get the surface of the substrate exposed in the light of the halogen lamp.

(5) O_2 plasma etching. The purpose of this step is to remove the residue of the photoresist. For the dc plasma etcher, the typical etching time is 25 seconds. For the ac RIE system, it is 8 seconds.

(6) Metalization: electron-gun (e-gun) deposition. Deposit 4 nm Ti (4N5) and 25 nm Au (3N5). The purpose of the Ti layer is for adhesion, which ensures the Au layer adheres to the substrate when we soak the substrate in an ultrasonic bath in the next step.

(7) Liftoff. (i) Liftoff the Shipley 1813 photoresist layer by soaking the substrate in an ultrasonic acetone bath for 2 minutes. (ii) Liftoff the LOR-7B layer by soaking the substrate in the 1165 stripper for 10 minutes at 70 ℃ on the hot plate. (iii) Rinse the substrate with acetone and then isopropanol, and blow it dry with N_2 gas. Note that the flash point for the 1165 stripper is 88 ℃. We should monitor the temperature carefully in the second step of this liftoff procedure.

3.1.3. Fabrication of Si_3N_4 membranes

In order to measure the thermal conductance of mesoscopic samples, it is crucial to confine the path of the thermal current. One of the most challenging parts of the confinement is to eliminate the heat leak from the electron bath to the substrate by electron-phonon scattering. To avoid this problem, of course, a straight forward way is to go to low temperatures, where the electron-phonon scattering is negligible. But, there are other ways to achieve it. One of the most popular methods emerging recently is to fabricate the device on top of a thin Si_3N_4 membrane [**82, 83**], by taking advantage of modern nanolithography technology [**84, 85**]. During the period of this thesis work, we also developed a routine to make Si_3N_4 membrane devices in our laboratory, which is described in the following (also illustrated by Fig. 3.4).

(1) Wafer. The wafer used here is also a 0.02-inch-thick one-side polished Si wafer[14], but coated with a 50 nm Si_3N_4 layer instead of SiO_2.

(2) Spincoat. Using the parameters mentioned in the previous section, spincoat the polished surface of the wafer with the Shipley 1813 photoresist and bake

[14]From Polishing Corporation of America.

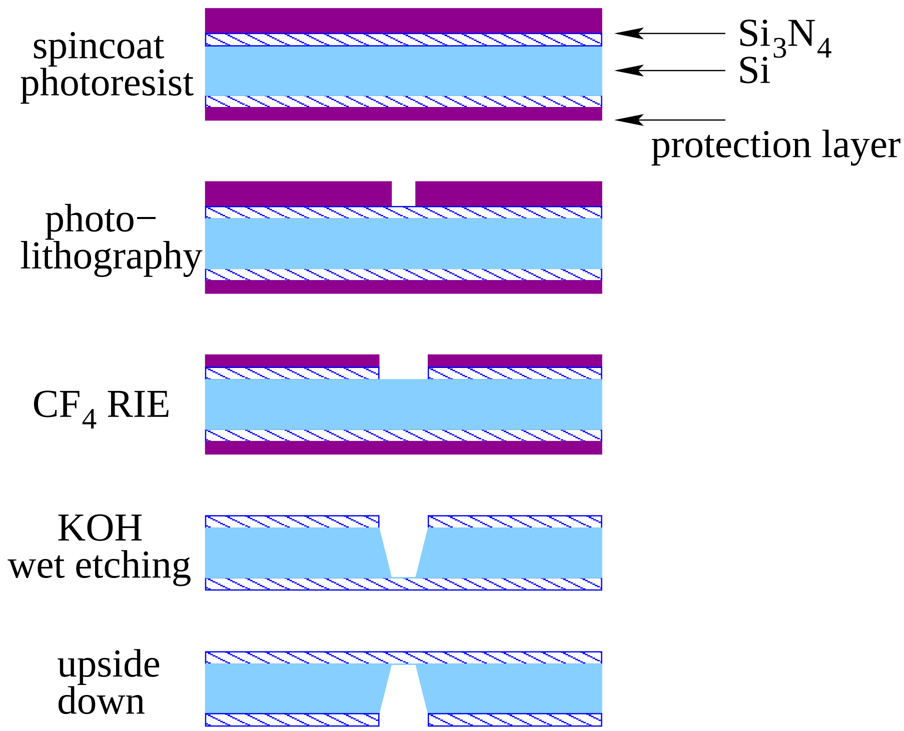

Figure 3.4. Schematics of the fabrication procedure for Si_3N_4 membranes: (a) Spincoat both sides of the wafer with photoresist. (b) Expose the back side of the wafer and develop it. (c) Use RIE to etch through the Si_3N_4 layer. (d) Use wet chemical etching (KOH) to etch down the Si. (e) Flip the wafer over and make patterns onto the top surface.

it properly. This layer of coating is just for protection of the top surface of the wafer. In addition, spincoat the back side of the wafer with the Shipley 1813 photoresist too and bake it.

(3) Exposure. Load the wafer into the Quintel Q-2001 CT mask aligner and expose an array of 757 μm $\times$ 757 μm squares on the back side of the wafer. The aim is to obtain 50 μm $\times$ 50 μm Si_3N_4 membranes on the top surface after etching. The exposure time is 30 seconds at a power of 150 W. We also can expose an array of 807 μm $\times$ 807 μm squares for 100 μm $\times$ 100 μm Si_3N_4 membranes, but they are easy to break in the later multilayer e-beam lithography process.

(4) Development. Develop the Shipley 1813 photoresist with MF-319 for 60 seconds and rinse the wafer with DI water, then blow it dry with N_2 gas.

(5) RIE. Use the homemade RIE system in Prof. Ketterson's laboratory. Flow CF_4 gas into the chamber and keep the pressure at 50-55 mTorr. Etch the back side of the wafer for 50 seconds at a power of 46 W.

(6) Cleaning. Wash out the Shipley 1813 photoresist by acetone and rinse the wafer with isopropanol, then blow it dry with N_2 gas.

(7) Wet chemical etching. Dissolve the solid potassium-hydroxide (KOH) in DI water (20% by weight) in a ceramic pitcher and soak the wafer in it. Use a hot plate and a digital temperature controller to keep a water bath at 80 ℃ and dip the ceramic pitcher in it. Etch the wafer for about 8 to 9 hours. At the end of etching, check the wafer by optical microscope every half an hour. A fully etched Si_3N_4 membrane looks very bright under the microscope due

to the penetration of the light. In addition, the membrane should be uniform and its edges should be smooth.

(8) Cleaning. Wash out the KOH solution with DI water and go through the standard cleaning procedure to clean up the wafer, except that the ultrasonic bath is not allowed for Si_3N_4 membranes, since it will break the membranes in a second.

3.1.4. E-beam lithography

The procedure for e-beam lithography is similar to photolithography. The main differences are: (1) we use a JEOL JXA-840 SEM instead of the halogen lamp to expose the substrate; (2) we use different resists and developer[15]. The standard e-beam lithography procedure is as follows.

(1) Spincoat. Spincoat the substrate with MMA/MAA at a speed of 3000 RPM for 60 seconds. Bake the substrate at 140 ℃ for 30 minutes. Spincoat the substrate with 950K PMMA at a speed of 8000 RPM for 60 seconds. Bake the substrate at 170 ℃ for another 30 minutes. For samples with Ni, permalloy (NiFe) or Cu deposited on it, to avoid the oxidization (or chemical reactions), we normally bake the substrate at 80 ℃ for one hour for both above two layers.

(2) Exposure. Expose the substrate by e-beam with desired patterns. This step is performed in SEM and controlled by a PC computer. Depending on the substrate, the charge dosage used for exposure is quite different. For example,

[15]From MicroChem Corp..

at 5000 magnification, it is 460 μC/cm^2 on SiO_2 substrates, 650 μC/cm^2 on Si_3N_4 membranes.

(3) Development. Use Methyl isobutyl ketone-co-isopropanol (MIBK/IPA)[16] to develop the substrate at a temperature of 24 ℃ for 60 seconds by a constant jet of developer from a wash bottle. Then, rinse it with isopropanol and dry it with N_2 gas.

(4) Plasma etching. For O_2 plasma etching, we normally use the dc plasma etcher. The typical etching time is 25 seconds. In order to increase the interface transparency between two different types of metals, such as between N and S or F and S, *in situ* Ar^+ plasma etching has been used to clear the sample just before the next layer of deposition.

(5) Metalization. We use the homemade e-gun evaporator[17] to deposit *dirty* metals, such as Ni (4N5), NiFe, Al (5N), Ti (4N5) and Au (3N5). For *clean* metals, Au (5N, 6N) and Cu (6N), a commercial Edwards thermal evaporator[18] has been used.

(6) Liftoff. Soak the substrate in acetone for about 5 minutes. Rinse it with isopropanol, and blow it dry with N_2 gas.

At the end of this section, we would like to address three aspects in the e-beam lithography procedure that are particularly important to the success of our sample fabrications.

[16]MIBK is purchased from Fisher Scientific. It is dissolved in the isopropanol solvent at a ratio of 1/3 by volume.
[17]The e-gun is model 528-5 from TFI Telemark.
[18]Edwards 306 vacuum coater.

First of all, noise control. During the patterning, the electron beam raster of the SEM is controlled by a PC computer via a D/A card[19]. The schematic of the control circuit can be found in Ref. [**79**]. However, recently, this control circuit suffers from the increase of environmental noise, mostly at the line frequency of 60 Hz. Figure 3.5(a) shows an image of our sample. The edges of the device show a sawtooth pattern that is due to line frequency interference in the raster scan. The length scale of the noise pattern is almost 100 nm. This problem has been solved by replacing the input operational amplifiers LF356 of the circuit with the precision instrumentation amplifiers AD524[20] and connecting their negative input pins to the common ground of the D/A card and their reference output pins to the ground of the SEM. With the above modifications, we avoid ground loops in the control circuit and hence reduce the noise dramatically. Figure 3.5(b) shows an image taken by using the new circuit, which basically has no visible noise pattern on the edge. We estimate the length scale of the noise pattern to be 10 nm.

Next, alignment ability. In the fabrication process, probably the most difficult part of it is to get good alignment between different layers of patterns. As indicated by the theoretical calculations in Chapter 2, good alignment would help us get larger signals. The way we do the alignment is as follows: we first pattern alignment marks onto the substrate, we then use the homemade patterning program developed by Prof. Chandrasekhar to open an image window just on the top of those alignment marks and align the next layer of pattern accordingly. Apparently, the precision of the alignment will depend on the image quality and the stability of the SEM. Figure 3.6 shows a sample with three layers aligned onto one set of alignment marks. These three

[19] From National Instruments.
[20] From Analog Devices.

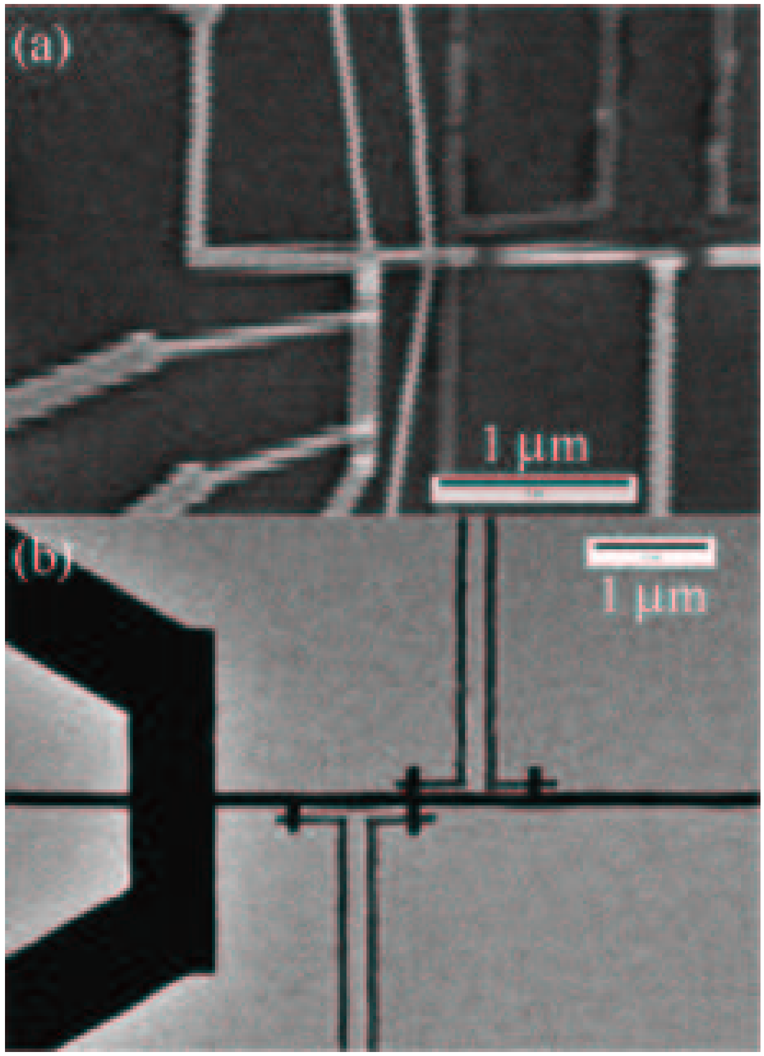

Figure 3.5. SEM images with and without 60 Hz noise. (a) Taken by using the old control circuit with the LF356 chips inside. The length scale of the noise pattern is almost 100 nm. (b) Taken by using the new control circuit equipped with the AD524 amplifiers. The length scale of the noise pattern is about 10 nm.

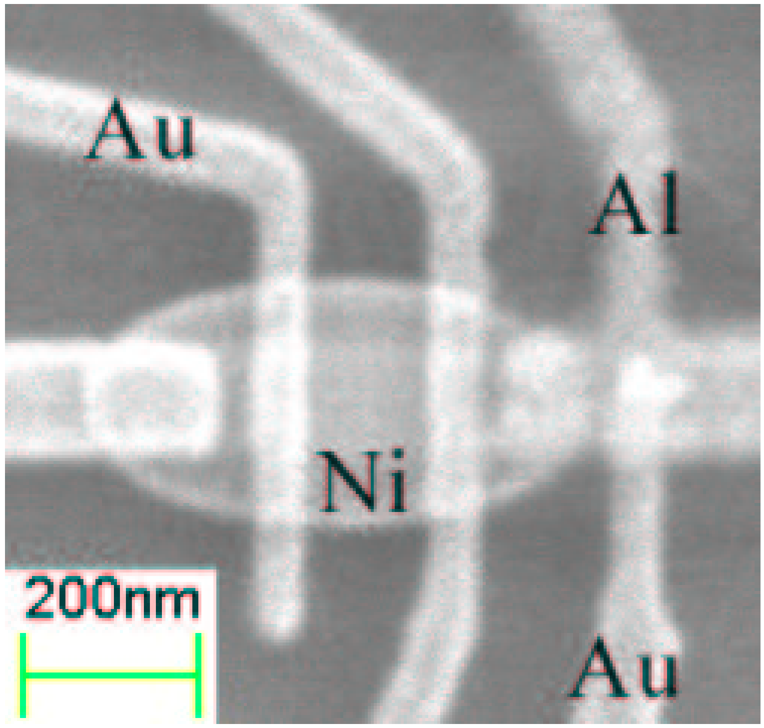

Figure 3.6. SEM image of a sample with three layers aligned onto one set of alignment marks. The alignment mismatch between layers is better than 10 nm.

layers are Ni layer, Au layer and Al layer respectively. We estimate the alignment mismatch between layers is better than 10 nm for this sample. It should be less than 30 nm in general.

The last one, *in situ* Ar^+ plasma etching. Almost all the physics of interest near the NS or FS interfaces strongly depends on the quality of the interface. In order to obtain highly transparent interfaces, *in situ* Ar^+ plasma etching is performed inside both the e-gun evaporator and the Edwards thermal evaporator to clean the sample just before the next layer of deposition. The setup of the *in situ* etching has been shown in Fig. 3.7, where we simply use a high voltage (2 kV) transformer[21] (60 Hz) instead of a commercial radio-frequency (rf) power supply (13.56 MHz). Before

[21]From United Transformer Company.

metal	Cu	Au	Ni
rate	0.99 nm/min	1.12 nm/min	0.53 nm/min

Table 3.1. Etching rate for *in situ* Ar^+ plasma etching.

interface	Ni/Al (mΩ μm^2)	Au/Al (mΩ μm^2)
in situ Ar^+	20-40	1.4-2.6
external Ar^+	370-19k	N/A
external O_2	Ni oxidized	17

Table 3.2. Specific resistance of Ni/Al and Au/Al interfaces with and without *in situ* Ar^+ plasma etching.

etching, we first pump down the chamber of the evaporator. For the e-gun evaporator, we normally pump it for about 1 hour to $\sim 3 \times 10^{-7}$ Torr; for the Edwards thermal evaporator, we pump it for about 3 hours to $\sim 5 \times 10^{-7}$ Torr. We then fill the chamber with 40 mTorr pure Ar gas and turn on the plasma. The generated plasma is stable and uniform around the sample area. The etching time is typically 80 seconds. After etching, we pump down the chamber again for several minutes until the pressure is close to the previous value; we then deposit metal onto the sample. The etching rate for different metals has been calibrated by AFM measurements, the results are shown in Table 3.1. A systematic study of the specific resistance also has been done for FS and NS interfaces, which shows that the *in situ* Ar^+ plasma etching indeed improves the transparency of the interfaces. For example, as listed in Table 3.2, the typical Ni/Al interface resistance with *in situ* Ar^+ plasma etching is 20-40 mΩ μm^2. Compared with the interfaces cleaned by an external Ar^+ plasma etching, where the specific resistance changes randomly over a large range of order 0.37-19 Ω μm^2, the *in situ* cleaned interfaces are quite consistent from sample to sample. To our knowledge,

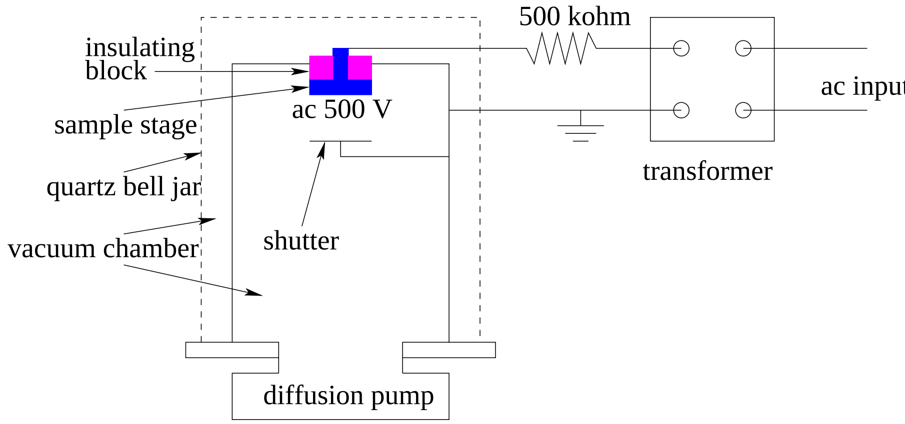

Figure 3.7. Schematic of the setup of the *in situ* Ar^+ plasma etching inside an evaporator. The sample is typically silver-painted on to the sample stage, where an ac voltage of 500 V is applied during the etching.

the most effective way to increase the transparency of the interfaces is *in situ* Ar ion milling, which has a specific resistance of 6 mΩ μm^2 [**40, 86**] for FS interfaces.

3.2. Measurement techniques

3.2.1. Cryogenics

Most of the thermal transport measurements discussed in this thesis were performed using an Oxford Kelvinox 300 dilution refrigerator capable of a temperature as low as 20 mK. The sample is in vacuum and mounted onto a cold finger that extends from the mixing chamber. The temperature of the sample is read out by the resistance of a RuO_2 thermometer[22] mounted on the mixing chamber. The RuO_2 thermometer was calibrated by another Ge thermometer[23] thermally sunk nearby. Although measuring a resistance seems to be trivial, at low temperatures, special care is needed to avoid self heating stemming from the measuring current. In our experiments, we use a

[22]Model SMT1206R from Vector Electronic Company with about 1 kΩ resistance at room temperature.
[23]Calibrated by Lake Shore Cryotronics, Inc..

commercial TRMC2 multi-probe regulator[24], which is specially designed for the low temperature measurements with a current as small as 10 pA. To stabilize the temperature, we use the differential analog output from the TRMC2 and a homemade PID box [**79**]. The former essentially gives us a voltage proportional to the difference between the setup temperature and the real temperature readout, while the latter stabilizes the temperature accordingly by sending a current into the mixing chamber heater.

For the thermopower measurements and the spin transport measurements described in Chapter 5 were performed in a closed cycle ^{3}He refrigerator[25] with a base temperature of 260 mK. This system has a two-axis magnet[26], which can generate a 1 T transverse field and a 3 T axial field simultaneously. Again, a 1 kΩ RuO_2 thermometer has been used to monitor the temperature, which is read out by a homemade temperature bridge [**78**] and stabilized by a second homemade PID box. For the homemade electronics mentioned above and other related homemade devices, the circuit diagrams can be found in Ref. [**78**], [**79**] and [**80**].

3.2.2. Magnetic field control

A magnetic field is normally applied onto our samples by sending a current into the superconducting magnet coil. The current is provided by one of three power supplies: for a high magnetic field, we use a 120 A bipolar superconducting magnet supply from Lakeshore[27]; for medium magnetic fields, a 20 A Kepco bipolar operational

[24]From AIR LIQUIDE.
[25]Janis Research Company, Inc..
[26]From Cryomagnetics, Inc..
[27]Lakeshore 622, from Lake Shore Cryotronics, Inc..

power supply[28] has been used; for very small magnetic fields, a 1 A Kepco bipolar operational power supply[29] is preferred.

The magnetic field can also be applied locally by fabricating a field coil on chip. In fact, a field coil is simply a superconducting wire, which is properly designed and deposited closely to the sample. By sending a current into the superconducting wire, one can generate a magnetic field locally without inducing an appreciable heating effect. Figure 3.8 shows a device with two such field coils, by which one can easily control the local magnetic field in the center of each field coil by tuning the direction and the magnitude of current in the coil. However, this design also has drawbacks: (1) First, the induced local field cannot be very large. For the device shown in Fig. 3.8, passing a $\sim 69\ \mu$A dc current in the field coil can only generate 1 quantum flux $\Phi_0 = h/2e$ through one of the interferometer loops. (2) Second, the induced local field is not homogeneous.

3.2.3. Low temperature measurements and electronics

The major technical concern in our experiments is always the noise issue, which needs to be considered carefully at each stage of wiring and electronics setup.

3.2.3.1. Wiring

To fulfill the transport measurements, we need extend the electrical lines from the sample holder to the electronics setup at room temperature. Cu twisted pairs are used in the first stage, from the sample holder to the mixing chamber of the dilution refrigerator or the ^{3}He pot of the ^{3}He refrigerator. These wires have been thermally

[28]Kepco Bop 20-20M, from Kepco, Inc..
[29]Kepco Bop 100-1M, from Kepco, Inc..

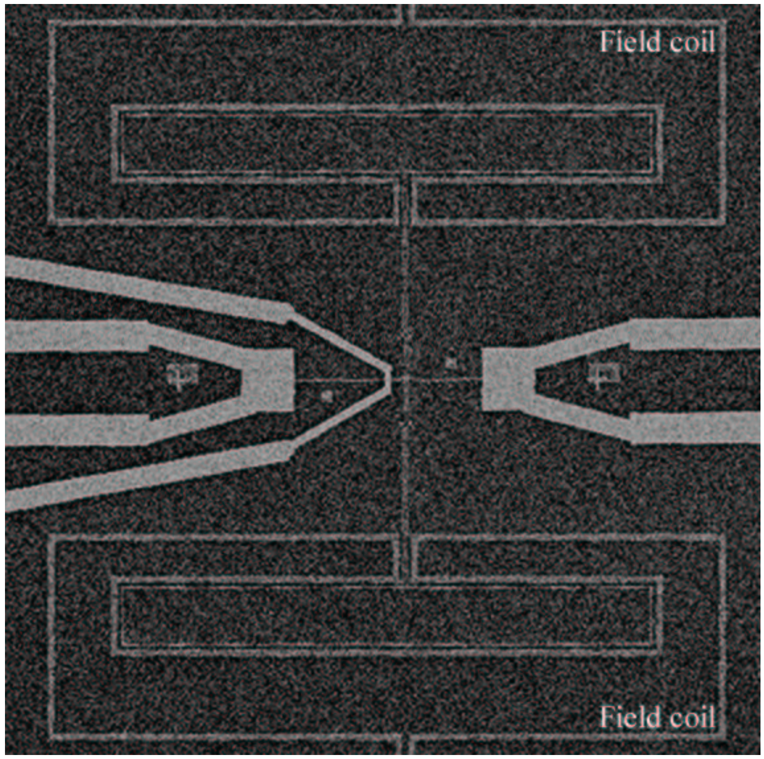

Figure 3.8. SEM image of a device with two field coils patterned on it. By sending a current into the field coils, one can generate magnetic fields locally in the center of the coils.

sunk by winding around a Cu rod mounted on the mixing chamber or the ^{3}He pot. In the second stage, superconducting twisted pairs (NbTi in a CuNi matrix[30], 0.004 inch in diameter) are used to extend the Cu twisted pairs to the top of the refrigerator. They are also thermally sunk at different temperature stages. On the top of the refrigerator, each electrical line is filtered with a π-section filter[31] with a cut-off frequency of 5 MHz. These π-section filters are installed in a rf sealed and waterproof metal box just after the vacuum seals, to minimize sample heating due to the ambient radio-frequency (rf) sources.

[30]From Supercon, Inc..
[31]From Murata Electronics North America, Inc..

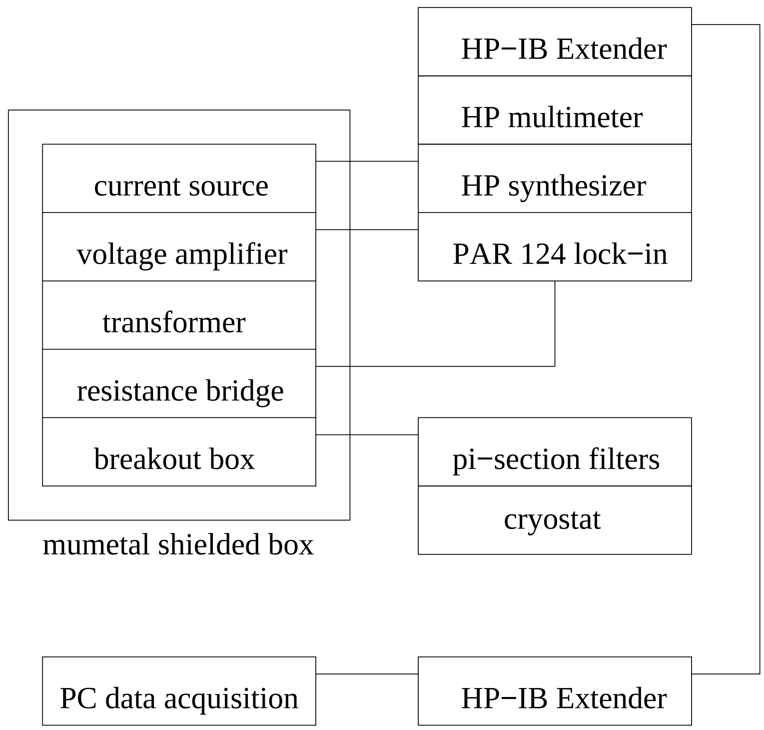

Figure 3.9. Typical electronics setup used in our experiments.

3.2.3.2. Electronics setup

Figure 3.9 illustrates an example of the electronics setup used in our experiments. The electrical lines coming from the π-section filters are first connected to a breakout box inside a mumetal shielded box[32], which is placed as closely as possible to the top of the refrigerator to reduce interference and inadvertent heating from line frequency sources. All the electronics that can be powered by batteries has been powered by batteries and put into the mumetal shielded box. These electronics include a resistance bridge[33], step-up transformer[34], instrumentation amplifier[35] and current source. The resistance

[32]Homemade design, manufactured by Amuneal Manufacturing Corp..
[33]This is an Adler-Jackson type bridge [**87**], modified based on a General Radio 1433-X or 1433-F bridge.
[34]From United Transformer Company.
[35]AD624, from Analog Devices.

of the sample was typically measured by a conventional four-probe technique using an ac resistance bridge with an excitation current generated by a lock-in amplifier (PAR 124)[36]. In order to increase the measurement sensitivity, the step-up transformer, the instrumentation amplifier and the lock-in amplifier[37] have been used in series to amplify the signal out of the resistance bridge. The background noise from the spectrum of the signal, as measured by a spectrum analyzer[38] attached to the lock-in amplifier, was approximately 6 nV/$\sqrt{\mathrm{Hz}}$, close to the 4 nV/$\sqrt{\mathrm{Hz}}$ expected input noise of the instrumentation amplifier, and showed an essentially flat frequency response (with no peaks at the harmonics of the line frequency) up to the maximum frequency of 100 kHz of the analyzer. In order to maximize the gain of the transformer, a frequency of 10-130 Hz was used for the measurements. The analog dc output of the lock-in amplifier is read by a HP multimeter[39].

In addition, we often need to send a dc current into the sample during the measurements. A homemade current source was designed to achieve this purpose, which converts a voltage input to a current output ranging from a couple of nanoamps to hundreds of microamps. The voltage input is normally generated by HP synthesizers[40] sweeping at a frequency as low as 1 μHz. In this setup, the current is introduced at the I_+ contact, while the I_- contact is grounded. However, in some special conditions such as in some non-local resistance measurements, the I_- contact is not preferable as a ground, so that a floating current source is required. A simple schematic is shown in Fig. 3.10(a) to demonstrate the basic idea of the non-local resistance measurements,

[36]From Princeton Applied Research.
[37]Model 116(A) differential preamplifier.
[38]SR760 FFT spectrum analyzer, from Stanford Research Systems.
[39]Model 34401A, from Hewlett Packard.
[40]Model 3325A, from Hewlett Packard.

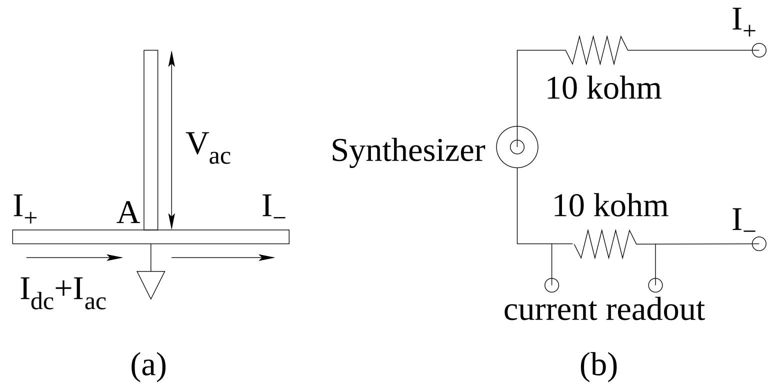

Figure 3.10. (a) Schematic of the non-local resistance measurement, where the ac voltage differential V_{ac} is measured across the segment of the sample which is not on the path of the ac excitation current I_{ac}. In order to obtain better signal-to-noise ratio, the grounding point is set in the middle of the device (point A). (b) Schematic of the floating current source, where I_{-} is not the grounding point. Note that the value of resistance can be modified depending on the measurement conditions.

where the ac voltage differential V_{ac} is measured across the segment of the sample which is not on the path of the ac excitation current I_{ac}. In this configuration, V_{ac} is superposed on V_A, the voltage at the joint point A. A typical example of such non-local resistance measurements is the thermopower measurements, in which the amplitude of V_{ac} is normally much smaller than V_A if we ground the device at I_{-}. Hence, in order to obtain better signal-to-noise ratio, the grounding point needs to be set at point A. Since the sum of the resistance of our sample and the wiring is typically below 200 Ω at low temperatures, a floating current source can be fulfilled simply by a couple of resistors. Figure 3.10(b) is the schematic of such a floating current source, where I_{-} is not the grounding point. The dc current through the sample can be read out by the voltage across the 10 kΩ resistor by a HP multimeter.

The HP multimeters are connected to a HP-IB extender[41], which sends the readings of the multimeters to a second HP-IB extender connected to a PC computer, but cuts off the grounding link between them to avoid the noise from the PC computer. The data acquisition is performed by a Windows-interfaced program written by Prof. Chandrasekhar. This program is capable of reading and program controlling the devices through the GPIB connections.

3.2.3.3. ac lock-in techniques: dV/dI and d^2V/dI^2 measurements

Measuring the differential resistance dV/dI at zero and finite bias is the basic operation in our work. A conventional four-probe technique using an ac resistance bridge and a PAR 124 lock-in amplifier has been performed in our experiments. The detailed description of such operations has been presented in the thesis work of former graduate students [**78, 79, 80**].

In this section, we will focus on the second derivative technique[42] used in the thermopower measurements. In these measurements, an ac excitation current with a frequency of f was sent into the sample, while d^2V/dI^2 is determined by measuring the ac voltage drop at a frequency of $2f$ and a phase of 90°. As shown in Fig. 3.11, this method requires two PAR 124 lock-in amplifiers. The operation procedure is the following.

(1) Set the sinusoidal oscillator of the No. 1 lock-in amplifier at a frequency of f, and use the conventional four-probe technique to measure the first derivative signal, dV/dI. Tune the phase of the oscillator accordingly.

[41] Model 37204, from Hewlett Packard.

[42] It actually can measure the first derivative dV/dI at the same time.

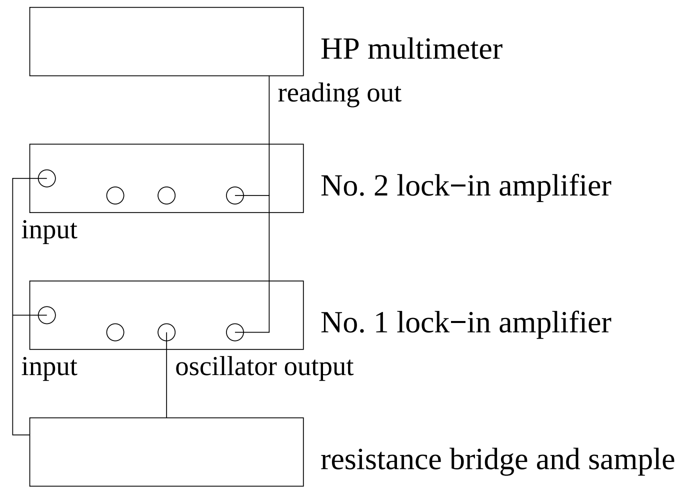

Figure 3.11. Schematic of the second derivative technique, which requires two Par 124 lock-in amplifiers. One sends an ac excitation current with a frequency of f, another picks up the corresponding ac voltage drop at a frequency of $2f$ and a phase of 90°.

(2) Use the No. 1 lock-in amplifier as the external reference (ext. $f/2$ mode) of the No. 2 lock-in amplifier, and synchronize the signal channel frequency of the No. 2 lock-in amplifier to $2f$.

(3) Send an excitation current with a frequency of f from the No. 1 lock-in amplifier into the sample through the ac resistance bridge. Take the ac voltage drop of interest to the input of the No. 2 lock-in amplifier and phase it accordingly. Measure d^2V/dI^2 at a frequency of $2f$ and a phase of 90°. Meanwhile, if we split the ac voltage drop and send it to the No. 1 lock-in amplifier, we would obtain dV/dI simultaneously.

Mathematically, the second derivative technique can be understood as follows.

$$\begin{aligned} V(I) &= V(I_{dc} + I_\circ \sin\omega t) \\ &\approx V(I_{dc}) + \frac{\partial V}{\partial I} I_\circ \sin\omega t + \frac{1}{4}\frac{\partial^2 V}{\partial I^2} I_\circ^2 (1 - \cos 2\omega t). \end{aligned} \tag{3.1}$$

Hence, by picking up the signal at a frequency of $2f$ and a phase of $90°$, we essentially get $(I_\circ^2/4)(\partial^2 V/\partial I^2)$. The detailed application of the second derivative technique will be described in the next chapter.

To conclude this section, we would like to address that our experiments are extremely sensitive to noise. Even a tiny ground loop may cause an appreciable effect which could bury the measurement signals. Thus, we normally continuously monitor the noise of the system in the frequency range of 0-100 kHz by using a SR760 FFT spectrum analyzer, and record it before each set of measurements.

CHAPTER 4

Experimental results: Thermal conductance and thermopower of Andreev interferometers

In principle, thermal and thermoelectric measurements are trivial. First of all, we need to heat up one end of the sample and measure the temperature differential ΔT across it. Then, for the thermal conductance measurement, we measure the thermal current I^T through the sample and calculate the thermal conductance by the ratio of I^T to ΔT (*i.e.*, $G^T = I^T/\Delta T$); for the thermopower measurement, we measure the thermoelectric voltage V_{th} across the sample and calculate the thermopower by the ratio of V_{th} to ΔT (*i.e.*, $S = V_{th}/\Delta T$).

In practice, thermal transport measurements are more complicated than electrical transport measurements. Thermal transport measurements require a well defined thermal current path and the ability to measure local electron temperatures. In this chapter, we will first introduce the local thermometry technique used in our experiments. Then we will describe the thermal conductance measurements of Andreev interferometers and compare the experimental results with our numerical simulations. Finally, we will discuss the recent studies of the symmetry of the thermopower oscillations of Andreev interferometers with respect to the applied magnetic flux. This experiment was performed in a device in which we can change the supercurrent distribution. We find that the thermopower can be either symmetric or anti-symmetric in the same device depending on its supercurrent distribution.

Additionally, it is important to note from the beginning that, in this chapter, we study the *electronic* thermal properties of Andreev interferometers, in that the temperature differential ΔT is generated and measured in the electron bath. In order to do so, we perform the measurements at very low temperatures and take special care in designing and fabricating the samples to eliminate the coupling between the electrons and the phonons.

4.1. Local thermometry technique

4.1.1. Overview of local thermometry techniques

In our devices, we normally connect one end of the sample to a metallic wire, the so-called heater. By sending a dc current through the heater, we can heat up this end of the sample to a temperature higher than the substrate temperature T_b, while keeping the substrate and other parts of the sample cold. The typical size of the heater is $\sim 0.7 - 1$ μm wide and $\sim 20 - 25$ μm long in our devices. In this configuration, since the length of the heater L is much larger the electron-electron characteristic scattering length l_{e-e}, the electrons in the heater would achieve local thermodynamic equilibrium by energy exchange between electrons [**88, 89**], where l_{e-e} is given by

$$l_{e-e} = \left[\left(\frac{\sqrt{2}}{k_B} \right) \left(\frac{\hbar}{e} \right)^2 \frac{Dw}{TR_\square} \right]^{1/3}, \tag{4.1}$$

here D is the electronic diffusion coefficient, w the width of the heater and $R_\square$ the sheet resistance of the heater. Applying the experimental parameters ($D = 104$ cm^2/s and $R_\square = 0.335$ Ω) into Eqn. (4.1), we get $l_{e-e} = 4.7$ μm at 100 mK, close to the value in Ref. [**89**]. As the local electron temperature T_e in the heater is higher than T_b, a temperature gradient can be generated in the electron bath. Conventional low temperature thermometers cannot be used to make a direct measurement of T_e on mesoscopic samples, because their physical size is much larger than the sample of interest. Hence, special thermometry techniques are needed on the submicron length scale.

As pointed out by Prof. Olli V. Lounasmaa [**90**], in low temperature physics it is important but difficult not only to reach the low temperature but also to measure it. Recently, spurred by the interest in measuring thermal and thermoelectric properties of mesoscopic structures, local thermometry techniques are attracting much more attention (see a review article: Ref. [**90**]). Taking advantage of modern nanolithography technology, these new thermometers are typically very small and their thermal relaxation times are usually short. They are designed to have good thermal coupling to the electron bath, but only allow a very tiny amounts of self-heating. These thermometers can be broadly divided into three categories.

(1) Coulomb blockade thermometry (CBT): The CBT has been studied extensively [**91, 92, 93, 94, 95**] and developed into a commercial product in the last decade. It operates in a temperature regime where the thermal energy k_BT is larger than the charging energy E_c of the single electron tunneling device. Due to the competition between the thermal energy k_BT, the electrostatic energy eV and the charging energy E_c, the dI/dV *vs.* V characteristics of the CBT show strong temperature dependence at a temperature as low as a few tens of millikelvin. In particular, the Coulomb blockade effect is illustrated as a dip in the dI/dV *vs.* V curve and the full width of this dip at the half minimum is approximately proportional to the temperature T, which allows the CBT to work as a primary thermometer.

(2) Noise thermometry: It has been almost 80 years since Johnson noise $S_I(T) = 4k_BT/R$ was exploited in thermometry. More recently, shot noise $S_I(T) = 2eI\coth(eV/2k_BT)$, which is essentially the second moment in the full counting statistics [**96**], also has been used to determine the electron temperature of normal metal systems [**97**]. As with the CBT, this type of thermometry is a primary thermometer; but beyond the CBT, it operates in a temperature regime of over four orders of magnitude, in the range of dilution refrigerator temperature to room temperature. However, this technique imposes restrictive constraints on the design of the samples. For example, noise measurements typically have a cutoff sensitivity below which the measurement accuracy drops. Henny *et al.* [**98**] mentioned a cutoff at a value of 2×10^{-20} $\mathrm{V}^2\mathrm{s}$, which requires a minimum thermometer resistance of 3.6 kΩ at 100 mK. Superconducting quantum interference devices (SQUIDs) can increase the sensitivity of noise measurements, but need relatively complicated circuits and sample fabrication [**97, 99, 100**].

(3) Thermometry based on hybrid junctions: In this category are included the local thermometry technique used in our thermal conductance and thermopower measurements of Andreev interferometers. The advantage of our thermometers is that they are well coupled to the electron bath and have relatively high sensitivity, but require minimum fabrication and electronics to read out the temperature. Particularly, our thermometers can also be easily integrated into complex samples, which cannot be said of all the other

thermometers. The earlier version of our thermometer is based on the superconducting proximity effect [**101**], in which the resistance of a proximity-coupled normal metal shows a temperature dependence at a temperature below the transition temperature T_c of the superconductor. The overall resistance change of this thermometer is $\sim$ 1-5% of the normal state resistance (measured at a temperature just above T_c) and can be used to determine the electron temperature over a 100 nm size scale. However, unfortunately, a 5% resistance change cannot always give one enough sensitivity to precisely measure a small temperature differential across a sample. Therefore, more recently, we developed a more sensitive thermometer based on the resistance of a SNS junction device that shows a much stronger temperature dependence at low temperatures [**102**]. The overall thermometer resistance change, from 18 mK to $\sim$ 350 mK, is up to 102% of the normal state resistance, and consequently, this thermometer is almost two orders of magnitude more sensitive than that of Ref. [**101**].

Another type of thermometer in this category is the tunnel junction thermometer, where an insulating layer is sandwiched between two different conductors. A typical example of it is the SIN tunnel junction thermometer, where SIN stands for the superconductor/insulator/normal-metal junction. As with our SNS junction, the current-voltage $(I - V)$ characteristics of the SIN tunnel junction thermometer usually strongly depend on the temperature, which enable it to work as a thermometer as well [**103, 104, 105**]. Note that this type of thermometer is an alternate candidate for our thermal transport measurements.

4.1.2. Local thermometry technique based on proximity-coupled SNS devices

Figure 4.1(a) shows a SEM image of the "parallelogram" Andreev interferometer fabricated for thermal conductance measurements. This device was patterned using conventional multilevel e-beam lithography[1]. A 46-nm-thick Au film (brighter regions in the image) was deposited first. A 76-nm-thick Al film (darker regions) was then deposited on top of the Au film in another level of lithography, after an *in situ* Ar^+ plasma etching was used to increase the transparency of the NS (Au/Al) interfaces. As shown in Fig. 4.1(a), this device can be divided into four sections: (1) The "Hot" section, on the left, consists of a heater and a "Hot" thermometer. By passing a dc current through the heater, one can increase the electron temperature T_e of this section above the substrate temperature T_b. (2) The "Cold" section, on the right, includes a "Cold" thermometer and a large normal metal pad as a reservoir. (3) The sample section consists of the structures between the "Hot" and "Cold" sections. As shown in Fig. 4.1(b), the sample is essentially a "parallelogram" Andreev interferometer. Since the "Hot" and "Cold" sections are at different temperatures, a temperature gradient is generated across the sample. The exact value of the temperature differential can be accurately controlled by the dc current through the heater. (4) The last section is a single thermometer electrically isolated from the rest of the sample, which measures the temperature of the substrate. This "Sub" thermometer can be used to monitor the heat leak from the heater to the substrate by electron-phonon scattering.

[1]This sample was fabricated on a Si wafer covered with a 30 nm Si_2O_3 layer.

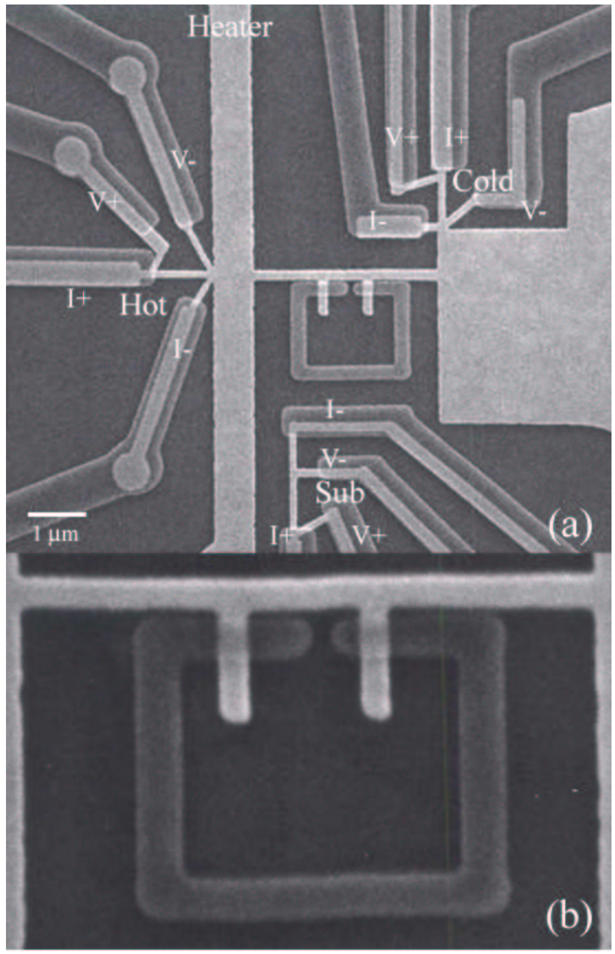

Figure 4.1. (a) SEM image of the "parallelogram" Andreev interferometer patterned for the thermal conductance measurements. The brighter regions are composed of normal metal (Au), while the darker regions are superconductor (Al). The device consists of three thermometers. The one coupled to the heater is labeled "Hot" (length: 0.95 μm, width: 0.13 μm); the one away from the heater on the right side is labeled "Cold" (length: 0.67 μm, width: 0.13 μm); the one on the substrate is labeled "Sub" (length: 0.91 μm, width: 0.12 μm). (b) Zoomed-in image of the "parallelogram" Andreev interferometer.

All these three thermometers (shown in Fig. 4.1(a)) have similar structure: a short normal metal wire with four superconducting probes. These superconducting probes are designed to be close to each other to increase the Josephson coupling between them, but not close enough to cause a supercurrent flow in the entire thermometer, as this would effectively short the resistance of the normal metal wire, and defeat its use as a thermometer. Additionally, a superconductor is a very poor thermal conductor at temperatures well below T_c. Hence, as supported by numerical simulations, the use of the superconductor can ensure a uniform temperature distribution along the thermometer and eliminate the heat leak from the sample through the probes of the thermometer. Using this type of thermometer, one would not disturb the electron temperature profile of the sample we measured. Furthermore, it also needs to be pointed out that since the thermometers were patterned in the same step of lithography as other parts of the device, good coupling between the thermometers and the electron bath of the sample is automatically ensured.

As with other resistance thermometers, our thermometer is also a secondary thermometer, which needs to be calibrated before using it. The calibration procedure is as follows [**101, 102**]: (1) First of all, we use the conventional four-probe technique to measure the resistance of the thermometer as a function of the temperature of the dilution refrigerator mixing chamber, with no dc current through the heater[2]. The temperature of the dilution refrigerator is determined by a RuO_2 thermometer mounted on the mixing chamber. This temperature dependence is plotted in Fig. 4.2(a) for all three thermometers shown in Fig. 4.1(a). The normal state resistance R_n of these three thermometers are 4.08 Ω ("Hot"), 4.19 Ω ("Cold") and 5.28 Ω ("Sub")

[2]Although there is no dc current, we still attach the current source to the heater (but set the output to zero), in order to keep the same wire configuration during the entire calibration procedure.

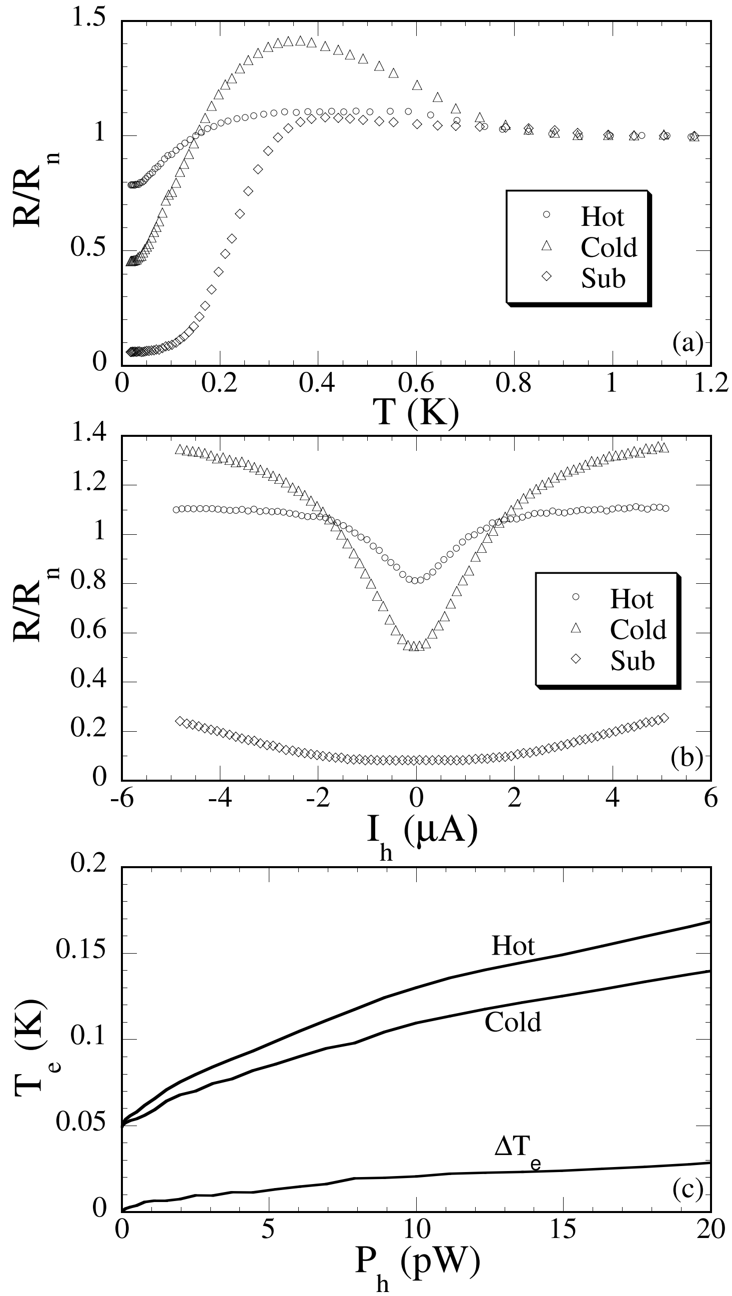

Figure 4.2. (a) Normalized resistance of the "Hot", "Cold" and "Sub" thermometers as a function of the temperature. (b) Normalized resistance of the three thermometers as a function of the dc current through the heater at the substrate temperature $T_b = 49.5$ mK. (c) Local electron temperature T_e of the "Hot" and "Cold" thermometers and the corresponding temperature gradient ΔT_e across the sample as a function of heater power P_h at the substrate temperature $T_b = 49.5$ mK.

respectively. (2) In the next step, we fix the temperature of the dilution refrigerator and measure the resistance of these three thermometers as a function of the dc current I_h through the heater (shown in Fig. 4.2(b)). (3) We then numerically cross-correlate the data in Figs. 4.2(a) and 4.2(b), to obtain the local electron temperature T_e as a function of I_h. To be specific, we first replot the temperature dependence of the thermometer resistance (Fig. 4.2(a)) in a form of T *vs.* R, and the heater current dependence (Fig. 4.2(b)) as I_h *vs.* R. We then generate a series of R with equal spacing and interpolate it into the T *vs.* R curve and the I_h *vs.* R curve, to obtain the corresponding T and I_h, and plot them as T_e *vs.* I_h, here we use T_e instead of T to denote the temperature of electrons. The resulting T_e for the "Hot" and "Cold" thermometers and the corresponding temperature differential ΔT_e are shown in Fig. 4.2(c), expressed as a function of the power of the heater P_h=$I_h^2 R_h$. Figure 4.2(c) shows that a significant fraction of the power generated in the heater flows through the sample, because T_e in both thermometers increases substantially when we increase the heater power, while the electron temperature differential ΔT_e increases only gradually.

The working regime of the thermometers is the low temperature regime[3], extending from the base temperature of the dilution refrigerator up to temperatures of 300-350 mK. As illustrated in Fig. 4.2(a), all three thermometers show strong temperature dependence in this regime. The changes are 32%, 96% and 102% for the "Hot", "Cold" and "Sub" thermometers respectively, much larger than can be expected from the decrease of resistance due to the proximity effect ($\sim$ 10% for transparent NS interfaces). We interpret this strong resistance change as associated with

[3]This range can easily be increased by using a superconductor with a higher T_c, or modifying the distance between the superconducting probes as discussed below.

Josephson coupling between the pairs of superconducting probes on either end of the thermometers [**106, 107**] (*i.e.*, between I_+ and V_+ or I_- and V_-). Due to this coupling, the resistance of those parts of the thermometers near the superconducting probes drops significantly, but the entire thermometer does not go superconducting, since the distance between superconducting probes on opposite ends of thermometer is too large for significant Josephson coupling to occur between them in our measurement temperature range. Since the temperature range where Josephson coupling in a SNS junction is determined by the correlation energy $E_c = \hbar D/L^2$, where D is the electronic diffusion coefficient in the normal metal, and L the distance between the two NS interfaces [**6**], the above picture can easily be checked: Taking, as an example, the "Cold" thermometer, with the measured value of $D = 104$ cm^2/sec, and $L = 0.485$ μm between the nearest pair of probes (I_+ and V_+), the temperature below which Josephson coupling should become significant is $E_c/k_B \simeq 336$ mK, which is in good agreement with the experimentally observed value of ~ 350 mK where the resistance starts to drop rapidly (see Fig. 4.2(a)). We also note that, if we take $L = 1.15$ μm the distance between the superconducting probes on opposite sides of the thermometer (I_+ and I_-), we get $E_c/k_B \simeq 60$ mK. Below this temperature, the Josephson coupling between the superconducting probes would be appreciable and the supercurrent in between would increase exponentially. Eventually, the resistance of the thermometer would vanish because the supercurrent would short the entire thermometer. However, at the base temperature 20 mK of the dilution refrigerator, we still observed non-zero resistance for all three thermometers. This may indicate that, in spite of our best efforts to shield all sources of extrinsic noise, there may still be some noise coupled to the sample, which suppresses the supercurrent across the thermometers.

In addition, the resistance of the thermometers is strongly dependent on the ac excitation current used in the four-probe resistance measurements, which is another signature of the presence of Josephson coupling. Again, we use the "Cold" thermometer as an example. Figure 4.3(a) demonstrates the temperature dependent resistance $R/R_n(T)$ of the "Cold" thermometer taken with different values of the ac excitation current. As the ac excitation current is increased from 10 nA to 200 nA, the overall change in resistance from the base temperature to approximately 350 mK reduces substantially. Since there is essentially no difference between the 20 nA curve and the 10 nA curve, we assume 20 nA current would neither suppress the supercurrent nor create any self-heating problem.

The third signature of the presence of Josephson coupling is that the differential resistance dV/dI of the thermometers as a function of the dc current I through it is strongly reminiscent of the differential resistance of a SNS junction, except that the differential resistance at $I = 0$ is not zero. Figure 4.3(b) shows the current-voltage $(I - V)$ curve of the "Cold" thermometer, obtained by integrating the dV/dI vs. I curve after the $I = 0$ value of the differential resistance was subtracted. The overall shape of this $I - V$ curve is very much like the $I - V$ characteristic for a SNS junction. Extrapolation of the high current part of the curve gives a *critical current* of $I_c \simeq 40$ nA.

We also notice that, in the temperature regime from ~ 350 mK up to T_c, the resistance of all the thermometers *increases* as the temperature decreases below T_c. Although this behavior is opposite to the result of proximity effect, similar behavior

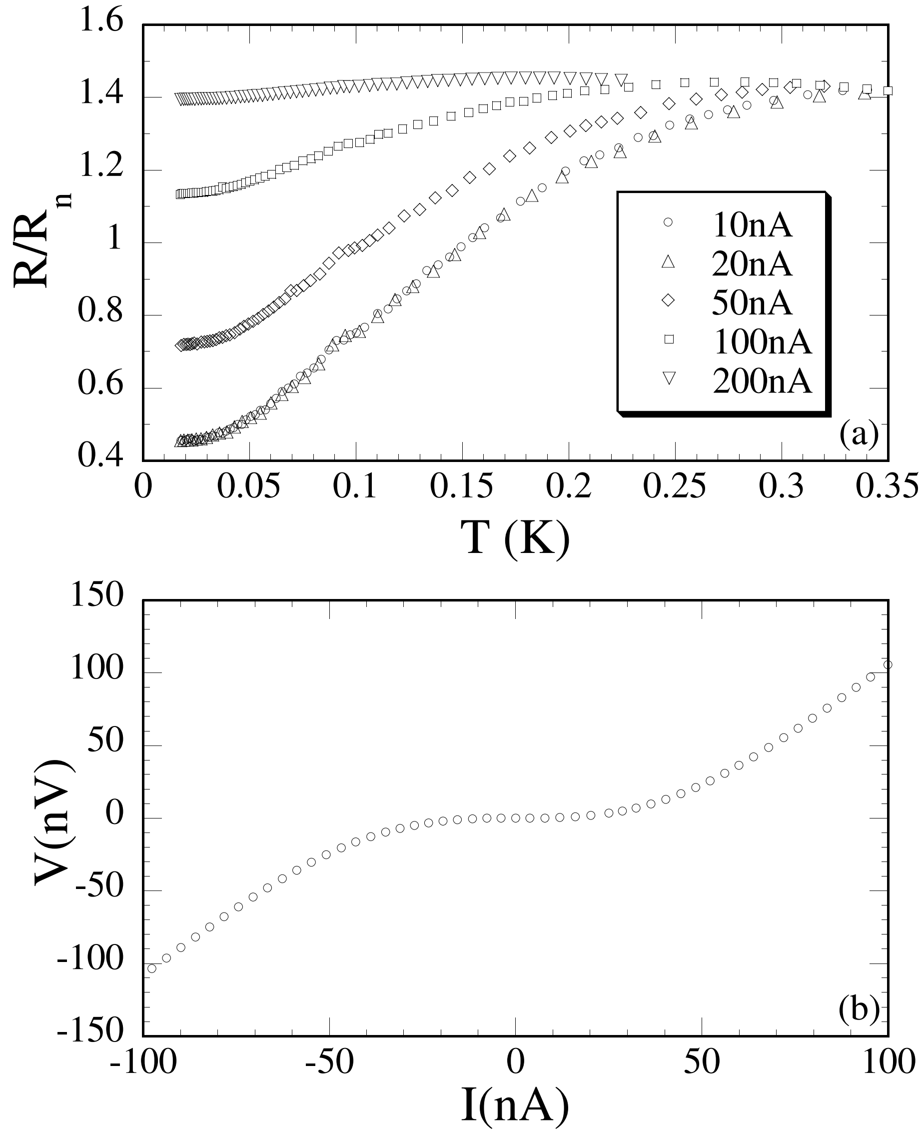

Figure 4.3. Characteristics of the "Cold" thermometer: (a) Normalized resistance of the "Cold" thermometer as a function of the temperature taken with different values of the ac excitation current. (b) $I-V$ curve of the "Cold" thermometer at the substrate temperature $T_b = 17.6$ mK, obtained by integrating the dV/dI vs. I curve after the $I = 0$ value of the differential resistance was subtracted.

has also been observed before in proximity-coupled devices [**5, 108, 109, 110**], and was interpreted as arising from current redistribution in samples with a four-probe configuration, where the width of the sample is of the same order as its length, as the sample is cooled below T_c. Our thermometers can also work in this temperature regime, but with less sensitivity compared with the low temperature regime.

Furthermore, it also needs to be pointed out that the "Sub" thermometer resistance shown in Fig. 4.2(b) has a very weak dependence on I_h at low values of I_h. Particularly, as $I_h \leq 1$ μA, the "Sub" thermometer basically shows no responses, but the "Hot" thermometer reaches $T_h \sim 140$ mK at $I_h = 1$ μA ($T_b = 49.5$ mK). This behavior demonstrates that the heat leak (due to electron-phonon interactions) from the electron bath to the substrate is very small in the low temperature regime. Finally, note that this device was patterned onto an oxidized Si substrate. For the samples fabricated later on top of 50 nm thick Si_3N_4 membranes, we would expect the heat leak to be even less.

4.2. Thermal conductance of Andreev interferometers

The ability to measure small temperature differences in the electron temperature opens up the possibility of quantitatively measuring the thermal properties of mesoscopic samples. In this section, I will focus on the thermal conductance measurements of Andreev interferometers.

In the sample of Fig. 4.1, since we already know the temperature differential ΔT_e across the Andreev interferometer (see Fig. 4.2(c)), if we have a way of determining the heat current through it, we then can obtain its thermal conductance ($G^T = I^T/\Delta T_e$). In this sample configuration, the electrical connections from the heater line and thermometers extending out to the outside patterns are all designed to be superconducting. Since, at temperatures well below T_c, the thermal conductance of superconductor is very small, these superconducting connections essentially block the heat transport from the device to its surroundings. Hence, most of the power P_h generated in the heater flows out only through the Andreev interferometer. In addition, as noted in the previous section, the heat conduction due to phonons is also negligible at a temperature below 140 mK. The heat flow I^T through the Andreev interferometer can therefore be determined by simply measuring the resistance of the heater R_h and using $P_h = I_h^2 R_h$. The thermal conductance is then $G_T \equiv I^T/\Delta T_e = P_h/\Delta T_e$.

4.2.1. Earlier work in measuring the thermal conductance of Andreev interferometers

Thermal conductance measurements on Andreev interferometers were first performed by Dikin *et al.* in our group at the base temperature of the ^{3}He refrigerator ($T_b = 280$ mK) [**13**]. The configuration of the Andreev interferometer measured there is similar to the one shown in Fig. 4.1, except that it has two short superconducting arms in the path of the thermal current. Figure 4.4 represents the main results of Dikin's measurement. First, Fig. 4.4(a) shows the local electron temperature (T_h and T_c) measured by the "Hot" and "Cold" thermometers and the corresponding temperature differential $\Delta T_e = T_h - T_c$ as a function of the heater power P at $T_b = 280$ mK. Compared with Fig. 4.2(c), we note that the "Cold" thermometer in this device initially has no response with a small heater power ($P < 3$ pW), which suggests that the heat flow may be interrupted in the low heater power regime.

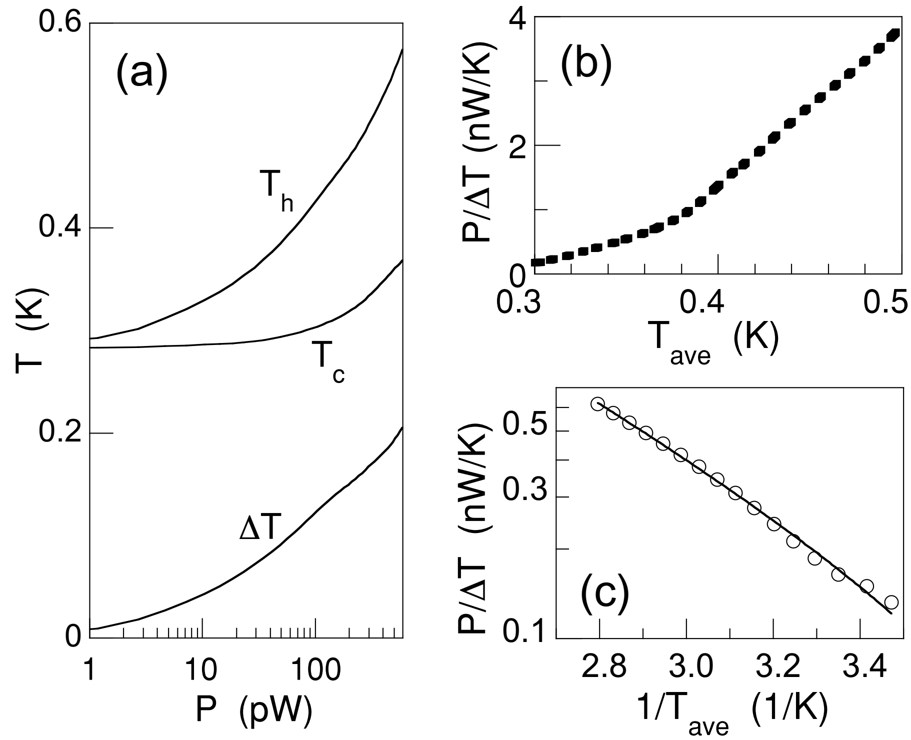

Figure 4.4. (a) Local electron temperature measured by the "Hot" and "Cold" thermometers and the corresponding temperature differential ΔT as a function of the heater power P at $T_b = 280$ mK. (b) G^T as a function of the average temperature $T_{ave} = (T_h + T_c)/2$ of the Andreev interferometer. (c) Open dots replot the low-power regime of (b) in a semilogarithmic scale as a function of $1/T_{ave}$. Solid line is a fit to the expected dependence for a superconductor. (Adapted from Ref. [**13**].)

Second, the thermal conductance G^T as a function of the average temperature $T_{ave} = (T_h + T_c)/2$ of the Andreev interferometer is plotted in Fig. 4.4(b). One can read out $G^T = 1.2 \times 10^{-10}$ W/K in the limit of $\Delta T_e = 0$ at $T_b = 280$ mK. It is instructive to calculate G^T of an equivalent normal metal system[4] by using the Wiedemann-Franz law [**11**], $G^T = \pounds_0 T/R$, where $\pounds_0 = \pi^2/3e^2$ is the Lorenz number. Thus, we get $G^T = 1.3 \times 10^{-9}$ W/K, which is more than an order of magnitude higher than the experimental result. As pointed out by Dikin *et al.* in Ref. [**13**], although small deviations from the Wiedemann-Franz law at this temperature are expected, the order of magnitude difference is unusual, which indicates that the presence of the two superconductor arms in the path of the thermal current has a substantial effect on G^T.

Third, motivated by the above discussions, Dikin *et al.* treat the portion of the normal metal underneath the NS interfaces as superconductor, and replot the low-power regime of Fig. 4.4(b) but as a function of $1/T_{ave}$ (see Fig. 4.4(c)). They then fit the data to the formula for thermal conductance of a superconductor [**66**]

$$G_S^T \approx G_S^T \frac{6}{\pi^2} \left(\frac{\Delta}{k_B T} \right)^2 e^{-\Delta/k_B T}, \tag{4.2}$$

where G_N^T is the thermal conductance in the normal state. The fitting is reasonably close to the real data and gives us a superconducting gap $\Delta = 200$ μeV, which is comparable with the value $\Delta = 183$ μeV obtained from the measured T_c of the Al.

Consequently, based upon the above three aspects of the data, we can conclude that the measured suppression of G^T in Ref. [**13**] is due to the well-known suppression of thermal conductance in a superconductor. Furthermore, in Ref. [**14**], Bezuglyi

[4]An Au wire of the same dimensions as in the Andreev interferometer, but without the Al loop.

and Vinokur calculate G^T of a NSN sandwich-like structure, similar to the sample measured by Dikin. Their simulations indeed show that a large suppression in G^T is expected at higher temperatures due to the presence of the superconductor.

4.2.2. Quantitative measurements of the thermal resistance of Andreev interferometers in the true proximity regime

Prompted by Dikin's experiment, we quantitatively measured the temperature and magnetic field dependence of the thermal resistance R^T of the "house" and " parallelogram" Andreev interferometers in the true proximity regime. Note that, in this section, we will use the phrase *thermal resistance* ($R^T = 1/G^T$) instead of *thermal conductance* in order to have a better presentation of the data and easier connection with the results of the electrical resistance measurements.

4.2.2.1. Technical improvements

Compared with Dikin's work, a couple of substantial modifications and technical improvements have been done in our measurements. They are

(1) Design the samples in the true proximity regime. Since we believe that the large suppression in G^T in Dikin's measurement is due to the superconducting effect resulting from the two superconducting arms patterned in the path of the thermal current, we have moved the NS interfaces away from the thermal path in our new devices. The SEM image of the "parallelogram" Andreev interferometer has been shown in Fig. 4.1; the "house" interferometer is illustrated in Fig. 4.5.

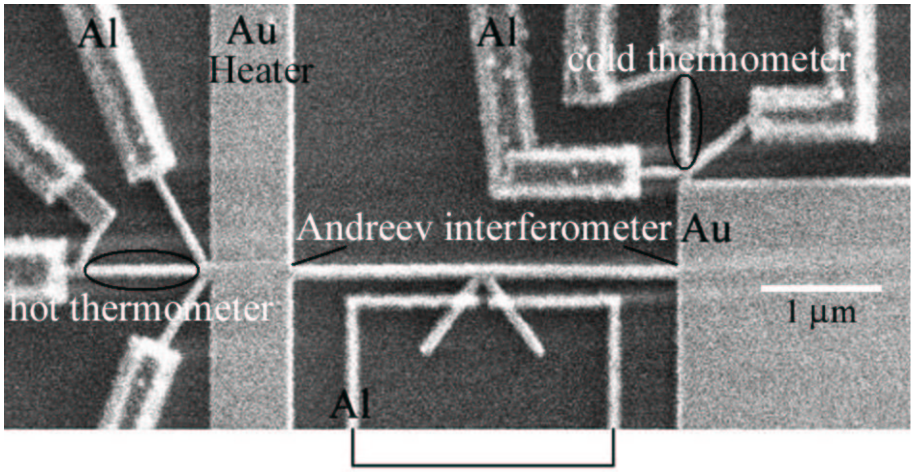

Figure 4.5. SEM image of the "house" Andreev interferometer. The device consists of three parts: (1) On the left, a metallic heater line with a thermometer. (2) On the right, a large normal-metal pad with another thermometer. (3) In the middle, a "house" Andreev interferometer.

(2) Eliminate the heat leak from the electron bath to the substrate. As discussed previously that the electron-phonon scattering is not negligible at a temperature above 200 mK [**102**]. In the present work, we measured R^T at lower temperatures, from 20 mK to 170 mK. In addition, our later samples are fabricated on top of 50 nm thick Si_3N_4 membranes to minimize the heat leak from the device to the substrate. Furthermore, R^T is measured with much lower thermal current through the sample, which is as low as 2.1 fW compared in the present work with 455 fW in Ref. [**13**].

(3) Improve NS interface transparency. Since the magnitude of the proximity effect strongly depends on the transparency of the NS interfaces, special care has been taken in the sample fabrication process to reduce the NS interface resistance. For samples patterned onto oxidized silicon substrates, *in situ* Ar^+ plasma etching is performed to clean the normal-metal surfaces prior to

deposition of the superconductor. A specific interface resistance of 1.4-1.6 mΩ μm^2 has been obtained. For samples fabricated on top of Si_3N_4 membranes, however, since charge accumulation could blow out the structures on the chip, we use external O_2 plasma etching and achieve a specific interface resistance of ~ 17 mΩ μm^2.

4.2.2.2. Temperature dependent thermal resistance of Andreev interferometers

In the above discussions, we have already described the way we measure the thermal resistance R^T of Andreev interferometer as a function of the heater power P_h, but only at a fixed temperature of the refrigerator. In this section, we will repeat this measurement at different temperatures to obtain the temperature dependence of R^T.

Figures 4.6(a) and 4.6(b) show the thermal resistance R^T of the "parallelogram" and "house" interferometers as a function of the heater power P_h at six different temperatures of the dilution refrigerator. As shown in Fig. 4.6, the qualitative behavior of R^T as a function of P_h is similar for the two configurations. In addition, for both geometries, we find that R^T is a strongly non-linear function of P_h at small values of P_h. Experimentally speaking, to define the thermal resistance in the linear response regime, R^T should approach a limiting value as $P_h \to 0$. However, it is not the case in our experiments, in which R^T continues to change as a function of P_h even at a heater power of a few femtowatts. In particular, as shown in Fig. 4.7, $R^T \propto \sqrt{1/P_h}$ at low values of P_h. This power law dependence of R^T on P_h is found to hold for all samples and at all temperatures measured. It is also consistent with our numerical simulations for these devices based on the quasiclassical theory (see

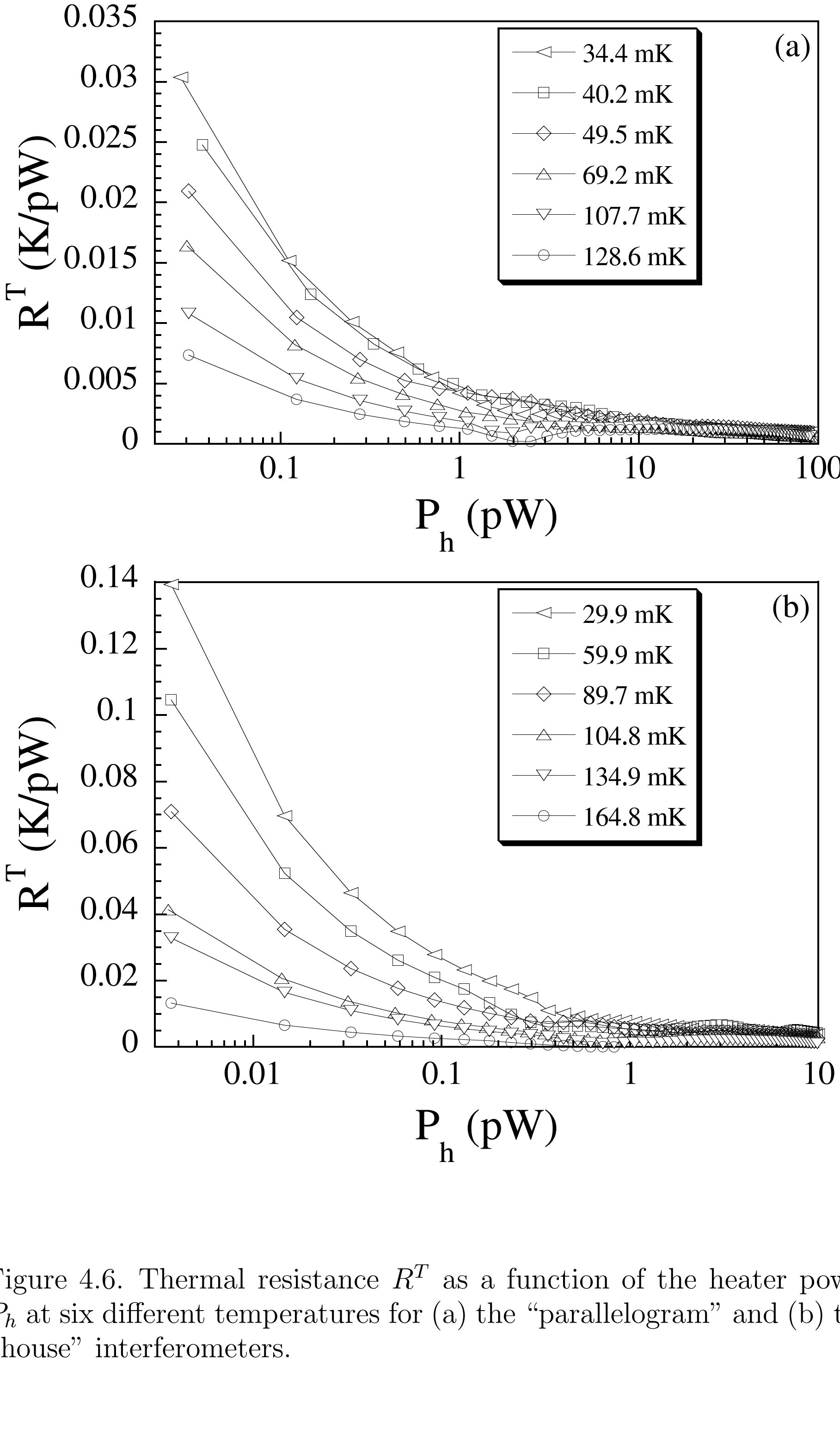

Figure 4.6. Thermal resistance R^T as a function of the heater power P_h at six different temperatures for (a) the "parallelogram" and (b) the "house" interferometers.

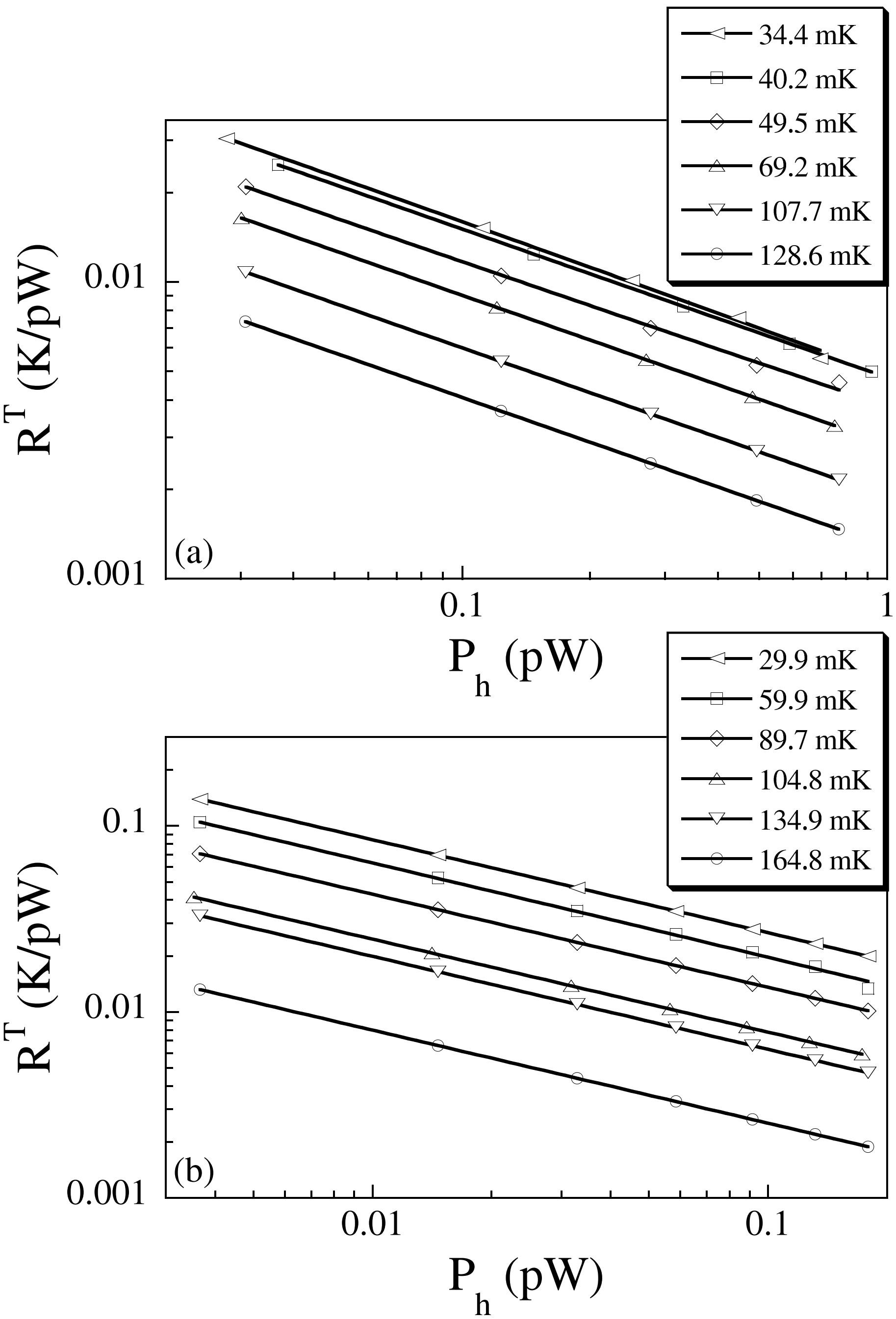

Figure 4.7. R^T *vs.* P_h at small values of P_h at six different temperatures for (a) the "parallelogram" and (b) the "house" interferometers. The solid lines are fits to the functional form $R^T \propto \sqrt{1/P_h}$.

Fig. 2.8 in Chapter 2), but for intermediate values of P_h. Following the discussions in Chapter 2 and applying the experimental parameters (taking the "house" interferometer as an example, $T_c = 1.2$ K and $R_N^T = 0.01$ K/pW from Fig. 4.6(b)), we find that the theory predicts the linear response regime is approached only for $P_h < 3$ fW, comparable to the lowest power we applied in the heater. Note that 3 fW is one order less than the lowest power we applied for the "parallelogram" interferometer.

Theoretically, of course, a linear response R^T always can be defined. However, the non-linear dependence of R^T as a function of P_h curve in our measurements creates a problem in experimentally defining the thermal resistance of the sample. Given this problem, in the later discussion, we define the linear response thermal resistance as the value of R^T at the lowest heater power measured. This corresponds to $P_h = 31$ fW for the "parallelogram" interferometer and $P_h = 3.7$ fW for the "house" interferometer of Fig. 4.6 respectively. The resulting thermal resistance as a function of the temperature for the two geometries is demonstrated in Fig. 4.8 (represented by solid symbols). At first sight, one may notice that the thermal resistance R^T of the "house" interferometer is about 4 times larger than that of the "parallelogram" interferometer at low temperatures. However, it must be pointed out that R^T of the "parallelogram" interferometer was inferred at a heater power of 31 fW, compared with 3.7 fW for the "house" interferometer. If we extrapolate R^T of the "parallelogram" geometry to a value of 3.7 fW, we would get the same order of magnitude of R^T for both geometries.

In Fig. 4.8, except for the experimental results, we also show the expected thermal resistance of equivalent normal-metal wires (solid lines), calculated by using the Wiedemann-Franz law from the measured normal state resistance of the wires

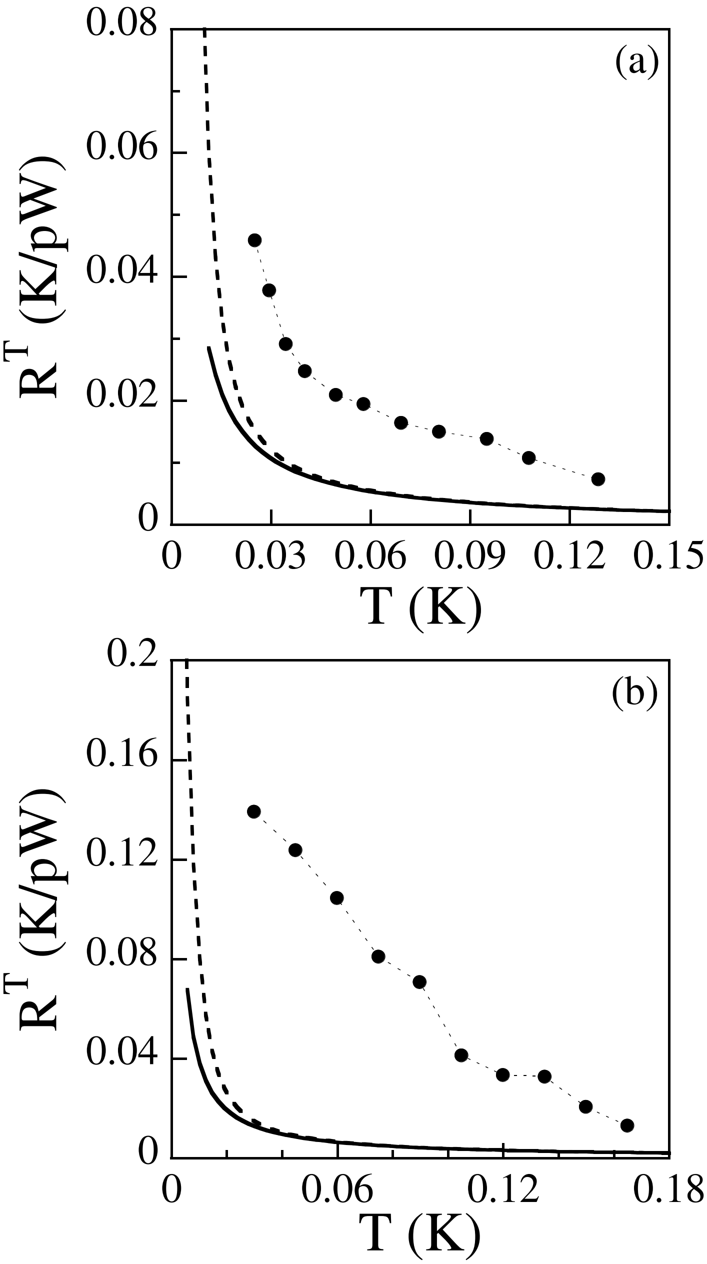

Figure 4.8. Thermal resistance (solid symbols) as a function of the temperature for (a) the "parallelogram" and (b) the "house" interferometers. The dotted lines are guides to the eye. The solid lines represent the thermal resistance of equivalent normal-metal wires, estimated using the Wiedemann-Franz law, and the measured normal state electrical resistance of the wires. The dashed lines represent theoretical calculations of the thermal resistance of the interferometers, using the experimental parameters for the samples.

and the textbook value for the Lorenz number. We find that for both geometries, R^T increases rapidly with decreasing temperature. For the “house” interferometer, R^T is larger than the thermal resistance of an equivalent normal system by almost an order of magnitude at the lowest temperature $T \sim 30$ mK.

In addition, we calculate the thermal resistance of the Andreev interferometers numerically as a function of the temperature, using the experimental parameters for the samples. For the “house” interferometer, the distances from either side of the sample and from the NS interfaces to the center node are (referring to Figs. 2.4(a) and 4.5) $L = 1.55$ μm and $L' = 0.29$ μm respectively. For the “parallelogram” configuration, $L = 1.19$ μm, $L' = 0.24$ μm, and $L” = 0.76$ μm (see Figs. 2.4(b) and 4.1). As predicted in Chapter 2, the thermal resistance of Andreev interferometers increases monotonically as the temperature decreases below T_c, due to a decrease in the DOS $N(E)$ near the Fermi energy E_F. However, unlike a superconductor, $N(E)$ of an Andreev interferometer does not go to zero as $T \to 0$, but saturates at a value that depends on the dimensions of the sample and the transparency of the NS interfaces. As $T \to 0$, $N(E)$ is small but finite; the quasiparticles occupying the levels in the pseudogap contribute to the thermal resistance, leading to an enhanced thermal resistance, but one that still varies inversely with T according to the Wiedemann-Franz law. From our numerical simulations (see Fig. 2.7), we notice that R^T/R^T_N starts to deviate from its normal state value at a temperature of $T \sim 5E_c/k_B$ and approaches its saturation value below a temperature corresponding to approximately $0.1E_c/k_B$, where $E_c = \hbar D/L_0^2$ is the correlation energy and L_0 is the length from one end of the interferometer to one of the NS interfaces. For the “parallelogram” interferometer shown in Fig. 4.1, where the diffusion constant $D = 127$ cm^2/sec and $L_0 = 1.43\ \mu$m, we get $5E_c/k_B \sim 235$ mK and $0.1E_c/k_B \sim 4.7$ mK. Equivalent parameters for the "house" interferometer are $D = 208$ cm^2/sec and $L_0 = 1.84\ \mu$m, coincidently giving similar temperatures of $5E_c/k_B \sim 235$ mK and $0.1E_c/k_B \sim 4.7$ mK. Notice that this saturation temperature is below the temperature range of the experiments. The dashed lines in Fig. 4.8 show the calculated thermal resistance as a function of the temperature for the "parallelogram" and "house" interferometers respectively, with the parameters given above, and assuming perfectly transparent NS interfaces. However, the theoretical predictions show significant deviations from the normal state thermal resistance (calculated by using the Wiedemann-Franz law) only at temperatures below 20-30 mK, while the experimental R^T is already larger than the normal state thermal resistance at temperatures about an order of magnitude higher. Although we should not be surprised by this deviation, since the fits to the temperature dependent electrical resistance by the quasiclassical theory are not very successful either, we believe that this deviation might be associated with an intrinsic mesoscopic effect not restricted to NS devices. In particular, it might be related to the long length scales required to equilibrate the energy of the quasiparticles in mesoscopic devices.

4.2.2.3. Phase dependent thermal resistance oscillations

As we know, the quasiparticles are phase coherent near the NS interfaces during the process of Andreev reflection. Therefore, like the electrical resistance, the thermal resistance of an Andreev interferometer is expected to oscillate periodically as a function of the external magnetic flux, with a fundamental period of one superconducting flux quantum $\Phi_0 = h/2e$ [**14, 16**]. Detailed simulations in Chapter 2 for both the "parallelogram" and the "house" interferometers show that the "house" geometry actually has a larger oscillation amplitude of the thermal resistance compared with the "parallelogram" configuration, hence we focus on the former geometry in measuring oscillations of R^T. However, it turns out that measuring the phase dependent thermal resistance oscillations is a difficult proposition. Ideally, to achieve our goal, we can apply a temperature differential across the interferometer and measure the variations in the temperature by the local electron thermometers as a function of the external magnetic field. In reality, however, this method does not work in our experiments. The reason can be understood by closely looking at the exact numbers in Fig. 4.6(b). As shown in Fig. 4.6(b), at a heater power of 3.7 fW, the temperature differential across the sample is $\Delta T = T_h - T_c \sim 0.52$ mK. However, to resolve such a small temperature change $\delta(\Delta T)(B)$, one would require an impractically long averaging time. Of course, to increase $\delta(\Delta T)(B)$, one could apply a larger amount of power to the heater, because $\Delta T \propto \sqrt{P_h}$ at low heater powers. But, the maximum variation in R^T would drop dramatically at larger values of P_h. Consequently, in order to measure the variation of R^T with respect to the external magnetic field B, we use the same technique as for the temperature dependence: First, we fix the external magnetic field B and measure the thermal resistance R^T as a function of heater power P_h. We then take the value at the lowest measured heater power as the value of R^T at that value of magnetic field B. Second, we bias the magnetic field to another value and repeat the above measurements. The resulting R^T *vs.* B curve is shown in Fig. 4.9 for a third Andreev interferometer device in the "house" configuration, where R^T is measured at $T = 40$ mK and $P_h = 2.1$ fW. For comparison, we also plot oscillations of the resistance of the interferometer measured at $T = 400$ mK. The reason we choose this relatively high temperature is that at low temperatures, the R *vs.* T curve shows hysteretic behavior with respect to magnetic field, due to the diamagnetic screening of the supercurrent [**111, 112**]. At higher temperatures, the supercurrent is suppressed, therefore the hysteresis disappears. For field dependent thermal resistance measurements (at low temperatures), we first sweep the magnetic field to ~ 3 G, and then slowly decrease it to the desired value and fix it. After setting up the field, we typically wait about 20-40 minutes, and then we start to calibrate the thermometers and measure R^T as a function of P_h, which would take about 5 hours. Hence, we should not expect any hysteresis in our results. From Fig. 4.9, one can see that both the electrical resistance R and the thermal resistance R^T oscillates periodically with the applied magnetic field B, with a period corresponding to one superconducting flux quantum $\Phi_0 = h/2e = 0.092$ mT through the interferometer loop. In addition, both oscillations have the same symmetry with respect to B. Since it is well-known that R is symmetric with respect to B, R^T is also symmetric with respect to B, as predicted by theory [**14, 16**]. The offset seen in the data is due to the remanent field in the external superconducting solenoid. Furthermore, we notice that there is a π phase difference between these two oscillations. It is exactly what one expects, because lower resistance means larger proximity effect (or more suppression in the DOS, $N(E)$), resulting an enhancement in R^T.

4.3. Symmetry of phase-coherent thermopower oscillations in Andreev interferometers

Using the local thermometry technique, we also have been able to quantitatively measure the thermopower of Andreev interferometers. As defined earlier, the

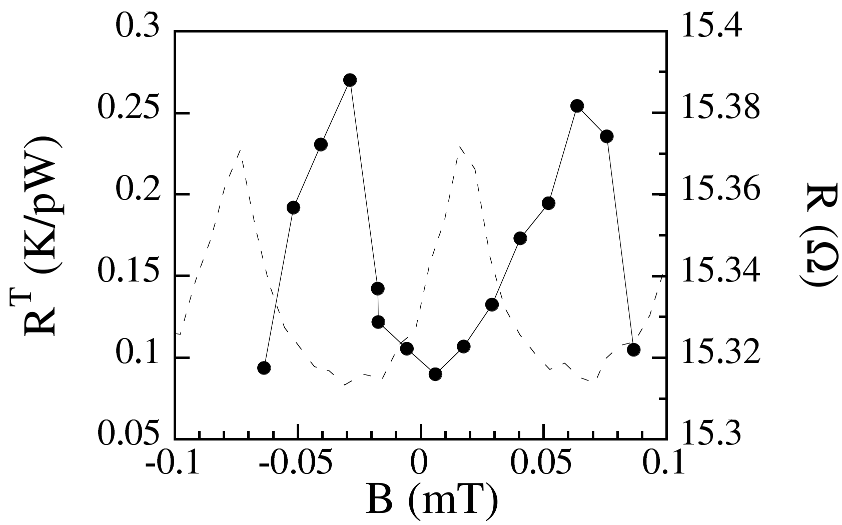

Figure 4.9. Thermal resistance oscillations of a "house" interferometer (solid symbols) as a function of the externally applied magnetic field, measured at $T = 40$ mK. The solid line is a guide to the eye. The dashed line is the resistance oscillations of the same sample as a function of the magnetic field at $T = 400$ mK.

thermopower is essentially the ratio of the thermal voltage V_{th} to the temperature differential ΔT across the sample, under the condition that there is no electrical current through the sample. Figure 4.10 shows the schematic of a device for measuring the thermopower of a "parallelogram" interferometer, where the lighter area is normal metal (Au) and the darker area is superconductor (Al). Again, by passing a dc current through the heater, a temperature differential ΔT is generated across the interferometer. The local electron temperature of each side of the sample is then measured by the 'Hot' and 'Cold' thermometers, and the difference between them gives ΔT. As to the thermal voltage V_{th}, ideally, it should be measured by two probes which are at the same temperature to avoid the thermopower contribution from the probes. Hence, as shown in Fig. 4.10, an extra reference Au wire has been designed,

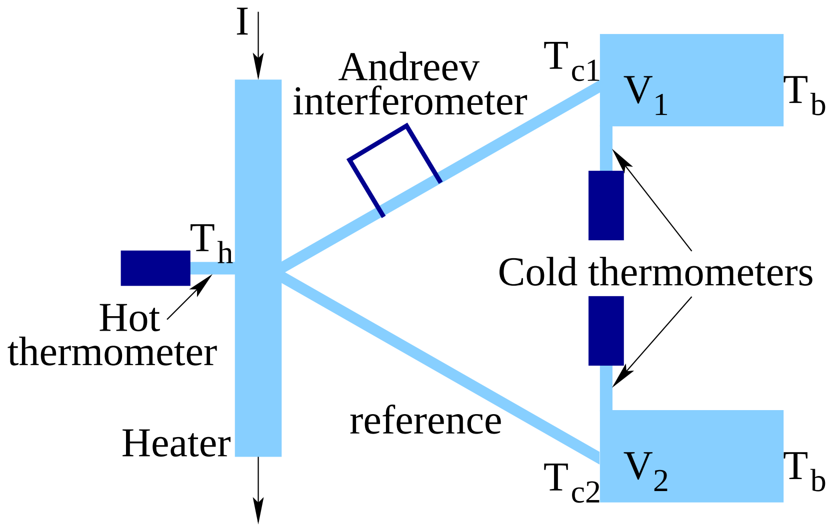

Figure 4.10. Schematic of a device for measuring the thermopower of a "parallelogram" Andreev interferometer, where the lighter area is normal metal and the darker area is superconductor. During the measurements, the local electron temperatures at the hot side (T_h) and the cold side (T_c) of the sample are measured by local electron thermometers. The thermal voltage is measured using the probes labeled V_1 and V_2, which are at the same temperature T_b, the substrate temperature.

and V_{th} is given by

$$V_{th} = V_2 - V_1 = \int_{T_{c1}(I)}^{T_h(I)} S_A dT + \int_{T_h(I)}^{T_{c2}(I)} S_N dT, \tag{4.3}$$

where S_A and S_N are the thermopower of the Andreev interferometer and the reference arm respectively.

As we mentioned in previous chapters, experimentally, the thermopower of Andreev interferometers has been found to be a periodic function with respect to the magnetic flux with a period corresponding to one superconducting flux quantum $\Phi_0 = h/2e$ through the loop of interferometer [**17, 18, 19**]. The most puzzling aspect of the experimental results on Andreev interferometers is that the symmetry of the thermopower oscillations with respect to the external magnetic field can be either symmetric or antisymmetric, depending on the geometry of the sample. In this thesis work, the symmetry issue of the thermopower oscillations has been further studied, focusing on the relation between the symmetry of the oscillations to the supercurrent distribution in the device. Before we introduce our new experimental results, let us first summarize the discoveries in the previous work.

4.3.1. Previous work

The symmetry of the thermopower oscillations in Andreev interferometers can be summarized in Fig. 4.11, which is adapted from Ref. [**17**]. Figure 4.11(a) illustrates the thermopower (solid line) and the resistance (dashed line) oscillations as a function of magnetic field for the "house" Andreev interferometer; while Fig. 4.11(b) is for the "parallelogram" configuration. For both sample geometries, the resistance oscillates symmetrically with respect to the applied magnetic field. However, while the thermopower oscillations for the "house" thermometer are symmetric with respect to magnetic field, the oscillations for the "parallelogram" interferometer are antisymmetric with respect to magnetic field. Since these initial experiments, our group has measured a number of different sample topologies. All of these sample topologies, except the "house" topology, show a thermopower that is antisymmetric with respect to magnetic field. In spite of considerable theoretical efforts in recent several years [**20, 21, 22**], this dependence of the symmetry of the thermopower oscillations on the topology of the sample still remains an open and interesting question. The theoretical studies suggest that the origin of the symmetry of the thermopower oscillations may be associated with the conversion of the supercurrent to the quasiparticle current in the devices.

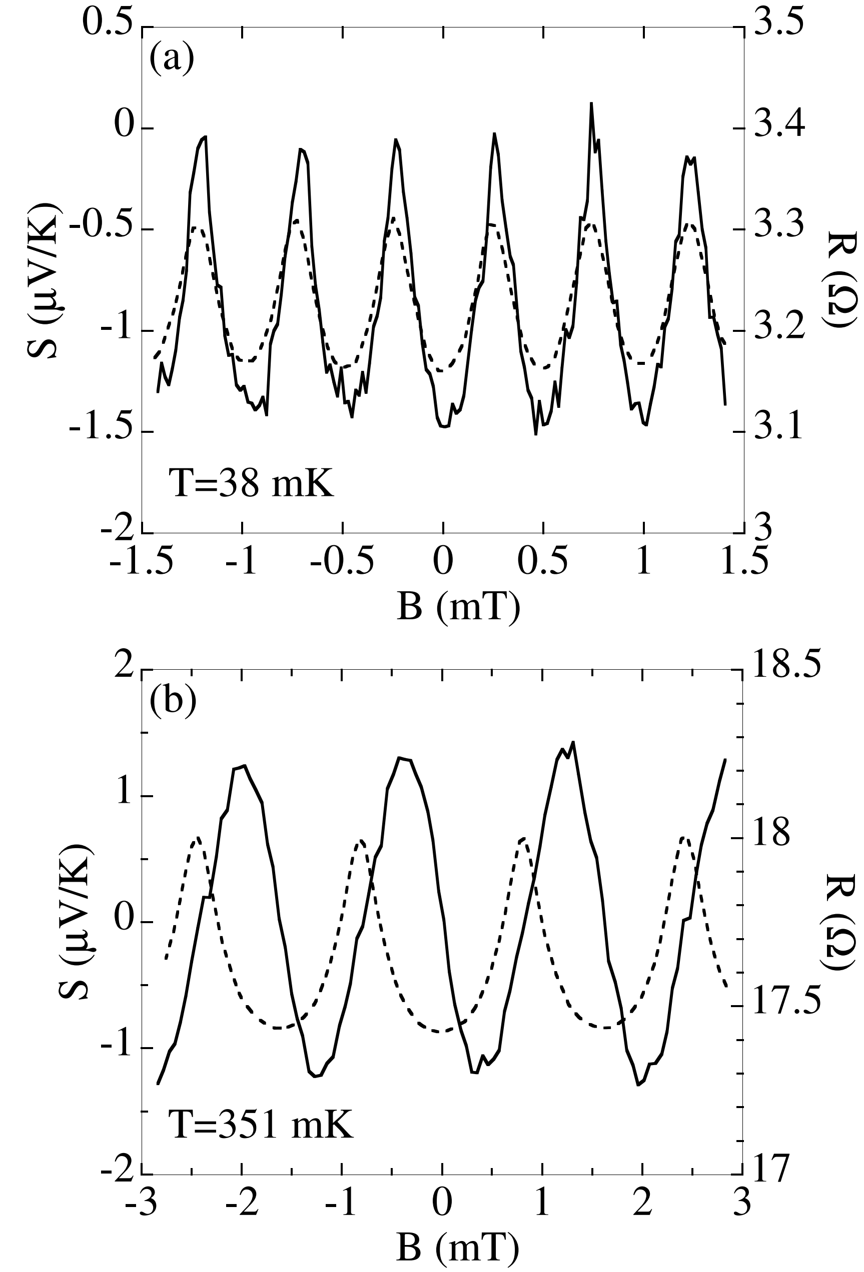

Figure 4.11. (a) Symmetric thermopower oscillations (solid line) as a function of magnetic field for the "house" Andreev interferometer; (b) Antisymmetric thermopower oscillations (solid line) as a function of magnetic field for the "parallelogram" Andreev interferometer. In both (a) and (b), the dashed line represents the resistance oscillations as a function of magnetic field, which is always symmetric. (Adapted from Ref. [**17**].)

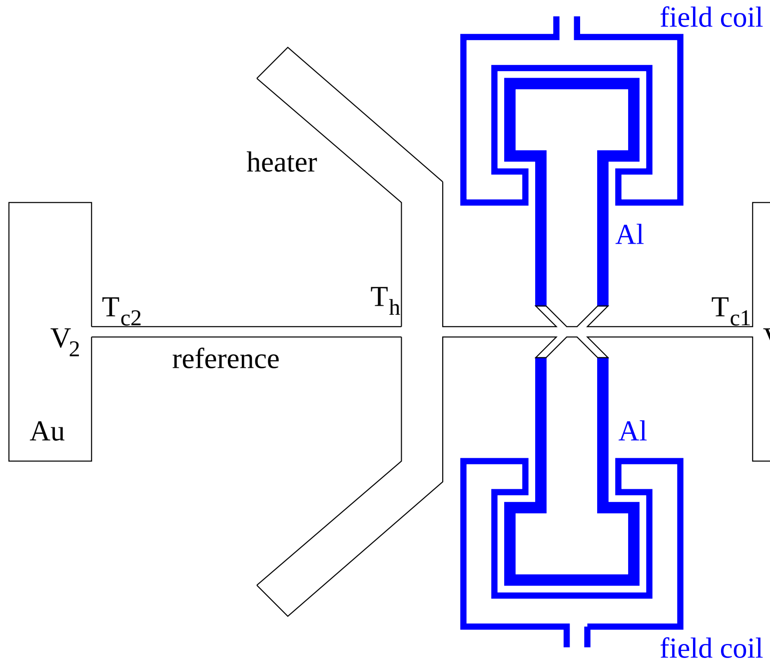

Figure 4.12. Schematic of the double-loop interferometer.

4.3.2. Thermopower measurements in a double-loop interferometer

In order to investigate the relation between the thermopower and the supercurrent in Andreev interferometers, a double-loop interferometer has been designed so that we can control the supercurrent distribution in the device. The schematic of the device is shown in Fig. 4.12 and its SEM image has been shown in Fig. 3.8 in Chapter 3. In Fig. 4.12, a double-loop interferometer is shown schematically to the right of the heater, which is a metallic Au film of ~ 25 μm long and ~ 1 μm wide in reality. The interferometer consists of an 8.5 μm long and 100 nm wide Au wire, which is connected to the heater on one end, and a large area Au contact on the other end. The thickness of the Au film is 50 nm. The Au wire is connected above and below to two superconducting Al loops (100 nm thick). Around each interferometer loop, a superconducting Al thin film field coil was fabricated. Magnetic flux could be generated and coupled into each interferometer loop by sending a dc current into its field coil. Since the two field coils were separated by a distance of more than 30 μm, the cross-coupling between them is then negligible[5]. Although the magnetic field generated by each field coil is not homogeneous across the area of the nearby interferometer loop, we are still able to tune the direction and the magnitude of the magnetic flux locally and separately in each loop. By varying the direction of the dc current in the field coils, the flux coupled to both loops could be varied in phase, *i.e.*, they are perpendicular to the plane of the substrate, and in the same direction; or out of phase, *i.e.*, they are perpendicular to the plane of the substrate, but in opposite directions. To the left of the heater, a reference Au wire with the same dimensions as the one in the interferometer was patterned. The thermal voltage V_{th} is then measured between V_2 and V_1. From low temperature (300 mK) measurements, the resistivity of the Au film was estimated to be $\rho_{Au} \sim 1.5\ \mu\Omega$cm, corresponding to a diffusion constant of $D_{Au} \sim 264$ cm^2/s. In order to ensure transparent NS interfaces, an *in situ* Ar^+ plasma etching was used to clean the Au surface before the Al deposition. The transparency of the Au/Al interfaces was checked by an on-chip control sample, which had a resistance of 0.14 Ω for a 0.01 μm^2 area at room temperature.

In this experiment, since we only focus on the symmetry of the thermopower oscillations with respect to the magnetic flux, but not the exact values of the thermopower, we do not measure the electron temperatures using local electron thermometers, as we have done in previous experiments. In Eqn. (4.3), because S_N is small and does not vary as a function of the magnetic flux, we can neglect its

[5]Calculation shows that when we apply one superconducting flux quantum Φ_0 through one of the interferometer loops by its field coil, only 0.1% Φ_0 is generated in the opposite interferometer loop.

contribution in our analysis. Hence, Eqn. (4.3) can be rewritten as

$$V_{th} = \int_{T_{c1}(I)}^{T_h(I)} S_A dT. \tag{4.4}$$

In order to improve the measurement sensitivity, a non-local ac technique has been used by applying an ac tickling current into the heater, and measuring the derivative [**17, 13**]

$$\frac{dV_{th}}{dI} = S_A \left(\frac{dT_h(I)}{dI} - \frac{dT_{c1}(I)}{dI} \right), \tag{4.5}$$

in the linear response regime. As discussed in Chapter 3, in order to pick up the signal dV_{th}/dI in the measurements, a floating current source is required and the grounding point should be in the center of the heater, close to the joint of the heater to the interferometer. Unfortunately, we do not have a lead in this device for such a ground. Alternatively, we use the second derivative technique developed in Ref. [**18**], and measure

$$\begin{aligned} \left.\frac{d^2V_{th}}{dI^2}\right|_{I=0} &= S_A \left.\left(\frac{d^2T_h(I)}{dI^2} - \frac{d^2T_{c1}(I)}{dI^2} \right)\right|_{I=0} \\ &\quad + \frac{dS_A}{dI} \left.\left(\frac{dT_h(I)}{dI} - \frac{dT_{c1}(I)}{dI} \right)\right|_{I=0} \\ &= S_A \left.\left(\frac{d^2T_h(I)}{dI^2} - \frac{d^2T_{c1}(I)}{dI^2} \right)\right|_{I=0}, \end{aligned} \tag{4.6}$$

where $dT_{h(c)}/dI = 0$ at $I = 0$. This method actually can further improve the measurement sensitivity. From the thermal conductance measurements, we know that $d^2T_{h(c)}/dI^2$ are always symmetric with respect to the magnetic flux, so that we can obtain the symmetry of the thermopower oscillations directly from the symmetry of the measured d^2V_{th}/dI^2.

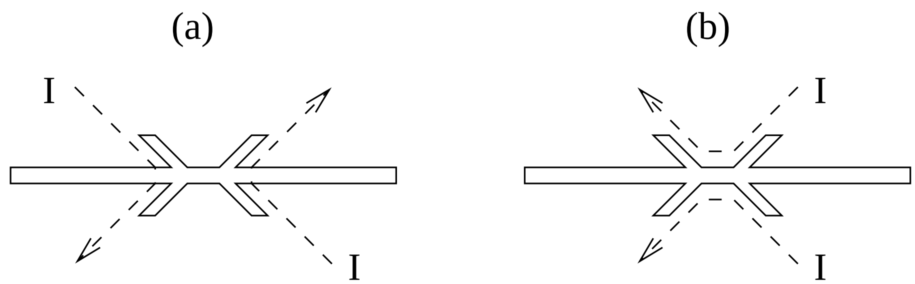

Figure 4.13. Preferred supercurrent distributions for (a) the in-phase flux configuration and (b) the out-of-phase flux configuration.

The technical details relate to the second derivative measurements have been described in Chapter 3. Particularly, in this experiment, an ac current I of rms amplitude 5 μA with a frequency of $f \sim 43$ Hz was sent into the heater, while d^2V_{th}/dI^2 is determined by measuring the ac voltage drop between V_2 and V_1 at a frequency of $2f$ and a phase of 90°.

The magnetic flux is applied locally by sending a dc current in series into the two field coils. As we have noted above, depending on the direction of the dc current, the fluxes coupled to the two interferometer loops can either be in phase, or out of phase. In the former case, assuming the device is perfectly symmetric, there will be no supercurrent along the path of the thermal current, as the supercurrent contributions from the two loops cancel each other, as shown in Fig. 4.13(a). The in-phase flux configuration is therefore similar to the "house" geometry, in which no supercurrent flows along the path of the thermal current. In the out-of-phase case (Fig. 4.13(b)), the two supercurrent contributions add, leading to a supercurrent that is twice the value for a single loop. Since the supercurrent flows along the path of the temperature gradient, this configuration is similar to the "parallelogram" configuration.

Figure 4.14 shows the thermopower (solid line) and the resistance (dashed line) oscillations of the double-loop interferometer as a function of the dc current through

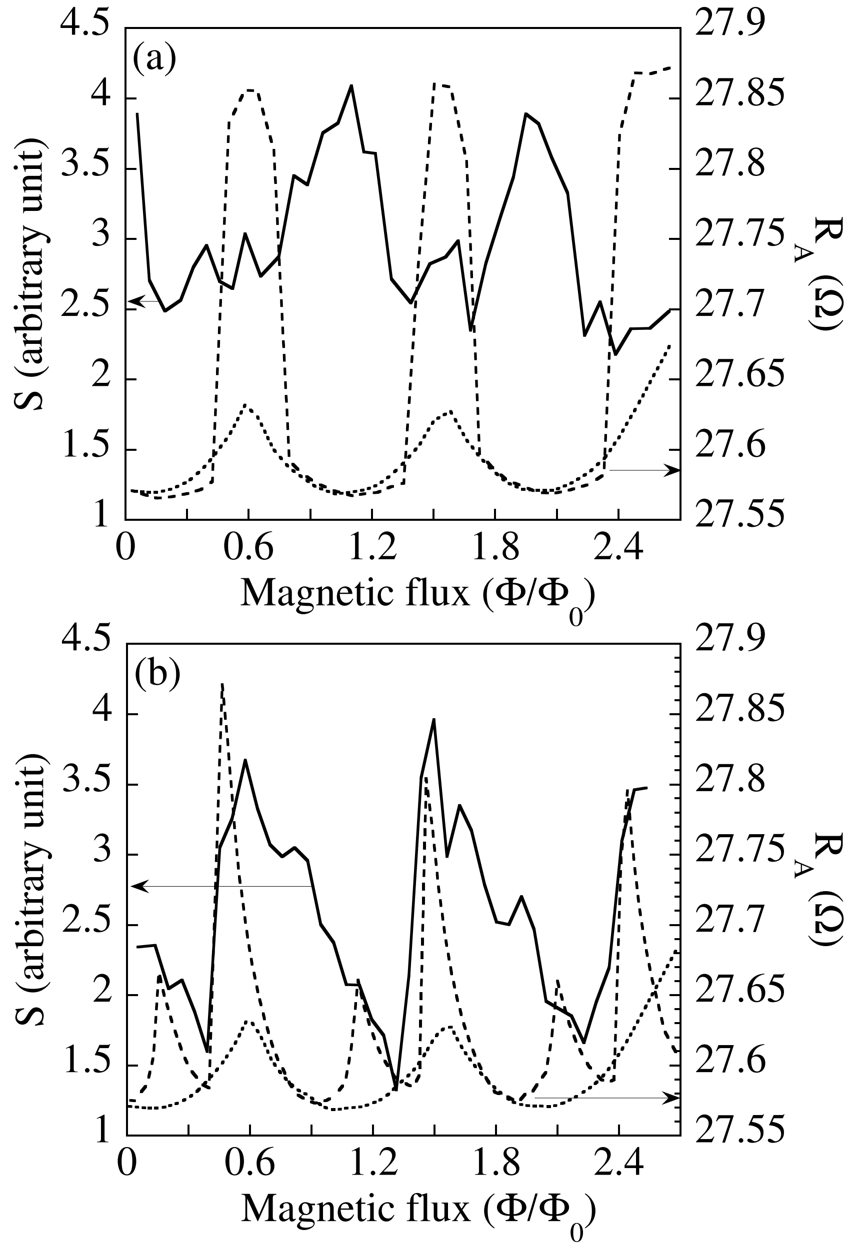

Figure 4.14. The thermopower (solid line) and the resistance (dashed line) oscillations as a function of the dc current through the field coils, calibrated in units of the number of flux quanta through one interferometer loop: (a) the in-phase flux configuration and (b) the out-of-phase flux configuration. The dotted lines in both (a) and (b) represent the resistance oscillations measured as sending a dc current through only one field coil. The thermopower is measured at $T = 0.79$ K; the resistance is measured at $T = 0.93$ K.

the field coils, calibrated in units of the number of flux quanta Φ_0 through one interferometer loop, for the in-phase flux configuration (Fig. 4.14(a)) and the out-of-phase flux configuration (Fig. 4.14(b)). We find that both the thermopower and the resistance oscillate with respect to the applied magnetic flux, but with different symmetry and waveform for the in-phase and out-of-phase flux configurations. In order to examine the exact symmetry of these oscillations, the resistance of the interferometer is measured as a function of the dc current through only one field coil, because it is always symmetric with respect to the magnetic flux. The resulting curves are shown as the dotted lines in Figs. 4.14(a) and 4.14(b). It should also be pointed out that there is a small offset in the magnetoresistance measurements, which is most likely due to the Earth's magnetic field, since the area of the interferometer loop is large. Knowing that the area of one interferometer loop in this device is $\sim 287\ \mu\mathrm{m}^2$, we estimate that $B = 7.2 \times 10^{-6}$ T corresponds to 1 superconducting flux quantum through the loop. For this sample, the amplitude of the resistance oscillations was only appreciable at higher temperatures, in the range of 0.75 to 1 K. It is consistent with the fact that the amplitude of the resistance oscillations shows reentrant behavior as a function of the temperature when the temperature is on the scale of the correlation temperature $E_c = \hbar D/L^2$ [**56, 62, 111**]. At a temperature scale on the order of $5E_c/k_B$, the amplitude of the oscillations reaches its maximum; otherwise, below or above this scale, the amplitude decreases. Taking $L = 500$ nm as the length between the NS interfaces in this device, $E_c/k_B \sim 0.8$ K, hence the amplitude of the resistance oscillations decrease with decreasing temperature below this temperature scale. For this reason, the magnetoresistance data shown in this paper were all taken at a temperature of 0.93 K.

The dashed curves in Figs. 4.14(a) and 4.14(b) show the resistance of the double-loop interferometer as a function of the dc current applied through both field coils, in the in-phase and out-of-phase flux configurations respectively. In both configurations, the resistance was found to be strongly hysteretic with magnetic flux. This is consistent with the fact that, when the Josephson coupling between NS interfaces is strong, the supercurrent screens the magnetic flux diamagnetically, so that the phase difference between the NS interfaces is not directly given by the applied magnetic flux [**111, 112**]. This effect depends on the self-inductance of the interferometer loop and the temperature of the device. At low temperatures, the circulating supercurrent becomes larger, therefore the hysteresis increases. Consequently, in Fig. 4.14, all the data are plotted in the same direction of the sweep. The most interesting feature of the resistance oscillations is in the out-of-phase flux configuration (Fig. 4.14(b)), where two periods can be discerned clearly. One period corresponds to the one observed with the field applied only through one field coil (and hence corresponds to one superconducting flux quantum through only one loop); the second one, which has smaller amplitude, has a period half of that, corresponding to one superconducting flux quantum through both loops. In the in-phase case, only oscillations with period corresponding to a flux through one loop are observed. At this point, we do not know the exact nature of this difference. However, if we believe the Earth's magnetic field is indeed the reason causing the offset in the magnetic flux, it might be the possible origin of this difference. In the in-phase case, the Earth's magnetic field would apply symmetrically to both interferometer loops. On the other hand, for the out-of-phase flux configuration, it would have the opposite effect in each loop, which may cause the doubled frequency in the magnetoresistance measurement.

The solid lines in Figs. 4.14(a) and 4.14(b) show the thermopower oscillations as a function of the magnetic flux for the in-phase (Fig. 4.14(a)) and out-of-phase (Fig. 4.14(b)) flux configurations. As with the electrical resistance, the amplitude of the thermopower oscillations decreased drastically at low temperatures, which implies that the reentrance behavior in the thermopower measurements [**17, 18**] also has an energy scale being set by E_c. Consequently, these thermopower data were taken at a temperature of 0.79 K. Although the amplitudes of the thermopower oscillations in the two configurations are approximately the same, the waveforms are quite different. In particular, the waveform of the out-of-phase flux configuration is quite non-sinusoidal. In addition, comparing the thermopower curve to the resistance curves, it can be seen that the thermopower oscillations in the in-phase flux configuration are symmetric with respect to the flux, while they are nearly antisymmetric in the out-of-phase case. As we pointed out earlier, the in-phase flux configuration is similar to the "house" interferometer, which also shows symmetric thermopower oscillations; the out-of-phase flux configuration is more close to the "parallelogram" interferometer, which shows an antisymmetric thermopower oscillations. Hence, the thermopower measurements in the double-loop interferometer are consistent with the previous results. At the end, it should be emphasized that these two symmetries of the thermopower oscillations were taken from the same device, merely by changing how the flux (and hence the supercurrents) are distributed in the sample. This is strong evidence that the symmetry of the thermopower is intimately related to whether or not supercurrent flows along the path of the thermal current, *i.e.*, related to the conversion of the supercurrent to the quasiparticle current.

CHAPTER 5

Spin transport in ferromagnet/superconductor heterostructures

During the last decade, ferromagnet/superconductor (FS) heterostructures have been found to exhibit a wide variety of interesting properties. However, from our point of view, this field is still much less explored compared with NS systems, and the experimental work in this field is much behind the theoretical studies, especially in diffusive systems where the experimental results so far are even contradictory. This field involves tremendous amount of interesting physics, and by itself cannot be fully covered in a thesis. Therefore, in this chapter, we are going to only touch a small portion of it and extend our understanding regard to the spin-polarized electron transport through FS interfaces and the superconducting proximity effect in ferromagnets.

5.1. Spin transport through FS interfaces

5.1.1. Differential resistance dV/dI of mesoscopic FS junctions

Recently, point contact Andreev reflection has become a common tool to quantitatively determine the spin polarization P in ferromagnets [**25, 26**]. As one of the most important fundamental parameters, the spin polarization is defined by $P \equiv (n_\uparrow - n_\downarrow)/(n_\uparrow + n_\downarrow)$, where $n_{\uparrow(\downarrow)}$ denote the densities of spin-up and spin-down electrons respectively. In order to understand these point contact Andreev reflection experiments, it would be very instructive to start from the NS case.

On a microscopic level, the low temperature transport properties of NS interface devices are related to the probability of Andreev reflection $A(E)$[1], which is essentially associated with the transparency of the NS interfaces. In the Blonder-Tinkham-Klapwijk (BTK) theory [**32**], the interface transparency is characterized by a dimensionless parameter Z: (1) When $Z = 0$, the NS interface is perfectly transparent and $A(E) = 1$. Therefore, as one would expect, the conductance of the NS interface increases by a factor of 2 from its normal state value for $E < \Delta$. (2) When $Z > 0$, both the interface transparency and the value of $A(E)$ are reduced, so that the conductance of the interface decreases as well. (3) When $Z \to \infty$, the interface approaches the tunneling barrier limit, where $A(E) = 0$ and the conductance of the interface vanishes.

If the normal metal is replaced by a ferromagnet in the above picture, $A(E)$ would be reduced even for a perfectly transparent interface, due to the fact that not all the quasiparticles of one spin orientation can find a partner with opposite spin orientation to form a Cooper pair in the superconductor side. Particularly, in the limit of $P = 1$ (100% spin polarization), $A(E) = 0$. In a typical point contact FS spectroscopic measurement, the differential conductance dI/dV of a point contact junction is first measured as a function of the applied voltage bias V. The measured dI/dV *vs.* V curve is then fitted by the spin-polarized version of the BTK model for obtaining quantitative estimates of P and Z.

In this section, we will introduce our measurements of low temperature differential resistance dV/dI of mesoscopic FS junctions. The samples we measured are simple FS crosses (one sample image is shown in Fig. 5.1), fabricated by two-step

[1]Here E is the energy of a quasiparticle incident on the NS interface.

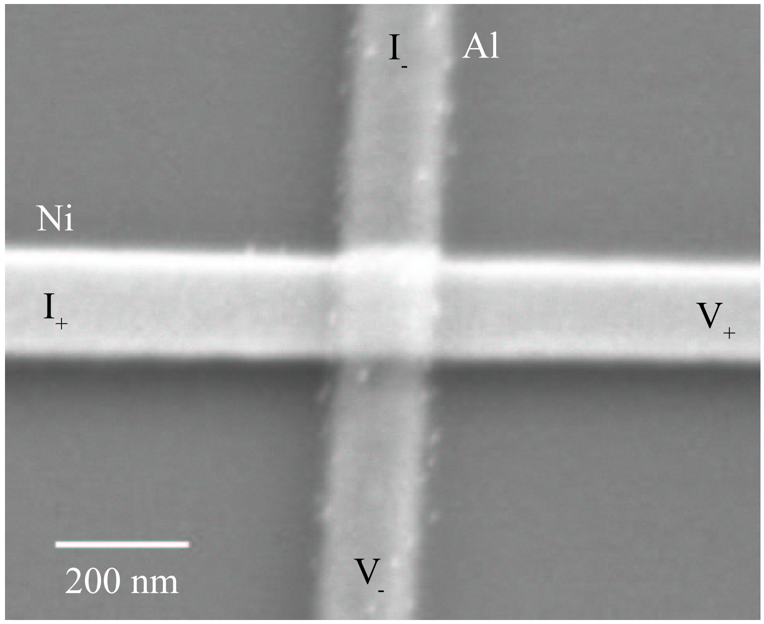

Figure 5.1. SEM image of a FS cross. The leads used to measure the four-terminal resistance are marked. The current leads were used to send both the ac and dc current. Both Ni and permalloy (NiFe) were used as the ferromagnet in our samples; only one sample image is shown here.

e-beam lithography onto oxidized silicon substrates, with all the interfaces cleaned by an *in situ* ac Ar^+ plasma etching prior to deposition of the Al films to ensure highly transparent interfaces. In the experiments, we measured the dV/dI of the FS interfaces as a function of the voltage bias V across them. As shown in Fig. 5.1, we use a four-terminal configuration, and send a small ($\sim 10 - 50$ nA) ac current superposed on a dc bias current. The voltage bias across the interface is obtained by numerically integrating the dV/dI vs. I curve afterward. The measurements were performed at the base temperature of ^{3}He refrigerator ($T = 290$ mK) with conventional ac lock-in amplifier techniques. During the measurements, we were able to apply a magnetic field in the plane of the sample, aligned along the length of the ferromagnetic wire.

The reasons for this kind of magnetic field setup are the following: first, this orientation increases the critical field of the thin film superconductor by reducing the cross-sectional area of the superconducting wire in the field; and second, the field is aligned along the easy axis of the ferromagnet element to obtain relatively a uniform magnetization.

Figure 5.2 shows the dV/dI *vs.* V measurements of a permalloy/Al (Py/Al) cross[2] at three different values of magnetic field H. There are a few features which are particularly interesting in these measurements. (1) As $H = 0$ (Fig. 5.2(a)), when we increase the voltage bias from $|V| = 0$ to either direction, the measured dV/dI first increases and reaches a peak at a voltage of $|V| \simeq 4$ μV; then it starts to decrease and show two dips before approaching its normal state resistance at higher values of V. Comparing our experimental results with what are observed in the FS point contact experiments, we notice that they are substantially different. For example: in the point contact experiments, one would not see the multiple peak/dip structures, and dV/dI would decrease rather than increase as one shifts away from $|V| = 0$. In addition, as shown in Fig. 5.2(a), while the inner pair of dips in dV/dI are almost symmetric with each other, the outer pair of dips are asymmetric, in that the amplitude of the dips is different. (2) As an external magnetic field H is applied, although the height of the peak in dV/dI remains almost same, the features of the two dips change very differently. For the outer pair of dips, the left dip (at negative bias voltage $V < 0$), shows a splitting as a function of magnetic field (a hint of splitting at $H = 1002$ G and a clear splitting at $H = 2005$ G). Note that a negative bias voltage corresponds to ejecting electrons from the Py side into the Al. As to the inner pair of dips, there

[2]This sample is similar to the one shown in Fig. 5.1, except that we use Py instead of Ni.

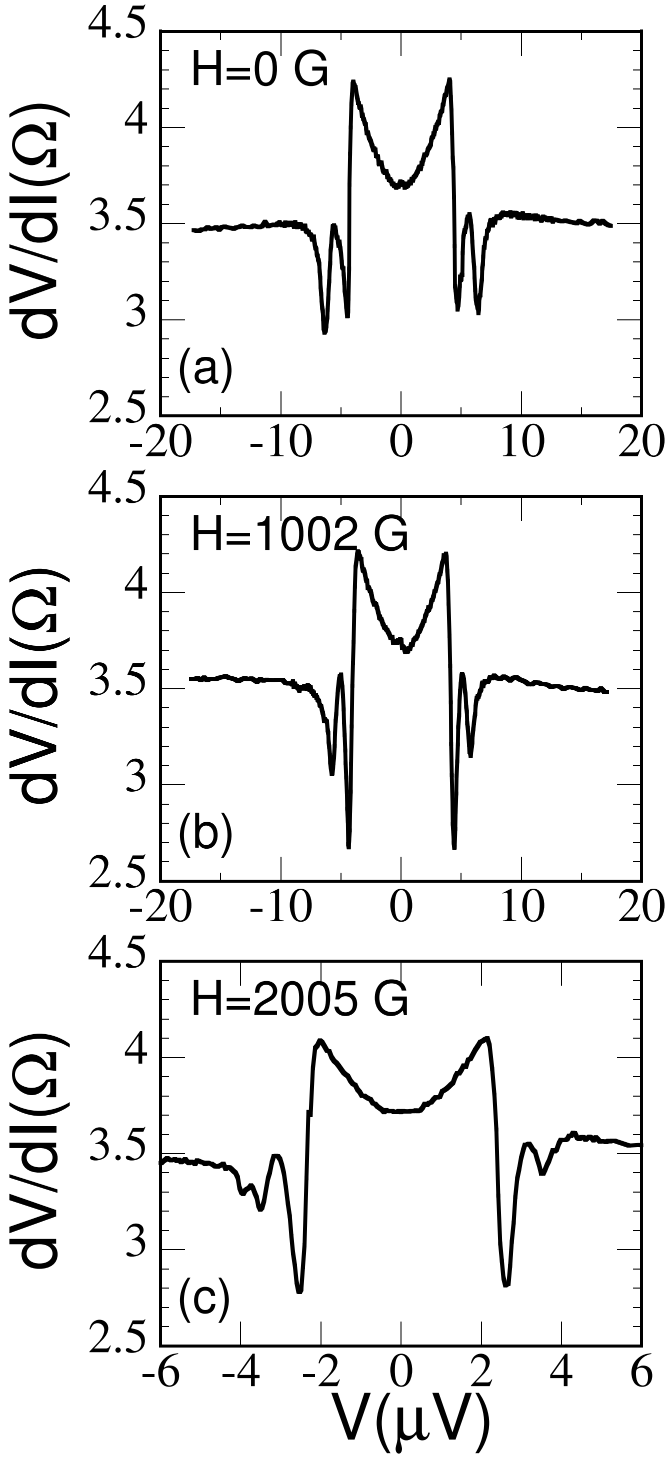

Figure 5.2. Differential resistance dV/dI of a Py/Al cross at $T = 290$ mK: (a) $H = 0$ G, (b) $H = 1002$ G, and (c) $H = 2005$ G.

is no sign of splitting. However, we also notice that the inner dips at $H = 1002$ G are much sharper than those at $H = 0$ G; and the inner dips at $H = 2005$ G are only a little bit less sharper, which may be simply due to the suppression of the superconducting gap at this field. One common theme of these peaks/dips is, as H increases, the positions of the peaks/dips move down to lower values of $|V|$. (3) The peak and dip features in the dV/dI measurements are all in the range[3] of $|V| < 10$ μV at $H = 0$ G instead of ~ 200 μV, the superconducting gap of Al obtained from the low temperature transport measurements.

In order to understand the above experimental results, we have studied the charge/spin transport across FS junctions in the framework of a spin-polarized BTK model [**25, 27**]. Again, we start from the NS case, *i.e.*, the conventional BTK model, where the properties ($I - V$ characteristics, etc.) of NS point contacts are studied by solving the Bogoliubov-de Gennes equations of the transmission and reflection of quasiparticles at the interfaces[4] [**32**]. In this thesis, however, we would not present the detailed derivation of the theory, just use the equation of the current I_{NS} across a NS junction with a voltage bias of V as the starting point. In the conventional BTK model, this current is given by

$$I_{NS} = 2N(0)ev_F S \int_{-\infty}^{\infty} [f(E - eV) - f(E)] \, [1 + A(E) - B(E)] \, dE, \tag{5.1}$$

where $N(0)$ is the density of states at the Fermi energy, v_F is the Fermi velocity of the electrons, S is the cross-sectional area of the interface, f is the Fermi distribution

[3]This range is sensitive to the thickness of the Al film and the area of the FS interface.
[4]Note that the BTK theory has proved to be valid for an interface with arbitrary barrier strength ranging from the metallic limit to the tunnel junction.

function, and $A(E)$ and $B(E)$ are the BTK coefficients that correspond to the probability for Andreev reflection and normal reflection of electrons from the NS interface. As we mentioned before, the value of $A(E)$ and $B(E)$ vary as a function of the BTK parameter Z. The exact expressions of $A(E)$ and $B(E)$ as a function of Z are listed in Table II of Ref. [**32**].

To adapt the BTK theory for FS systems, it is necessary to understand the differences between a NS and a FS structure in the process of Andreev reflection, whereby a spin-up electron of energy E combines with another spin-down electron of energy $-E$ to form a Cooper pair in the superconductor. Unlike the NS case, not all electrons which are incident on the FS interface can find complementary electrons of opposite spin polarity to form a Cooper pair in a FS device with a finite polarization P in ferromagnet, which results in a decrease in the probability of Andreev reflection by a factor of (1-P). Hence, in the FS case, we decompose the current into two parts $I = (1-P)I_u + PI_p$, where I_u is the unpolarized component of the current described by the conventional BTK theory, and I_p the polarized component of the current which are forbidden in the process of Andreev reflection. Correspondingly, the original BTK coefficients $A(E)$ and $B(E)$ can also be divided into an unpolarized component (A_u, B_u) and a polarized component (A_p, B_p) with $A_p = 0$. Note that these modifications on A and B are restricted by the requirement of current conservation through the FS interface, and the exact expressions of A_u, B_u and B_p are listed in Table I of Ref.

[**27**]. Eqn. (5.1) can then be modified to

$$
\begin{aligned}
I_{FS} = N(0)ev_F S \int_{-\infty}^{\infty} & [f(E-eV) - f(E)] \\
& \big\{(1-P)\left[1 + A_u(E - g\mu H) - B_u(E - g\mu H)\right. \\
& \qquad \left. +1 + A_u(E + g\mu H) - B_u(E + g\mu H)\right] \\
& \quad +P\left[1 - B_p(E - g\mu H)\right]\big\} dE,
\end{aligned}
\tag{5.2}
$$

where the energy contributions $\pm g\mu H$ come from Zeeman splitting of the superconducting quasiparticle density of states in the magnetic field. To be specific, in the presence of magnetic field, the energy of quasiparticles with one spin polarity is raised to $E + g\mu H$, while the energy of quasiparticles with opposite spin polarity is reduced to $E - g\mu H$. For the quasiparticles with lower energy $E - g\mu H$, they can always find a complementary partner with opposite spin, therefore they contribute to the unpolarized component of the current I_u for which Andreev reflection is allowed. For the quasiparticles with higher energy $E + g\mu H$, however, since Andreev reflection is unfavorable, they are related to the polarized component of the current I_p.

Based on Eqn. (5.2), we calculate the normalized differential resistance of a FS interface as a function of the voltage bias across it for a number of different combinations of Z and P. Figure 5.3(a) shows the results of our calculations without external magnetic field $H = 0$. For $Z = 0$ and $P = 0$, as we expected, we obtain exactly the same result as the conventional BTK model, in that the zero bias resistance of the interface is half of the normal state value. For $Z = 0$ and $P = 0.5$, only half of the electrons can find a partner to form Cooper pairs, therefore the zero bias resistance is the same as the normal state resistance. For $Z = 0.5$ and $P = 0$, we find

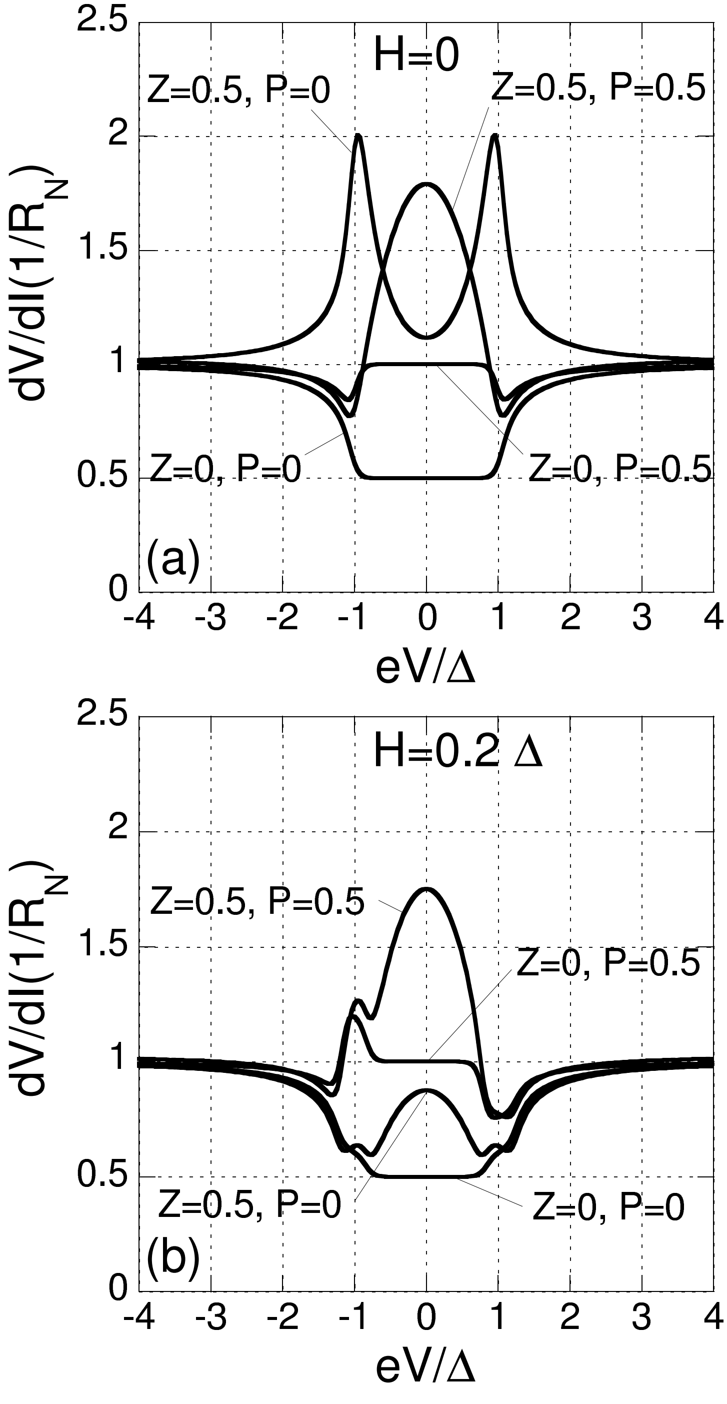

Figure 5.3. Numerical calculations of the normalized differential resistance of a FS interface as a function of the voltage bias across it, from the theory described in the text. (a) $H = 0$, (b) $H = 0.2\Delta$. The values for Z and P are noted in the figure, and the temperature is $T = 0.05\Delta$.

that the zero bias resistance is slightly larger than the normal state resistance. This behavior is associated with the suppression of Andreev reflection due to a non-perfect interface. For $Z = 0.5$ and $P = 0.5$, the zero bias resistance rises well above the normal state value. In short, our calculations basically show that the zero bias resistance is sensitive to both Z and P, so that one cannot differentiate the contributions from them independently by examining only the zero bias resistance. In order to obtain both Z and P, the entire measured dV/dI *vs.* V curve needs to be fitted to Eqn. (5.2), because Fig. 5.3(a) also show that Z and P affect the measured dV/dI in different ways at higher bias. Figure 5.3(b) shows the results of our calculations with an applied magnetic field $H = 0.2\Delta$. We notice that, except for the curve $Z = 0$ and $P = 0$, other curves are significantly different from those at $H = 0$. The differences are associated with the Zeeman splitting of the superconducting quasiparticle density of states. In particular, we observe a splitting in the dip structures of dV/dI with a substantial asymmetry near $V \simeq \Delta/e$. The splitting can be seen even for the curves of $P = 0$, but the asymmetry of the splitting only appears for $P \neq 0$.

Comparing the experimental results (Fig. 5.2) with the calculations (Fig. 5.3), we note that there are some similarities, but substantial differences in even the qualitative behavior. In the following, we will discuss the major differences between them.

First, Fig. 5.3(b) indicates that, when we apply an external magnetic field, the calculated differential resistance always decreases as the voltage bias is moved from 0, except for the case $Z = 0$. However, the experimental data show an opposite trend, *i.e.*, the resistance invariably *increases* and forms a peak structure as one increases the voltage bias across the interface (see Figs. 5.2(b) and 5.2(c), even in Fig. 5.2(a)). In addition, this resistance peak is also confirmed in the temperature

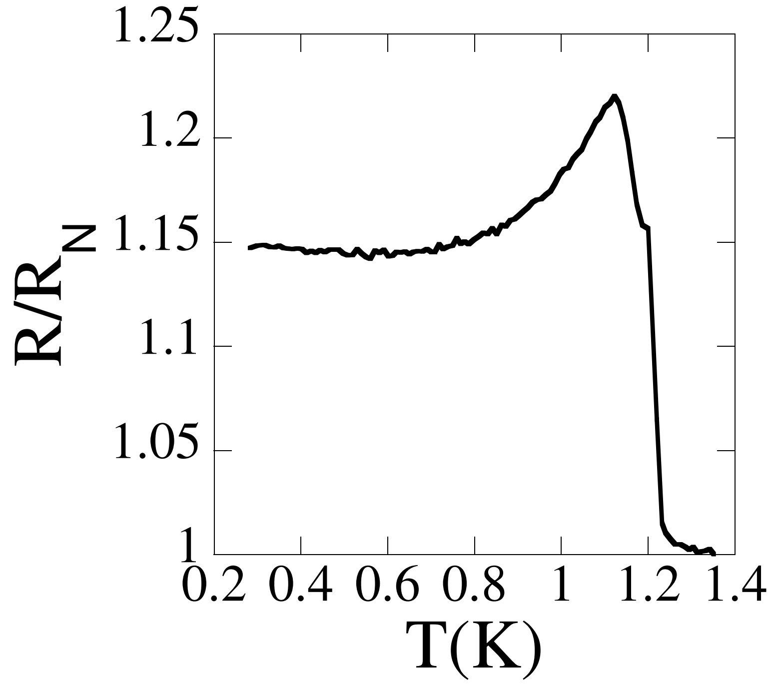

Figure 5.4. Normalized differential resistance of the Py/Al cross (the same sample of Fig. 5.2) as a function of temperature.

dependent zero bias resistance measurement of the same sample, which is shown in Fig. 5.4, where a large increase in resistance is seen at a temperature just below the transition temperature of the superconductor (Al). This behavior can be understood as the charge imbalance effect induced in the superconductor near the interface. We will come back and discuss it in detail for FS structures in the next section.

Second, in Fig. 5.2(a), two sharp dips appear in the data. We now understand that the outer pair of dips are related to similar dips seen in Fig. 5.3, because they are asymmetric and split in an external magnetic field. In particular, the evolution of the outer pair of dips as a function of the applied magnetic field in the experiments is very close to the case $Z = 0.5$ and $P = 0.5$ in Fig. 5.3, since both show a dip splitting at a negative voltage bias in an external magnetic field. However, different from the calculated results, we observe asymmetric dips even at zero applied external field in the experiments. However, we should also point out that the field H can result from a combination of the externally applied field and the self-field of the ferromagnet, which can be substantial near the ferromagnet. Hence, the asymmetric dips at $H = 0$ may be due to the self-field of the ferromagnet. As for the inner pair of dips observed in the experiments, at present, we do not know the origin of them. They might be associated with the charge imbalance peaks in dV/dI.

Third, as mentioned above, theory predicts the dip features in the dV/dI *vs.* V measurements to appear at $V \approx \Delta/e$ (see Fig. 5.3). However, in the experiments (shown in Fig. 5.2(a)), the positions of the outer dips are only at $V \sim 6$ μV, much less than 200 μV the estimated superconducting gap for Al. We believe this contradiction arises from the suppression of the superconducting gap due the presence of the ferromagnet, *i.e.*, the inverse proximity effect.

5.1.2. Charge imbalance effect in FS structures

The two-fluid model of superconductivity has been shown to be extremely valuable in understanding many interesting phenomena of superconductivity, if one can separate the contribution of the quasiparticle current from that of the supercurrent. Following the same spirit, one can understand that when quasiparticles are injected into a superconductor, it is also very useful to distinguish the quasiparticle chemical potential μ_{qp} and the Cooper pair chemical potential μ_{cp}. Indeed, the relaxation length scale for μ_{qp} and μ_{cp} are different in a superconductor near the NS or FS interfaces. The charge imbalance then gives rise to the difference in μ_{qp} and μ_{cp} [**9, 50**]. Deep inside the superconductor, both potentials are the same; near the interface, however, μ_{cp} rises to its bulk value within a superconducting coherence length ξ_S of the interface, while

μ_{qp} relaxes to μ_{cp} over a much longer length scale. This length scale is the so-called charge imbalance length λ_{Q^*}, which can be many microns long in superconductors such as Al [**77, 113, 114**], compared with $\xi_S \sim 190$ nm in Al at low temperatures [**115**].

Charge imbalance effects have been studied extensively in the 1970s and 1980s [**116, 117, 118, 119, 120**]. In principle, the potentials μ_{qp} and μ_{cp} were detected near a NS interface by using a normal-metal voltage probe and a superconducting voltage probe respectively [**117, 118**]. In our devices, with the probe configuration as shown in Fig. 5.1, we essentially measured μ_{cp} instead of μ_{qp} because the V_- probe is superconducting. Hence, we observed a resistance peak in the R *vs.* T curve at a temperature just below T_c (as show in Fig. 5.4). It should also be pointed out that this behavior is not restricted to FS devices; similar peaks have been observed in NS devices as well [**121**]. In diffusive systems, $\lambda_{Q^*} = \sqrt{D\tau_{Q^*}}$, where τ_{Q^*} is the charge imbalance time. Near T_c, an expression for τ_{Q^*} was given by Schmid and Schön [**50**]

$$\tau_{Q^*} = \frac{4k_B T}{\pi\Delta(T,H)}\sqrt{\frac{\tau_{in}}{2\Gamma}}, \tag{5.3}$$

where $\Delta(T,H)$ is the temperature and magnetic field dependent superconducting gap, τ_{in} is the inelastic scattering time, and the factor Γ is given by

$$\Gamma = \frac{1}{\tau_s} + \frac{1}{2\tau_{in}}, \tag{5.4}$$

and τ_s gives the contribution from orbital pair breaking. Here we have neglected the spatial variation of the superconducting gap and pair breaking due to the supercurrent. Then, an excess resistance would arise from the difference between μ_{cp} and μ_{qp}

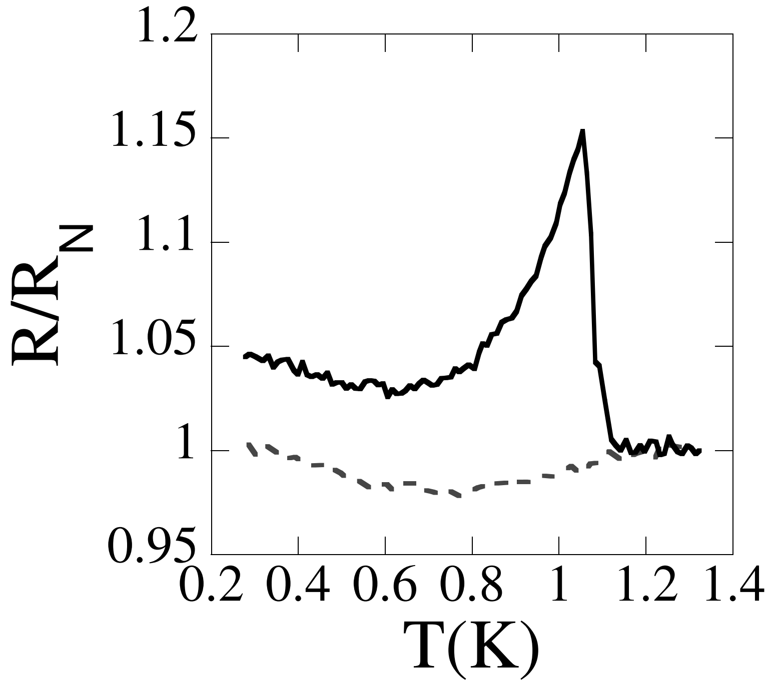

Figure 5.5. Normalized differential resistance of a Ni/Al interface as a function of temperature. The solid line is measured with probe configuration similar to shown in Fig. 5.1, *i.e.*, using an Al probe as V_-; the dashed line is measured using an Au probe close to interface as V_-.

near the interface. Specifically, if a superconducting probe is placed a distance x from the interface, the excess resistance ΔR will be measured as $\Delta R \approx (\lambda_{Q^*} - x)\rho_S$, where ρ_S is the resistance per unit length of the superconductor. λ_{Q^*} diverges when $\Delta \to 0$, and this divergence gives rise to the peak seen in the temperature dependent resistance measurements at a temperature just below T_c (shown in Fig. 5.4). The solid line in Fig. 5.5 illustrates the differential resistance of a Ni/Al interface as a function of temperature with probe configuration similar to shown in Fig. 5.1. An enhancement in resistance has been observed in this measurement at a temperature just below T_c as well. However, for this device, if we use a normal-metal (Au) probe close to the interface as the V_- probe in the four-terminal resistance measurement, we get a different temperature dependence, the dashed line in Fig. 5.5, where no excess resistance is measured. It is clear evidence that the peak features seen in the temperature dependence and the dV/dI *vs.* V measurements are associated with the charge imbalance effect. In addition, one may also notice that, at $T < 0.6$ K in Fig. 5.5, both the solid and the dashed lines show the same trend, which we believe is the intrinsic behavior of the interface, which does not depend on the measurement probes.

5.1.3. Spin-polarized Andreev reflection in FS device

As pointed out above, the probability of Andreev reflection depends on both P and Z, so that one cannot separate the their contributions only based on the measured zero bias resistance of FS junctions. In order to do so, a new device has been designed, where the polarization P of the "ferromagnet" can be varied. The schematic of this device is shown in Fig. 5.6, in which the "ferromagnet" is actually a normal metal (Cu) with a non-equilibrium magnetization injected from a real ferromagnet (Py). During the measurements, to create a non-zero spin polarization in Cu, we inject a spin-polarized current I_{sp} from a nearby Py into it. The magnitude of the non-equilibrium polarization in Cu depends on the magnitude of the injected current. However, this effect only exists over a certain length scale, the so-called spin-flip length λ_{sf}, which is ~ 1 μm in Cu[5] at a temperature of 4.2 K [**122**]. Beyond that, the electrons injected from Py would lose their spin memory, and the injected current would have equal number of spin-up and spin-down electrons. In practice, the distance between the Cu/Al interface and the Py/Cu interface is ~ 520 nm, hence the current injected from Py would still carry a finite spin polarization at the Cu/Al interface.

[5]Cu was chosen in our device because it has a long spin-flip length.

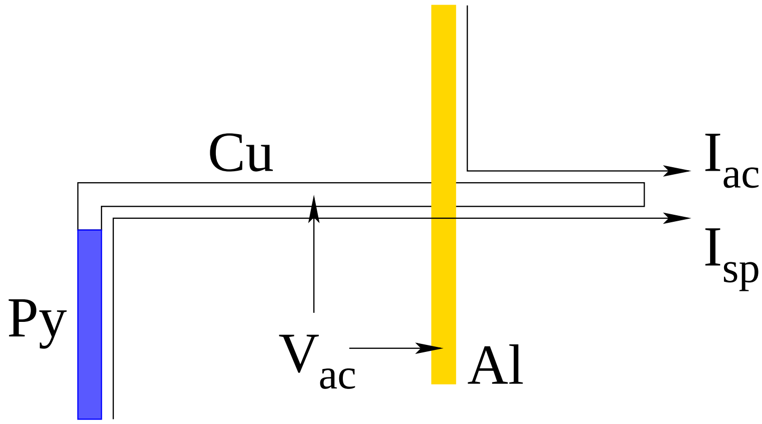

Figure 5.6. Schematic of the device for determining the dependence of the spin-polarized Andreev reflection on the polarization P of the "ferromagnet", as described in the text.

Figure 5.7 shows the central results of this experiment, in which we measured the differential resistance of the Cu/Al interface as a function of temperature with different dc currents injected from Py into Cu. The interface resistance was measured using conventional four-terminal technique with an excitation current $I_{ac} = 100$ nA. The dotted line in Fig. 5.7(a) plots the temperature dependence of the Cu/Al interface resistance at $I_{sp} = 0$, which is very similar to the results shown in Figs. 5.4 and 5.5. As the temperature drops below T_c, the interface resistance increases abruptly, showing a peak structure associated with the charge imbalance effect. When $I_{sp} \neq 0$, however, the overall shape of the R *vs.* T curve changes substantially as one increases $|I_{sp}|$ from 1 μA to 3 μA. One may notice that, as $|I_{sp}|$ increases, even the interface resistance at the lowest temperature increases significantly. It indicates that the applied dc current I_{sp} may cause some heating effect in our device, which raises the interface resistance and broadens the peak feature in the R *vs.* T curve. On the other hand, since the current path for $\pm I_{sp}$ is the same, effects due to Joule heating should also be the same, so that any differences between them will be due to the spin-polarized current.

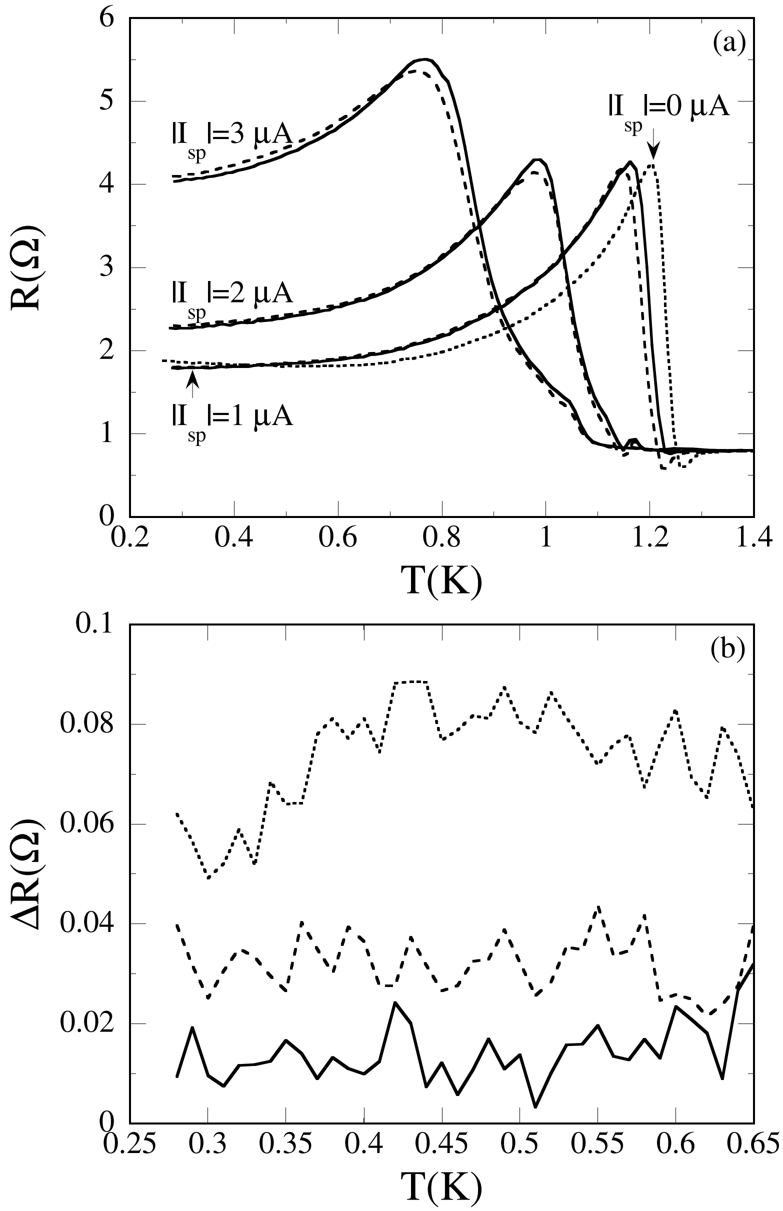

Figure 5.7. (a) Differential resistance of the Cu/Al interface as a function of temperature with different dc currents injected from Py into Cu. The dotted line shows the measurement at $I_{sp} = 0$. At $|I_{sp}| \neq 0$, for the same magnitude of $|I_{sp}|$, the solid lines illustrate the data of $I_{sp} > 0$, while the dashed lines represent the results with the injected currents in opposite directions. (b) Difference between the curves in (a) with the same magnitude of the injected currents but in opposite directions. The solid line is at $|I_{sp}| = 1$ μA, dashed line at $|I_{sp}| = 2$ μA, and dotted line at $|I_{sp}| = 3$ μA.

Note that a finite spin polarization only exists when $I_{sp} < 0$, *i.e.*, when an electron current is injected from the ferromagnet to the normal metal. When $I_{sp} > 0$, there would be no spin polarization induced in the normal metal. In 5.7(a), for the same magnitude of $|I_{sp}|$, the solid lines illustrate the data of $I_{sp} > 0$, while the dashed lines represent the results with injected currents in opposite directions, *i.e.*, $I_{sp} < 0$. At low temperatures, the dashed lines show larger resistance than the solid lines with the same $|I_{sp}|$ but in different directions. It is exactly what one expects, because when $I_{sp} < 0$, the induced spin polarization in Cu would reduce the probability of Andreev reflection, resulting in an increase in resistance. The difference between the spin-polarized and spin-unpolarized cases is indeed measurable, and can be seen clearly by taking the difference between the curves (solid and dashed lines in Fig. 5.7(a)) corresponding to the two current directions at each value of $|I_{sp}|$. These data are shown in Fig. 5.7(b), in which we only concentrate in the low temperature regime, from the base temperature of ^{3}He refrigerator to 650 mk, since the charge imbalance effect dominates higher temperatures. We believe, in such a low temperature regime, the differences shown in Fig. 5.7(b) are only related to the spin-polarized Andreev reflection effect, instead of a charge imbalance phenomena induced by using Al as the V_- probe in the four-terminal measurements. As shown in Fig. 5.7(b), the solid line plots the difference between the spin-polarized and spin-unpolarized cases at $|I_{sp}| = 1$, dashed line at $|I_{sp}| = 2$, and dotted line at $|I_{sp}| = 3$. Generally speaking, the differences increase as one increases the induced spin polarization in Cu by increasing $|I_{sp}|$.

We should point out that this experiment is only a preliminary investigation in topic of spin-polarized Andreev reflection. A measurable effect has been observed in the experiment, and it behaves in a way as we expected. In order to quantitatively study the dependence of the spin-polarized Andreev reflection on P, further experiments need to be done.

5.2. Superconducting proximity effect in a ferromagnetic metal

In diffusive proximity-coupled normal-metal systems, as discussed in previous chapters, the expected length scale of pair correlations induced by the superconductor is the superconducting coherence length in the normal metal $L_T = \sqrt{\hbar D/k_B T}$. For typical metallic films, L_T can be as long as 0.5 μm at $T = 1$ K. In a ferromagnet in contact with a superconductor, however, the above length scale is not valid any more, due to the presence of the strong exchange energy $E_{exc} \sim k_B T_{Curie}$, where T_{Curie} is the Curie temperature of the ferromagnet. Taking the common ferromagnetic material Ni as an example, the exchange energy is given by $E_{exc} \sim k_B(630\text{K})$, and the length over which superconducting correlations are conventionally expected is determined by the exchange length $L_{exc} = \sqrt{\hbar D/E_{exc}}$, which is estimated to be on the order of 2-20 nm [**123, 124**].

Recently, this statement is challenged in a number of publications, in which observations of a long-range superconducting proximity effect in a ferromagnet have been reported [**35, 36, 37, 38, 39, 40**]. In Ref. [**37**], Lawrence and Giordano measured the resistance of narrow Ni wires with superconducting Sn contacts as a function of temperature, and observed a significant resistance change at $T < T_c$. Based on the amplitude of the resistance change, they estimated the distance of the superconducting correlations in the ferromagnet as 46 nm. Giroud *et al.* [**38**] studied the temperature dependence of a Co ring in proximity to a superconducting Al pad. A non-monotonic behavior has been observed, which is similar to the reentrance behavior seen in a NS system. The amplitude of the resistance change below T_c is $< 1\%$ of the normal state resistance, comparing with $12-15\%$ for an ideal NS system. Again, from the size of this change, they estimated that the superconducting correlations extended in a ferromagnet up to a distance of approximately 180 nm. More recently, this problem has been reexamined by the same group, by measuring the temperature dependence of a short Co wire in contact with a superconductor Al pad with highly transparent interface [**40**]. A much larger proximity effect has been seen in these devices with almost 12% decrease in resistance at low temperatures, but no evidence of reentrant behavior. Petrashov *et al.* [**39**] also observed a *giant* proximity effect in Ni wires connected with a superconducting Al reservoir. These samples showed a decrease in resistance below the superconducting transition amounting to approximately $10-12\%$. They attributed this behavior to a proximity effect which extended into the ferromagnet to a distance of 600 nm. In short, in the above experiments, the measured extent of the superconducting correlations in a ferromagmet is much larger than the exchange length L_{exc}.

In addition, the long-range superconducting proximity effect is also supported by recent theoretical studies, where they show that the proximity effect may be still appreciable in a ferromagnet within a length scale comparable to the superconducting coherence length L_T, if the magnetization in the ferromagnet is spatially inhomogeneous [**41, 42**]. This long-range effect arises from the triplet component of the superconducting correlations in the ferromagnet, rather than the singlet component responsible for the conventional proximity effect in a normal metal. Although there is no experimental evidence to date to prove the existence of such a triplet proximity effect, the experiments discussed above indeed point to this mechanism as an possibility.

This problem has also attracted our interest and been explored experimentally in our group. Aumentado *et al.* [**125**] measured the resistance of a Ni ellipse in proximity to a superconductor (Al) pad as a function of temperature. The measurement shows no evidence of a proximity effect in the ferromagnet, although the Ni/Al interface resistance indeed shows a strong temperature dependence (Figs. 5.4 and 5.5). However, one criticism of this work was that the FS interface resistance in our device was too high (the specific resistance of the Ni/Al interface was ~ 370 mΩ μm^2), so that the proximity effect induced in the ferromagnet may be suppressed. In Ref. [**40**], Giroud *et al.* pointed out that the proximity effect is large only when the FS interface is highly transparent. They observed a $\sim 12\%$ resistance change in a device with specific interface resistance estimated to be less than 6 mΩ μm^2; while no appreciable change in resistance was measured for a device with specific interface resistance of ~ 600 mΩ μm^2.

Recently, *in situ* Ar^+ plasma etching was applied in our fabrication process to clean the ferromagnetic structures prior to depositing the Al film on top of them. This method improves the FS interface transparency significantly, and enables us to reduce the specific resistance to 20-40 mΩ μm^2. Figure 5.8 shows a SEM image of a Ni/Al interface device with specific interface resistance of 23 mΩ μm^2. This device has a relatively complicated configuration for other research purposes; here, we are going to only concentrate on the proximity effect induced in the left Ni ellipse. Figure 5.9 shows the resistance of the left Ni ellipse as a function of temperature, measured

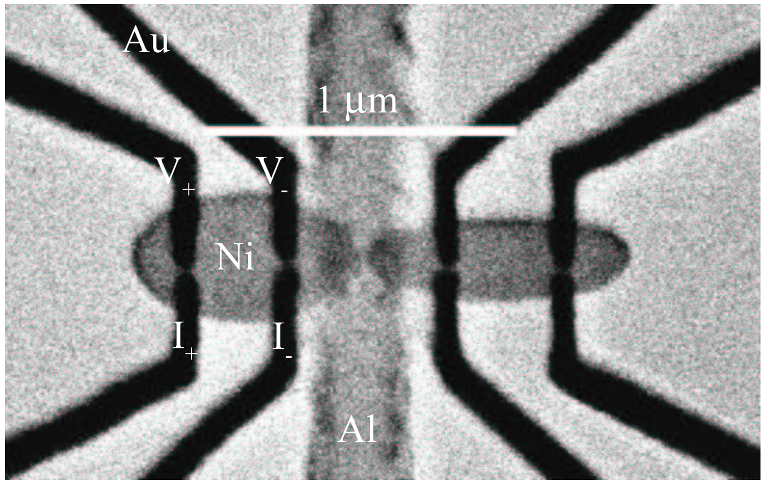

Figure 5.8. SEM image of a Ni/Al interface device with specific interface resistance of 23 mΩ μm^2. We will only concentrate on the proximity effect induced in the left Ni ellipse.

by the four normal-metal (Au) probes patterned on top of the Ni element. A clear decrease in resistance has been observed at $T < T_c$, which is $\sim$ 1.2 K for Al. Note that the total resistance change is about 0.07 % of the normal state resistance, and the distance from the I_- and V_- probes to the Ni/Al interface is $\sim$ 36 nm. Thus, our resistance change is much less than the measured resistance decrease by other groups [**39, 40**].

However, before we conclude the resistance drop in Fig. 5.9 is indeed associated with the proximity effect in the Ni element, we should rule out other possibilities which may also have contributions to the temperature dependent resistance change. First of all, it has been proposed that current redistribution causes the same effect. When we cool down the device through the transition temperature of the superconductor, the distribution of the measurement current in the Ni element may be modified due to the transition. Therefore, it may change the measured resistance of Ni. Notice that this effect would only appear at $T \sim T_c$. In Fig. 5.9, however, the

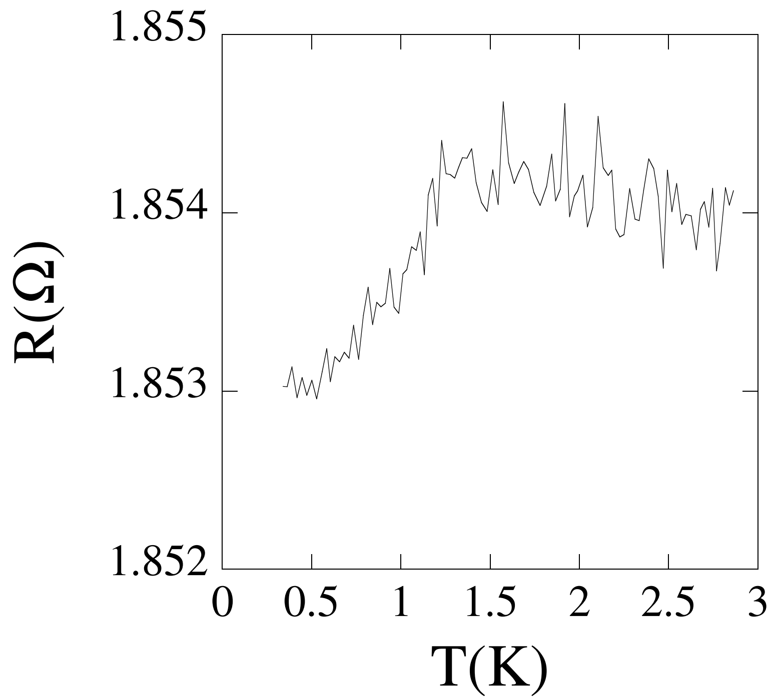

Figure 5.9. The temperature dependence of the left Ni ellipse shown in Fig. 5.8, measured by the four normal-metal (Au) probes patterned on top of the Ni element.

resistance of Ni ellipse gradually decreases as the temperature is decreased below T_c. Therefore, the resistance drop, particularly the drop at low temperatures, would not be a consequence of current redistribution. A second reason is the anisotropic magnetoresistance (AMR) of Ni. For a typical ferromagnetic metal, its AMR increases as one decreases the temperature [**40**]. The overall resistance change is 0.1% in a temperature range of 0.1-1.5 K. In fact, at a temperature above T_c in Fig. 5.9, we do observe a slight increase in resistance as the temperature drops. Since the AMR shows opposite temperature dependence compared with the proximity effect, it would not contribute to the resistance drop below T_c.

Hence, we now can conclude that we have observed a weak proximity effect in a ferromagnet (Ni) in contact with a superconductor (Al) with a specific interface resistance of 23 mΩ μm^2. The total resistance drop below T_c in our measurements is much less than that of the previous work [**39, 40**]. Additionally, it is important to note that a major difference between our samples and the samples measured by other groups is that the ferromagnetic elements in our case are elliptical in shape, which presumably have a relatively homogeneous magnetization, and reduce the possibility of the appearance of the triplet proximity effect. This may account for the smaller amplitude of the effect we observe.

CHAPTER 6

Conclusions and future work

6.1. Thermal transport properties of mesoscopic devices

In Chapter 2 and 4, we have studied the thermal transport properties, *i.e.*, thermal conductance and thermopower, of Andreev interferometers both experimentally and theoretically. In particular, we have examined the Wiedemann-Franz law in the proximity regime and measured phase coherent thermal conductance oscillations as a function of the applied magnetic field. We find that our experimental results are qualitatively consistent with our numerical simulations. In the study of the thermopower of Andreev interferometers, we focused on the symmetry of the thermopower oscillations with respect to the applied magnetic flux through the interferometer loop. Our results show that the symmetry is essentially associated with the distribution of the supercurrent in the device, which indicates that the origin of the thermopower oscillations may arise from the conversion of the supercurrent to the quasiparticle current.

The conclusions and future developments of our work are summarized in the following.

6.1.1. Thermal conductance of Andreev interferometers

In the experimental investigations of this topic, we have measured the thermal conductance of Andreev interferometers in two different geometries, namely the "house" and "parallelogram" interferometers. In both cases, we observe strong suppressions in thermal conductance and deviation of the Wiedemann-Franz law at low temperatures. In addition, we find the thermal conductance behaves non-linearly as a function of the thermal current I^T through the sample, showing a remarkable $\sqrt{I^T}$ dependence at low thermal currents. As a magnetic field is applied, the measured thermal conductance oscillates periodically with a fundamental period corresponding to one flux quantum $\Phi_0 = h/2e$, demonstrating the phase coherent nature of the thermal transport in these devices. As with the electric conductance, the thermal conductance oscillations are symmetric with respect to the magnetic flux.

In the theoretical study of this topic, we extend the quasiclassical theory of the superconductivity and calculate the thermal conductance of the "house" and "parallelogram" Andreev interferometers. Our simulation results are qualitatively in agreement with the experimental results.

As we pointed out in Chapter 4, the deviation of the measured thermal conductance to the theoretical predictions may be associated with the long length scales required to equilibrate the energy of the quasiparticles in mesoscopic systems. Hence, it would be very instructive if we can measure the thermal conductance of a single normal-metal wire. However, in our devices, the design of the thermometers requires superconducting leads, which always introduce superconducting correlations in our measurements. In order to avoid this problem and measure the thermal conductance of a pure normal-metal system, a superconductor/insulator/normal-metal (SIN) tunnel junction probably is the best choice of the thermometry.

6.1.2. Thermopower of Andreev interferometers

In order to study the relation between the symmetry of the phase-dependent thermopower oscillations and the supercurrent distribution in the device, we have designed a double-loop interferometer, in which we can change the supercurrent distribution. Our measurements show that the symmetry of the thermopower oscillations can be either symmetric or antisymmetric in the same device depending on the distribution of the supercurrent. Unfortunately, the detailed mechanism of the coupling of the thermopower to the supercurrent is still unknown at the moment, which needs to be further investigated both experimentally and theoretically. Additionally, as was found before, the amplitude of the thermopower oscillations shows a non-monotonic dependence on the temperature, showing a maximum at some intermediate temperature T_m. In our measurements, we find that this intermediate temperature is related to the correlation energy E_c of the system, $T_m \sim E_c/k_B$.

In addition to continuing the investigation of the dependence of the thermopower on the supercurrent in Andreev interferometers, we are also in the process of exploring their use in potential devices, in which we can tune the thermopower of Andreev interferometers by changing the supercurrent. It has been shown that in such devices, depending on the applied magnetic flux, the thermopower of the Andreev interferometer can be either positive (n-type) or negative (p-type). The magnitude of the thermopower is tunable as well, up to the order of a few μV/K. This kind of device, if successful, will be an exciting practical application of the thermoelectric effects in NS heterostructures. It may provide a new mechanism for designing on-chip cooler for future highly packed electronics.

6.1.3. Thermal transport properties of other mesoscopic samples

It has been continuously a popular topic to study the thermal transport properties of mesoscopic devices in recent years. A typical example is the investigations of the thermal and thermoelectric properties of carbon nanotubes, which has attracted much interest recently [**83, 126, 127**]. Based on our knowledge and the techniques developed during the study of the thermal conductance and thermopower of Andreev interferometers, it should not be difficult for us to measure the thermal properties of other mesoscopic samples. Actually, the measurements of the thermopower of individual multiwall carbon nanotudes are already in process.

6.2. Spin transport in ferromagnet/superconductor devices

In Chapter 5, we have studied the differential resistance of mesoscopic FS junctions as a function of the voltage bias. We observe a number of interesting features in the dV/dI *vs.* V curve, which are associated with charge imbalance and the injection of spin polarized current into the superconductor. In particular, we have observed the splitting of the dips in dV/dI as a function of the applied magnetic field, due to the Zeeman splitting of the quasiparticle density of states. We have also observed peak structures in dV/dI at voltage biases corresponding to the superconducting gap, which are related to the charge imbalance effect in the superconductor near the FS interface. Finally, we have studied the superconducting proximity effect in a ferromagnet in proximity to a superconductor with a highly transparent FS interface. In our experiments, we find a long range proximity effect in the ferromagnet at a distance of ~ 36 nm from the FS interface. This measured effect is much less than that of other groups.

The FS heterostructure device is a gold mine, which involves tremendously interesting physics. The work described in this thesis is only a scratch on its surface. To date, although a number of beautiful experiments have been done in this field, many topics are still not matured and need to be further investigated. Our ability of making highly transparent FS interfaces and precisely aligned multilayer e-beam lithographic devices opens the possibility for us to study the challenging but inviting physics in this field.

References

[1] *Mesoscopic Superconductivity*, edited by F. Hekking, G. Schön, and D. Averin [Physica (Amsterdam) **203B** (1994)].

[2] C.J. Lambert and R. Raimondi, J. Phys. Condensed Matter **10**, 901 (1998).

[3] P.G.N. de Vegvar, T.A. Fulton, W.H. Mallison, and R.E. Miller, Phys. Rev. Lett. **73**, 1416 (1994).

[4] H. Pothier, S. Guéron, D. Esteve, and M. H. Devoret, Phys. Rev. Lett. **73**, 2488 (1994).

[5] V.T. Petrashov, V.N. Antonov, P. Delsing, and T. Claeson, Phys. Rev. Lett. **74**, 5268 (1995).

[6] H. Courtois, Ph. Gandit, D. Mailly, and B. Pannetier, Phys. Rev. Lett. **76**, 130 (1996).

[7] S.G. den Hartog, C.M. A. Kapteyn, B.J. van Wees, and T.M. Klapwijk , Phys. Rev. Lett. **76**, 4592 (1996).

[8] P.G. de Gennes, *Superconductivity of Metals and Alloys*, (Benjamin, New York, 1964).

[9] M. Tinkham, *Introduction to Superconductivity*, (McGraw-Hill, New York, 1996).

[10] A.F. Andreev, Sov. Phys. JETP, **19**, 1228 (1964).

[11] G. Wiedemann and R. Franz, Ann. Phys., Lpz., (2), **89**, 497 (1853).

[12] N.W. Ashcroft and N.D. Mermin, *Solid State Physics* (New York, Holt, Rinehart and Winston, 1976).

[13] D.A. Dikin, S. Jung, and V. Chandrasekhar, Phys. Rev. B **65**, 12511 (2001).

[14] E.V. Bezuglyi and V. Vinokur, Phys. Rev. Lett. **91**, 137002 (2003).

[15] Z. Jiang and V. Chandrasekhar, cond-mat/0501478.

[16] Z. Jiang and V. Chandrasekhar, Phys. Rev. Lett. **94**, 147002 (2005).

[17] J. Eom, C.-J. Chien, and V. Chandrasekhar, Phys. Rev. Lett. **81**, 437 (1998); Superlattices and Microstructures **25**, 733 (1999); Journal of Low Temperature Physics **118**, 617 (2000).

[18] D.A. Dikin, S. Jung, and V. Chandrasekhar, Europhys. Lett. **57** 564 (2002).

[19] A. Parsons, I.A. Sosnin, and V.T. Petrashov, Phys. Rev. B **67**, 140502(R) (2003).

[20] R. Seviour and A.F. Volkov, Phys. Rev. B **62**, 6116 (2000).

[21] V.R. Kogan, V.V. Pavlovskii, and A.F. Volkov, Europhys. Lett. **59** 875 (2002).

[22] P. Virtanen and T.T. Heikkilä, Phys. Rev. Lett. **92**, 177004 (2004); cond-mat/0405285.

[23] Z. Jiang and V. Chandrasekhar, to appear in Chinese J. Phys..

[24] P.M. Tedrow and R. Meservey, Phys. Rev. Lett. **26**, 192 (1971); Phys. Rev. B **7**, 318 (1973).

[25] R.J. Soulen, Jr., J.M. Byers, M.S. Osofsky, B. Nadgorny, T. Ambrose, S.F. Cheng, P.R. Broussard, C.T. Tanaka, J. Nowak, J.S. Moodera, A. Barry, and J.M.D. Coey, Science, **282**, 85 (1998).

[26] S.K. Upadhyay, A. Palanisami, R.N. Louie, and R.A. Buhrman, Phys. Rev. Lett. **81**, 3247 (1998).

[27] G.J. Strijkers, Y. Ji, F.Y. Yang, C.L. Chien, and J.M. Byers, Phys. Rev. B **63**, 104510 (2001).

[28] B. Nadgorny, I.I. Mazin, M. Osofsky, R.J. Soulen, Jr., P. Broussard, R.M. Stroud, D.J. Singh, V.G. Harris, A. Arsenov, and Ya. Mukovskii, Phys. Rev. B **63**, 184433 (2001).

[29] I.I. Mazin, A.A. Golubov, and B. Nadgorny, J. Appl. Phys. **89**, 7576 (2001).

[30] Y. Ji, G.J. Strijkers, F.Y. Yang, C.L. Chien, J.M. Byers, A. Anguelouch, Gang Xiao, and A. Gupta, Phys. Rev. Lett. **86**, 5585 (2001).

[31] C.H. Kant, O. Kurnosikov, A.T. Filip, P. LeClair, H.J.M. Swagten, and W.J.M. de Jonge, Phys. Rev. B **66**, 212403 (2002).

[32] G.E. Blonder, M. Tinkham, and T.M. Klapwijk, Phys. Rev. B **25**, 4515 (1982).

[33] Z. Jiang, J. Aumentado, W. Belzig and V. Chandrasekhar, to appear in the proceedings of the St. Petersburg NATO Conference on Quantum transport, St. Petersburg, August, 2003 (cond-mat/0311334).

[34] W. Belzig, A. Brataas, Yu.V. Nazarov, and G.E.W. Bauer, Phys. Rev. B **62**, 9726 (2000).

[35] V.T. Petrashov, V.N. Antonov, S.V. Maksimov, and R.S. Shaikhaidarov, JEPT Lett. **59**, 523 (1994).

[36] V.T. Petrashov, Czech. J. Phys. **46**, 3303 (1996).

[37] M.D. Lawrence and N. Giordano, J. Phys.: Condens. Matt. **8**, L563 (1996); **11**, 1089 (1999).

[38] M. Giroud, H. Courtois, K. Hasselbach, D. Mailly, and B. Pannetier, Phys. Rev. B **58**, 11872 (1998).

[39] V.T. Petrashov, I.A. Sosnin, I. Cox, A. Parsons, and C. Troadec, Phys. Rev. Lett. **83**, 3281 (1999).

[40] M. Giroud, K. Hasselbach, H. Courtois, D. Mailly, and B. Pannetier, Eur. Phys. J. B **31**, 103 (2003).

[41] F.S. Bergeret, A.F. Volkov and K.B. Efetov, Phys. Rev. Lett. **86**, 4096 (2001).

[42] A. Kadigrobov, R.I. Shekhter and M. Jonson, Europhys. Lett. **54**, 394 (2001).

[43] E. Zhao, T. Löfwander, and J.A. Sauls, Phys. Rev. Lett. **91**, 077003 (2003).

[44] A. Schmid, *Nonequilibrium Superconductivity*, edited by K.E. Gray (Plenum, N.Y., 1981).

[45] J. Rammer, and H. Smith, Rev. Mod. Phys. **58**, 323 (1986).

[46] W. Belzig, F.K. Wilhelm, C. Bruder, G. Schön, and D. Zaikin, Superlattices and Microstructures **25**(5-6), 1251 (1999).

[47] F.K. Wilhelm, Ph.D. Thesis, Universität Karlsruhe (1999).

[48] V. Chandrasekhar, chapter in *The Physics of Superconductors: Vol. II*, Ed. K. H. Bennemann and J. B. Ketterson (Springer, Berlin, 2004).

[49] L.P. Kadanoff and G. Baym, *Quantum Statistical Mechanics*, (Benjamin, N.Y., 1962).

[50] A. Schmid and G. Schön, J. Low. Temp. Phys. **20**, 207 (1972).

[51] A.I. Larkin and Yu. N. Ovchinnikov, Zh. Eksp. Teor. Fiz. **73**, 299 (1977) [Sov. Phys. JETP **46**, 155 (1978)].

[52] A.V. Zaitsev, Zh. Eksp. Teor. Fiz. **86**, 1742 (1984) [Sov. Phys. JETP **59**, 1015 (1985)].

[53] M.Yu. Kuprianov and V.F. Lukichev, Zh. Eksp. Teor. Fiz. **94**, 139 (1988) [Sov. Phys. JETP **67**, 1163 (1988)].

[54] A.I. Larkin, and Yu.V. Ovchinnikov, Sov. Phys. JETP **46**, 155 (1977).

[55] A.F. Volkov, Physica B **203**, 267 (1994).

[56] Yu.V. Nazarov and T.H. Stoof, Phys. Rev. Lett. **76**, 823 (1996).

[57] T.H. Stoof, and Yu.V. Nazarov, Phys. Rev. B **53**, 14496 (1996).

[58] A.A. Golubov, F.K. Wilhelm, and A.D. Zaikin, Phys. Rev. B **55**, 1123 (1997).

[59] S. Yip, Phys. Rev. B **58**, 5803 (1998).

[60] S. Guéron, H. Pothier, N.O. Birge, D. Esteve, and M.H. Devoret, Phys. Rev. Lett. **77**, 3025 (1996).

[61] P. Charlat, H. Courtois, Ph. Gandit, D. Mailly, A.F. Volkov, and B. Pannetier, Phys. Rev. Lett. **77**, 4950 (1996).

[62] C.-J. Chien and V. Chandrasekhar, Phys. Rev. B **60**, 15356 (1999).

[63] M.J. Black and V. Chandrasekhar, Europhys. Lett. **50**, 257 (2000).

[64] A.F. Volkov, A.V. Zaitsev, and T.M. Klapwijk, Physica (Amsterdam) **210C**, 21 (1993).

[65] A.F. Volkov and A.V. Zaitsev, Phys. Rev. B **53**, 9267 (1996).

[66] A.A. Abrikosov, *Fundamentals of the Theory of Metals* (Elsevier Science, Amsterdam, (1988).

[67] J. Clarke and S.M. Freake, Phys. Rev. Lett. **29**, 588 (1972).

[68] A.G. Aronov and Yu.M. Gal'perin, Zh. ETF Pis. Red **19**, 281 (1974) [JETP Lett. **19**, 165 (1974)].

[69] Yu.M. Gal'perin, V.L. Gurevich, and V.I. Kozub, Zh. Eksp. Teor. Fiz. **66**, 1387 (1974) [Sov. Phys. JETP **39**, 680 (1974)].

[70] S.N. Artemenko and A.F. Volkov, Zh. Eksp. Teor. Fiz. **70**, 1051 (1976) [Sov. Phys. JETP **43**, 548 (1976)].

[71] M.V. Kartsovnik, V.V. Ryazanov, and V.V. Shmidt, Pis'ma Zh. Eksp. Teor. Fiz **33**, 373 (1981) [JETP Lett. **33**, 356 (1981)].

[72] V.V. Ryazanov and V.V. Schmidt, Solid State Commun. **42**, 733 (1982).

[73] N.R. Claughton and C.J. Lambert, Phys. Rev. B **53**, 6605 (1996).

[74] Tero T. Heikkilä, Markku P. Stenberg, Martti M. Salomaa and Colin J. Lambert, Physica B, **284-288**, 1862 (2000).

[75] D.J. Van Harlingen, J. Low Temp. Phys. **44**, 163 (1981).

[76] D.J. Van Harlingen, Physica 109 and 110B, 1710 (1982).

[77] H.J. Mamin, J. Clarke and D.J. Van Harlingen, Phys. Rev. B **29**, 3881 (1984).

[78] J. Eom, Ph.D. thesis, Northwestern University (1998).

[79] C.-J. Chien, Ph.D. thesis, Northwestern University (1998).

[80] J. Aumentado, Ph.D. thesis, Northwestern University (2000).

[81] Z. Zhang, Ph.D. thesis, Northwestern University, in preparation.

[82] K. Schwab, E.A. Henriksen, J.M. Worlock, M.L. Roukes, Nature **404**, 974 (2000).

[83] P. Kim, L. Shi, A. Majumdar, and P.L. McEuen, Phys. Rev. Lett. **87**, 215502 (2001).

[84] W.M. Moreau, *Semiconductor Lithography: Principles, Practices, and Materials (Microdevices : Physics and Fabrication Technologies)*, (Plenum Press, New York, 1988).

[85] *Handbook of microlithography, micromaching and microfabrication*, edited by P. Rai-Choudhury, (SPIE Optical Engineering Press, Bellingham, Wa., 1997).

[86] J. Eom, Y.S. Shin, and H.J. Lee, Phys. Stat. Sol. (b), **241**, 1494 (2004).

[87] J.G. Adler and J.E. Jackson, Rev. Sci. Instrum. **37**, 1049 (1966).

[88] K.E. Nagaev, Phys. Rev. B **52**, 4740 (1995).

[89] M. Henny, S. Oberholzer, C. Strunk, and C. Schönenberger, Phys. Rev. B **59**, 2871 (1999).

[90] J.P. Pekola, Journal of Low Temperature Physics **135**, 723 (2004).

[91] J.P. Pekola, K.P. Hirvi, J.P. Kauppinen, and M.A. Paalanen, Phys. Rev. Lett. **73**, 2903 (1994).

[92] P. Delsing, C.D. Chen, T. Claeson, P. Davidsson, B. Jonson, M. Lindroos, S. Norrman, G. Nyman, and S. Qutaishat, Physica B, **194**, 27 (1994).

[93] J.P. Kauppinen, K.T. Loberg, A.J. Manninen, J.P. Pekola, Rev. Sci. Instr. **69**, 4166 (1998).

[94] A.J. Manninen, J.P. Kauppinen, S. Farhangfar, L.J.T. Taskinen, and J.P. Pekola, Physica B, **284**, 2010 (2000).

[95] J.P. Pekola, J.K. Suoknuuti, M. Weiss, P. van der Linden, and A.G.M. Jansen, Journal of Low Temperature Physics **128**, 263 (2002).

[96] Y.M. Blanter and M. Büttiker, Phys. Rep. **336**, 1 (2000).

[97] L. Spietz, K.W. Lehnert, I. Siddiqi, and R.J. Schoelkopf, Science **300**, 1929 (2003).

[98] M. Henny, H. Birk, R. Huber, C. Strunk, A. Bachtold, M. Krüger, and C. Schönenberger, Appl. Phys. Lett. **71**, 773 (1997).

[99] A.H. Steinbach, J.M. Martinis, and M.H. Devoret, Phys. Rev. Lett. **76**, 3806 (1996).

[100] X. Jehl, P. Payet-Burin, C. Baraduc, R. Calemczuk, and M. Sanquer, Phys. Rev. Lett. **83**, 1660 (1999).

[101] J. Aumentado, V. Chandrasekhar, J. Eom, P.M. Baldo, and L.E. Rehn, Appl. Phys. Lett. **75**, 3554 (1999).

[102] Z. Jiang, H. Lim, J. Eom, and V. Chandrasekhar, Appl. Phys. Lett. **83**, 2190 (2003).

[103] M. Nahum, T.M. Eiles, and J.M. Martinis, Appl. Phys. Lett. **65**, 3123 (1994).

[104] M.M. Leivo, J.P. Pekola, and D.V. Averin, Appl. Phys. Lett. **68**, 2190 (1996).

[105] H. Pothier, S. Guéron, N.O. Birge, D. Esteve, and M.H. Devoret, Z. Phys. B **104**, 178 (1997).

[106] A.I. Zaitsev, JETP Lett. **61**, 771 (1995).

[107] M. Grove, R. Dittmann, M. Bode, M. Siegel, and A.I. Braginski, Appl. Phys. Lett. **69**, 696 (1996).

[108] V.T. Petrashov, V.N. Antonov, S.V. Maksimov, and R.S. Shaikhaidarov, Pis'ma Zh. Eksp. Teor. Fiz. **58**, 48 (1993) [JEPT Lett. **58**, 49 (1993)].

[109] V.N. Antonov, A.F. Volkov, and H. Takayanagi, Phys. Rev. B **55**, 3836 (1997).

[110] F.K. Wilhelm, A.D. Zaikin, and H. Courtois, Phys. Rev. Lett. **80**, 4289 (1998).

[111] V.T. Petrashov, R.Sh. Shaikhaidarov, and I.A. Sosnin, Pis'ma Zh. Eksp. Teor. Fiz. **64**, 789 (1996) [JETP Lett. **64**, 839 (1996)].

[112] W. Belzig, R. Shaikhaidarov, V.V. Petrashov, and Yu.V. Nazarov, Phys. Rev. B **66**, 220505 (2002).

[113] C.C. Chi and J. Clarke, Phys. Rev. B **19**, 4495 (1979).

[114] M. Stuivinga, J.E. Mooij, and T.M. Klapwijk, Physica B and C **108B**, 1023 (1981).

[115] D.A. Dikin, M.J. Black, and V. Chandrasekhar, Phys. Rev. Lett. **87**, 187003 (2001).

[116] J. Clarke, Phys. Rev. Lett. **28**, 1363 (1972).

[117] M. Tinkham and J. Clarke, Phys. Rev. Lett. **28**, 1366 (1972).

[118] M.L. Yu and J.E. Mercereau, Phys. Rev. Lett. **28**, 1117 (1972); Phys. Rev. B **12**, 4909 (1975).

[119] T.Y. Hsiang and J. Clarke, Phys. Rev. B **21**, 945 (1980).

[120] T.Y. Hsiang, Phys. Rev. B **21**, 956 (1980).

[121] C.-J. Chien and V. Chandrasekhar, Phys. Rev. B **60**, 3655 (1999).

[122] F.J. Jedema, A.T. Filip, and B.J. van Wees, Nature **410**, 345 (2001).

[123] K. Kawaguchi and M. Sohma, Phys. Rev. B **46**, 14722 (1992).

[124] J.S. Jiang, D. Davidović, D.H. Reich, and C.L. Chien, Phys. Rev. Lett. **74**, 314 (1995).

[125] J. Aumentado and V. Chandrasekhar, Phys. Rev. B **64**, 54505 (2001).

[126] J.P. Small, K.M. Perez, and P. Kim, Phys. Rev. Lett. **91**, 256801 (2003).

[127] M.C. Llaguno, J.E. Fischer, J. Hone, and A.T. Johnson, Nano Letters **4**, 45 (2004).